

Joint Institute for VLBI in Europe

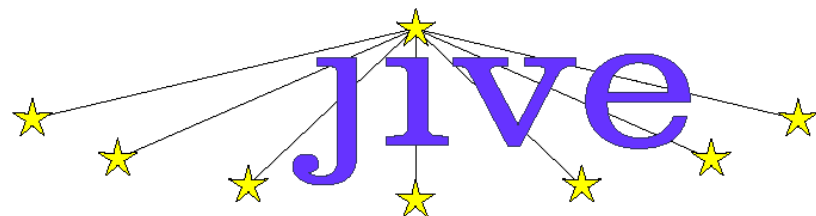
VLBI Observations of the Huygens Probe

ESA-ESTEC Contract No. 18386/NL/NR
Final Report

JIVE Research Note #0011

15 October 2008

Dwingeloo



JOINT INSTITUTE FOR VLBI IN EUROPE

This study is conducted at the Joint Institute for VLBI in Europe under Contract between ESA and JIVE No. 18386/NL/NR.

Project manager
Project scientist

L.I. Gurvits
S.V. Pogrebenko

Huygens VLBI Group at JIVE

I.M. Avruch, H.E. Bignall, A. Brunthaler,
R.M.Campbell, S.M. Parsley, R. Oerlemans

ESA Technical Managers

J.-P. Lebreton, C.G.M.. van't Klooster

Joint Institute for VLBI in Europe

P.O. Box 2
7990 AA Dwingeloo
The Netherlands

Tel: +31-521-596500
Fax: +31-531-596539
e-mail: secretary@jive.nl
www.jive.nl

Huygens VLBI Tracking Team

T. An¹, S.W. Asmar², M.K. Bird³, W.Brisken⁴,
G.Cimo^{5,6}, J.M. Dickey⁵, R.D.Dodson^{7,8},
S.Elingsen⁵, A.R. Foley⁹, W.M.Folkner²,
F.Ghigo⁴, X.-Y. Hong¹, S. Huang¹, T. Kondo¹⁰,
Y.Koyama¹⁰, D.-R. Jiang¹, G. Langston⁴, X.Liu¹¹,
J.E.J. Lovell^{6,12}, A. Mujunen¹³, L.Petrov¹⁴,
C.J.Phillips¹², R.A. Preston², B. Reid⁵,
C.Reynolds^{6,8}, J.E. Reynolds¹², J. Ritakari¹³,
J.D.Romney⁴, R.J. Sault¹², H. Takeuchi^{10,15},
S.J.Tingay^{8,16}, A.K.Tzioumis¹²

Smart-1 Tracking Team (Section 13.1)

E. Baynes⁵, O. Camino¹⁷, P.G. Edwards¹²,
P.Ehrenfreund¹⁸, B. Foing¹⁷, H. Hase¹⁹,
M.Kettenis⁶, G. Maccaferri²⁰, M. Martinez
Fernandez¹⁷, P. McManamon¹⁷, G. Molera¹³,
S.Montebugnoli²⁰, T.Morley¹⁷, A. Orlati²⁰,
M.Pereira de Lucena²¹, S. Sobarzo¹⁹, A.Sombra
da Silva²¹, J. Stevens⁵, H.J. Stiepel⁹,
K.Stuurwold⁹, A.Szomoru⁶, J. Wagner¹³

¹ Shanghai Astronomical Observatory, Shanghai, China

² NASA Jet Propulsion Laboratory, Pasadena, CA, USA

³ Radioastronomisches Institut Universität Bonn, Germany

⁴ National Astronomical Observatory, USA

⁵ University of Tasmania, Hobart, Australia

⁶ Joint Institute for VLBI in Europe, Dwingeloo, The Netherlands

⁷ Observatorio Astronómico Nacional, Yebes, Spain

⁸ Curtin University, Perth, Australia

⁹ ASTRON, Dwingeloo, The Netherlands

¹⁰ National Institute of Information and Communication Technologies, Japan

¹¹ Urumqi Astronomical Observatory, Urumqi, China

¹² Australia Telescope National Facility, Australia

¹³ Helsinki University of Technology TKK, Kymälä, Finland

¹⁴ NASA Goddard Space Flight Center, Greenbelt, MD, USA

¹⁵ JAXA Institute of Space and Astronautical Sciences, Japan

¹⁶ Swinburne University, Melbourne, Australia

¹⁷ European Space Agency

¹⁸ Radboud University Nijmegen, The Netherlands

¹⁹ TIGO, Universidad de Concepción, Chile

²⁰ Istituto di Radioastronomia, Bologna, Italy

²¹ Northeastern Space Radio Observatory, Fortaleza, CE, Brazil

Table of contents

1. Introduction	6
2. WP 1000: management.....	7
2.1. Identification of radio telescopes – potential participants of Huygens VLBI tracking.....	7
2.2. Technical aspects of readiness for Huygens VLBI tracking	8
3. WP 2000: Description and preparation of the test observation instrumentation and logistics	10
3.1. Front-end radio telescope instrumentation.....	10
3.2. Digital back-end radio telescope instrumentation and related software ..	10
3.3. Data recording and processing instrumentation.....	10
4. WP 3000: Huygens VLBI Tracking test observation #1 of 27 August 2004	12
4.1. Observing strategy	12
4.2. Radio telescope array	13
4.3. Scheduling issues, logistics and operational feedback	13
4.4. Data processing	13
5. Huygens VLBI project data processing setup at JIVE.....	15
5.1. Narrow band signal extraction and analysis.....	16
5.2. PCEVN/MRO-to-Mark5 data conversion.....	18
6. WP 5000: Huygens VLBI Tracking observation 14 January 2005 (GG057C) ..22	22
6.1. Observing strategy, preparatory status, personnel functions	22
6.2. Express “next morning” results and evaluation	25
7. Software for fast processing of pre-filtered Huygens data.....	27
7.1. Introduction.....	27
7.2. The software application design.....	28
7.3. Some software and hardware characteristics	39
8. Huygens VLBI data processing and preliminary results.....	40
8.1. Broad-band processing of the calibrator signal.....	40
8.2. Calibrator data analysis.....	42
8.3. Narrow band processing of the Huygens Probe signal	46
8.4. Single dish detection of the probe’s signal.....	46
8.5. Single dish detections	50
8.6. Closer look into the single dish detections data	53
8.7. Cross-correlation, phase referencing and phase/delay detection	56
8.8. Probe’s trajectory reconstruction algorithm.....	60
8.9. Resulting trajectory and meridional wind.....	66
9. VLBI Delay Computation	68
9.1. VLBI Time Delay	68
9.2 Huygens VLBI Time Delay Calculation	68
9.3 VLBI Time Delay Partial Derivatives	69
10. WPCCN-2000, 3000 and 4000: High resolution (time/frequency) Doppler data extraction and post-landing analysis.....	71
10.1. Doppler data extraction from VLBI recordings	71
10.2. The after-landing data set as a calibrator.....	73
10.3. The Green Bank data - a smooth ride data set	76
10.4. Conclusions.....	78
11. WPCCN-1000: Archiving and maintenance of Mk5 disc-packs with raw VLBI data from Huygens VLBI tracking experiment	79
12. Australian Test Geodetic Experiment VT08A	80
12.1. Introduction.....	80
12.2. Experimental Setup.....	80
12.3. Data Processing.....	81

13. WP 6000 and WPCCN-5000: Technology demonstrations for future ESA missions.....	84
13.1. Smart-1 tracking, May - September 2006	84
13.2. Outlook for future missions.....	98
13.3. Huygens VLBI tracking: dissemination of results and outreach	100
14. Conclusions.....	101
15. Acknowledgements	102
16. References.....	103

1. Introduction

This is Final Report on the VLBI Tracking project of the Huygens mission. The goal of the Project was to prepare and conduct VLBI tracking of the Huygens Probe during its parachute descent in the atmosphere of Titan on 14 January 2005. The study continues efforts conducted in the period 2003 – 2008. The report includes key topics reported earlier [1 – 3] and covers in details the period of the Project implementation after the completion of the mission and topics formulated in the corresponding Statements of Work.

Chapters 2 – 5 present the preparation to the Huygens VLBI tracking that involved, among other activities, several test observations of natural celestial sources and spacecraft.

Chapter 6 describes the main VLBI observations of the Huygens Probe conducted on 14 January 2005 and express-processing of the Huygens VLBI tracking data. .

Huygens VLBI data processing algorithms, their implementation and preliminary scientific results, data handling and raw data archiving are presented in chapters 7 – 11.

The auxiliary VLBI experiment which helped to improve the geodetic coordinates of the Australian telescopes is described in chapter 12.

Chapter 13 presents a demonstration of radio astronomy tracking of the Smart-1 spacecraft and gives a brief outlook of future VLBI applications for planetary and other space science missions.

Throughout this report relevant parameters of the mission are assumed to be the same as stated in Section 2 of the report [1].

2. WP 1000: management

2.1. Identification of radio telescopes – potential participants of Huygens VLBI tracking

Contract implementation began in July 2004 from review of conclusions and recommendations described in the reports on the Huygens VLBI Tracking assessment studies described in [1,2]. Particular attention was given to organizing observing and data processing resources required by the project.

Table 2.1. Radio telescopes – potential participants of the Huygens VLBI tracking experiment. Four radio telescopes marked in orange color have been excluded for further considerations based on the assessment of their suitability for the project (see text).

	<i>Telescope</i>	<i>Country</i>	Diameter [m]	T_{sys} [K]	Eff	<i>Status</i>	
						<i>S-band Rx</i>	Mk5
1.	GBT	USA	100	23	0.71	OK	Need
2.	VLBA_SC	USA	25	40	0.48	OK	Need
3.	VLBA_HN	USA	25	32	0.48	OK	Need
4.	VLBA_NL	USA	25	30	0.49	OK	Need
5.	VLBA_FD	USA	25	30	0.55	OK	Need
6.	VLBA_LA	USA	25	30	0.50	OK	Need
7.	VLBA_PT	USA	25	30	0.52	OK	Need
8.	VLBA_KP	USA	25	30	0.55	OK	Need
9.	VLBA_OV	USA	25	25	0.47	OK	Need
10.	VLBA_BR	USA	25	30	0.50	OK	Need
11.	VLBA_MK	USA	25	27	0.45	OK	Need
12.	Algonquin	Canada	46			Need upgrade	Need
13.	Usuda	Japan	70			Need upgrade	Need
14.	Kashima	Japan	34			Need upgrade	OK
15.	Nanshan	China	25			Need upgrade	OK
16.	Sheshan	China	25			Need upgrade	OK
17.	Mopra	Australia	22	36	0.60	OK	Need
18.	Parkes	Australia	64			Need upgrade	Need
19.	Hobart	Australia	26			Need upgrade	Need
20.	Ceduna	Australia	30			Need upgrade	Need

Table 2.1 described originally in [2], represents 20 radio telescopes considered to be suitable in principle for participation in Huygens VLBI tracking. In the course of the present project, it has become clear that it would be impractical to invest in upgrade of the radio telescope in Algonquin: its visibility of the Huygens Field during the probe descent in the atmosphere is too short but the upgrade and operational cost are too high.

The upgradability of the 70-m dish at Usuda (Japan) is being investigated by ISAS/JAXA in September-October 2004. It turned out that the upgrade would require substantial modifications of this main ISAS tracking antenna which would put it out of

normal operations for several months. Such the disruption of operations deemed to be unacceptable.

The two Eastern-most VLBA antennas, Saint Croix and Hancock (VLBA_SC and VLBA_HN) have a very limited sky coverage of the Huygens Field during the Huygens parachute descent and are deemed unnecessary for the experiment.

Operators of other telescopes listed in Table 2.1 have expressed their readiness to participate in the experiment provided their upgrade efforts are properly supported.

2.2. Technical aspects of readiness for Huygens VLBI tracking

According to the results of the Assessment Study, several radio telescopes - potential participants of the Huygens VLBI tracking network required project-specific upgrade.



Fig. 2.1. Mopra 22-m radio telescope (ATNF, Australia, left) and its VLBI DAS electronics (right).

These included some elements of the VLBI digital electronics at the radio telescopes in Australia (e.g. frequency synthesizer and Signal Generator), Fig. 2.1), special adjustment of RF front-ends at the Sheshan and Nanshan radio telescopes in China (tuning down to the non-standard for radio astronomy frequency of 2040 MHz).

A number of potential participants of the experiment by the second half of 2004 were not equipped with the disc-based VLBI data acquisition system (Mk5 or compatible). In particular, the NRAO GBT and several VLBA stations had no Mk5 DAS sets. The EVN Data Processor at JIVE also had insufficient number of Mk5 play-back systems.

During the pre-mission period of the project, the Huygens VLBI tracking team at JIVE in concurrence with the teams at the participating observatories in Europe, Asia, Australia and the United States conducted technical review of readiness for Huygens VLBI tracking and identified areas and components

that required upgrade or modifications. These were addressed by the appropriate actions at the participating observatories and in several cases (e.g. deployment of Mk5 systems at the NRAO GBT and two VLBA antennas (Fig. 2.2) as well as five Mk5 play-back terminals at JIVE) were funded through the current project.

Substantial modifications of the VLBI processing hard- and software instrumentation required by the Huygens VLBI tracking experiment are described chapters 7, 8 and 9 of this report.



Fig. 2.2. ESA-supplied Mk5 VLBI recorders at the NRAO Green Bank (top) and VLBA Pie Town (bottom) telescopes.

3. WP 2000: Description and preparation of the test observation instrumentation and logistics

3.1. Front-end radio telescope instrumentation

The test GG057A conducted on 27 Aug 2004 was designed, in particular, to verify characteristics of telescopes at the Huygens up-link frequency of 2040 MHz. The GBT and VLBA antennas need no modifications to operate at this frequency. Minor upgrade was required at Mopra (in particular, a new LO synthesizer and filters were installed).

The signal path at Parkes, Ceduna and Hobart telescopes were modified in preparation for the test GG057B of 17 November 2004. The test results demonstrated the quality of the modifications.

The upgrade of the Sheshan telescope (primarily – the new feed for the frequency of 2 GHz) was completed by the end of November 2004. Details of the upgrade have been discussed in mid December 2004 during the visit in China by L. Gurvitsm and documented at the Shanghai Astronomical Observatory.

The overall summary of the telescope performance at 2040 MHz was made available after completion of the data reduction of the experiment GG057B. This summary served as an input for calibrating the data of the “live” Huygens tracking (chapter 8).

3.2. Digital back-end radio telescope instrumentation and related software

The NRAO telescopes involved in the experiment did not require significant modifications of their pre-data-recording devices for the Huygens VLBI Tracking experiment. However, substantial changes were needed in the VLBA control system software and GBT control software. These software modifications were implemented by the NRAO personnel (mostly – by W. Brisken). R.C.Walker (NRAO) together with C. Reynolds (JIVE) modified the main VLBI scheduling tool – the program SCHED – in such the way that it could handle Mk5 scheduling for the Huygens VLBI Tracking experiment.

Digital back-end modifications at all three non-Mk5 telescopes in Australia (Parkes, Ceduna, Mopra) were very substantial. The modifications were tested in the observation GG057B (17 November 2004). Details of the test are described in [3] and also include results of the “local” Australian test TH024.

The three “genuine” Mk5-equipped telescopes (Hobart, Sheshan and Nanshan) did not require any modifications of their digital back-end instrumentation.

The telescope at Kashima was equipped with a generic K5 digital instrumentation. The test GG057B (2004.11.17) was the first attempt to combine K5 and Mk5 data in one VLBI experiment with Huygens-specific set-up. This test proved to be successful and provided useful “training ground” for the “live” Huygens VLBI experiment.

3.3. Data recording and processing instrumentation

In preparation for the “general rehearsal” test of GG057B, all 16 telescopes shown in Table 2.1 were equipped with Mk5 or Mk5-compatible recording systems.

Hobart, Sheshan and Nanshan used Mk5 systems as their standard recording environment, no special modifications were needed for the Huygens VLBI tracking.

The GBT and two VLBA stations were equipped with an ESA-supplied Mk5 system by the time of the test GG057A (27 August 2004). These have remained at the sites through the completion of the project. In addition, one more VLBA station, Pie Town was equipped with Mk5 system by NRAO. For the test GG057B and the “live” observation of 14 January 2005, further 5 Mk5 systems have been deployed at the VLBA sites (two supplied by NRAO, and three – by NASA). Therefore, from November 2004 on, 8 VLBA sites (all but VLBA_HN and VLBA_SC – see Table 2.1) and GBT have been equipped with Mk5 systems.

Recording at Parkes, Mopra and Ceduna has been conducted with a hybrid system based on the PCEVN/MRO and S2 elements. The data were recorded on disks for further translation into Mk5-compatible format at JIVE. The latter work has been done in collaboration with the Helsinki University of Technology. The first test GG057A has demonstrated the feasibility of the translation procedure.

Due to spacecraft constraints, the full array was not visible to the Cassini during X band transmission. Therefore the array was split into two sub-arrays: an Eastern array consisting of Westerbork, GBT and four VLBA stations (Pt, NI, La, Fd) which could see Cassini, and a Western array (VLBA stations Br and Mk, Parkes, Hobart, Mopra, Sheshan, Nanshan). The two sub-arrays did not observe the same sources.

4.2. Radio telescope array

The telescope array involved in the test GG057A involved the GBT, 8 VLBA antennas, Parkes, Mopra, Hobart, Sheshan. The Nanshan telescope, originally scheduled for GG057A, could not participate due to a scheduling conflict. Mopra and Hobart experienced failures of local hardware and power supplies unrelated directly to the Huygens-specific hardware. That prevented them from producing useful data. Other telescopes observed according to the schedule as described in the following sections.

4.3. Scheduling issues, logistics and operational feedback

VLBI observations are conducted on arrays of telescopes with quite different characteristics: drive and elevation limits, frequency coverage, available LO settings, and recording media are some of the parameters that constrain observations. The widely-used SCHED software package maintains a database of station characteristics. In several ways GG057A foiled the self-consistency checks SCHED applies to one's experimental setup. The non-standard S-band frequencies were outside the nominal coverage at some stations, so ad-hoc database entries were inserted. The mixture of recording media (Mk5-disk, Mk4-tape, PCEVN-disk) was indirectly a problem: attempting to schedule some VLBA stations with different data rates than others confused the control-file writing routines for non-VLBA stations. These problems were either overcome during schedule preparation, or at the telescopes by operators, or are currently being addressed by the software maintainers. The overall distribution of LO settings is shown in Table 4.1.

The schedule went through at least four revisions to deal with these problems leading up to the observation, and in particular some last-minute tweaking for the VLBA. In the end, there was no delay or data loss due to the non-standard observation parameters. Hobart had problems with the formatter, and Mopra's control computer had a system disk crash.

The following stations recorded data for correlation at JIVE: Westerbork (Mk5), Green Bank (Mk5), Fort Davis (Mk5) Kit Peak (Mk5), Los Alamos (Mk5), North Liberty (Mk5), Pie Town (Mk5), Brewster (Mk4), Mauna Kea (Mk4), Parkes (PCEVN), Shanghai (Mk5). Figure 4.3.1 shows the frequencies observed by the two subarrays. After observation, Mk5 disk-packs and Mk4 tapes were shipped to JIVE in the usual manner. The PCEVN disks from Parkes were received at JIVE and translated to MK5 format as described in section 5.2.

4.4. Data processing

The two subarrays were processed separately at the EVN correlator. Fringes were detected to all stations at which they were expected. Some special effort was required because of observing irregularities, such as swapped IF channels or polarisations. These kinds of problems are common in VLBI observations and it's not surprising several of them were encountered in GG057A. They were corrected or ameliorated during processing owing to the built-in flexibility of the correlator.

The Cassini signal was detected at X band in auto- and crosscorrelation spectra at all stations which observed the spacecraft.

Further details of the evaluation of the preparatory test observations GG057A&B as well as other tests are presented in the reports [1-2].

5. Huygens VLBI project data processing setup at JIVE

As described in [1,2] the data processing for VLBI tracking of the Huygens probe consists of two parts: detection and phase tracking of a narrow-band carrier signal, and broad-band correlation of signals from background celestial radio sources for proper phase calibration of the detected carrier phase. The second part will be done by the EVN Mark4/Mark5 VLBI Correlator at JIVE in a standard way, provided broad-band data is recorded on standard VLBI recording media, i.e. disk-based Mark5 units or compatible equipment.

Extraction and processing of the narrow band probe signal, as well as data conversion from Mark5-compatible recording platforms into actual Mark5 format has to be done on a dedicated hardware platform. As part of the Huygens activity at JIVE, the “Phase 1” setup was developed. Fig. 5.1 illustrates the current status of hardware used for development, testing and evaluation of the signal processing software and operational processing of the Huygens related VLBI data sets from GG057A, a Global VLBI observation project.

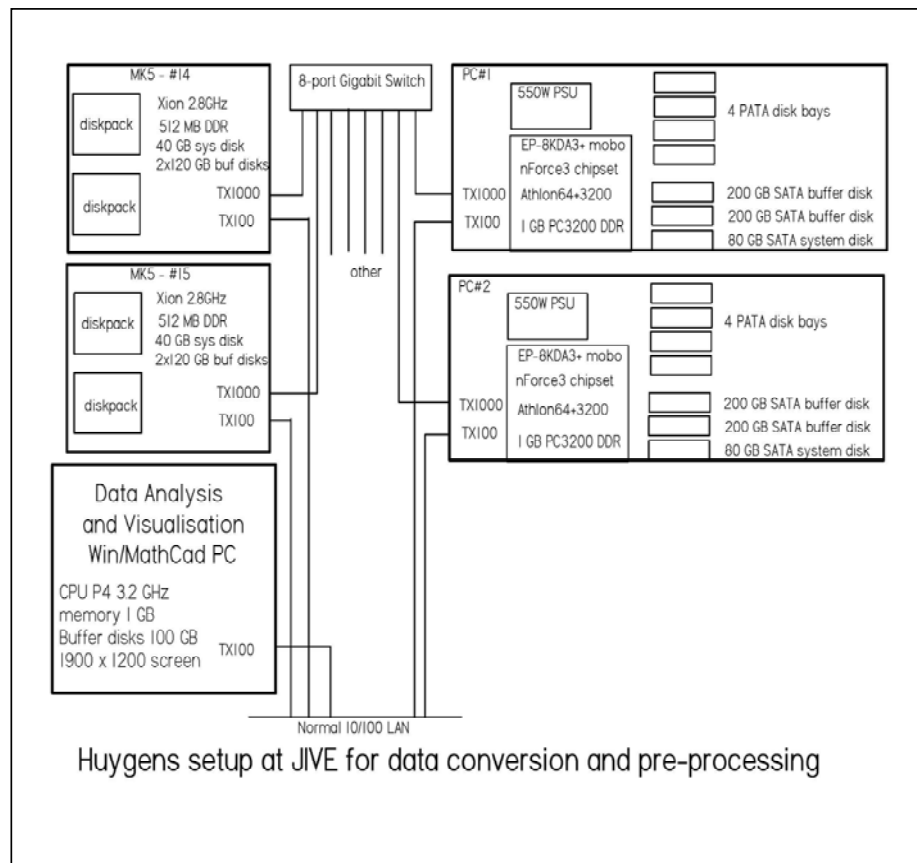


Fig. 5.1. Phase 1 hardware set-up for Huygens VLBI data processing at JIVE

The current set-up includes two upgraded Mark5 units with more advanced motherboards and two high-end Linux PCs with equivalent disk handling capability up to 4 TB. Local Gigabit Ethernet network and a data analysis workstation complete the setup. Two major software development tasks were exercised on this platform:

(a) narrow band signal extraction from broad-band Mark5 data and (b) data format conversion between ATNF and Mark5 recording systems.

We consider this Phase 1 set-up (Fig. 5.1) as a test-bench because it has provided estimates on actual processing power required completing the above mentioned tasks for the “live” Huygens observations on 14 January 2005 within a reasonable time.

5.1. Narrow band signal extraction and analysis

The Mark5 data recorder/playback unit can handle a data rate up to 1 Gbps. For the GG057A observations we recorded 512 Mbps, and the same mode was used for the Huygens Probe observations on 14.01.2005. This mode records data from 8 independent 16 MHz-wide video bands. All these bands are necessary for successful detection of phase referencing background radio source calibrators, while the probe signal itself can be represented in a band of several kHz (taking into account the range of possible Doppler shifts). As the probe signal can be highly elliptically polarized at large angles between probe antenna apex and our line of sight, we need to record and analyze both circular polarizations.

Special software was developed at JIVE to extract the required band width from broad-band Mark5 data. This extraction is done in several steps:

1. Copy blocks of the full 512 Mbps data from Mark5 units to general-purpose computers (Linux PCs as shown in Figure 5.1) employing the standard Mark5 Disk2Net/Net2File functions.
2. Extract from the Mark5 data the channels corresponding to the 16-MHz wide sub-bands and polarizations of interest, and store them on disk as another file. Special attention is paid to provide correct timing of extracted signal with respect to intrinsic time stamps of VLBA/Mark5 data. Sampler statistics are also computed at this stage to check that the VLBA data demodulation and sign/magnitude bit decoding are correct. We use +7 +2 -2 -7 coding for the extracted 2-bit per sample signals and pack 2 channels (RCP and LCP) into one byte of the output file. Although it's not as effective in terms of disk space usage, this coding has advantages for later stages of signal processing. The channel data extraction function is written in standard ANSI C.
3. Process the 16 MHz data file with a software base band conversion (BBC) procedure, which extracts the required narrow band within the 16 MHz sub-band. Current implementation of the Software BBC insures mutual phase coherency between the parent 16 MHz band and the extracted narrow band, and allows a wide range of software BBC settings. At this stage the full bandwidth power spectra are also computed. Filtered narrow-band data streams and broad-band power spectra are stored on disk. Examples of computed full band power spectra for GG057A observations of the Cassini spacecraft at X-band are presented in Fig. 5.2. Implementation of the Software BBC in C is based on a “Hopping FFT” technique and use of the FFTW library. The input FFT length can be as long as 256K samples, although we prefer 256000 (radix $5^3 2^{11}$) because it gives “Integer Hz” frequency binning in both input and output bands (125 Hz per bin) and allows software LO in stepping coherent to that of the Mark4 or VLBA data acquisition systems and the correlator LO. As a rule, the averaged power spectrum provided has the same frequency resolution as the primary FFT of the software BBC, although Hamming smoothing is optional.

4. Further down stream the narrow-band data is transferred to a data analysis workstation. The extracted narrow bands (100 – 10 kHz wide) are further processed in order to detect and track the spacecraft carrier line phase. Fig. 5.3 shows detection of the Cassini spacecraft transmitter carrier line at all six participating VLBA stations (including GBT). In this example we extracted a 15.625 kHz-wide band starting from 11.270 MHz in the 16 MHz band (1:1024 data filtering). The search for the carrier line was done with 1 Hz resolution. In Fig. 5.3 only 100 Hz of the 15.625 kHz band are plotted to show the Doppler shift of carrier line frequency. Segments are centred at the expected topocentric frequencies for each station; no correction for telescope motion was applied. A Doppler shift rate of the order of 0.4 Hz/second is mainly due to the proper motion of the spacecraft.

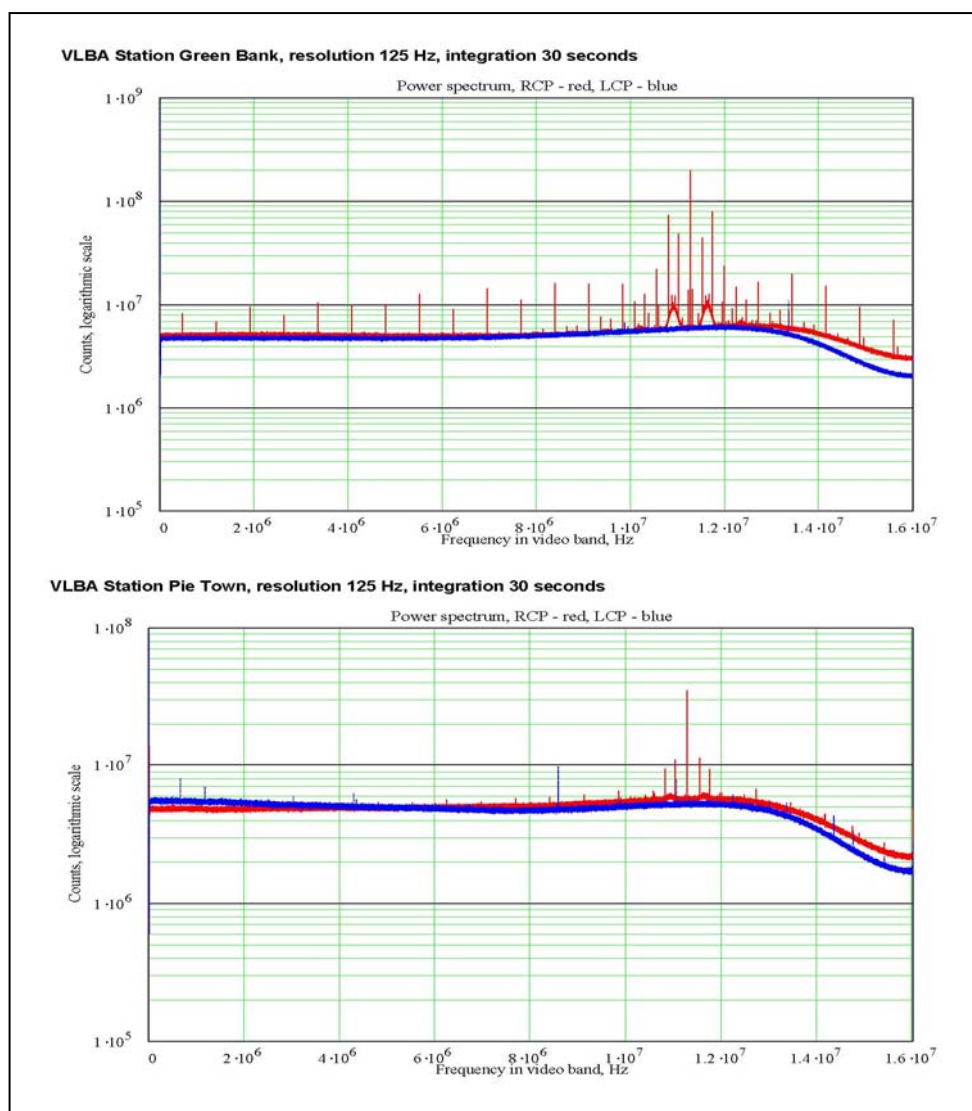


Fig. 5.2. Power spectra over 16 MHz in X-band observed at the GBT and VLBA Pie Town station in the GG057A test. Antenna pointing: Cassini S/C. The line forest seen in the GBT spectrum is due to cross-products between the carrier and sub-carrier lines caused by the strong signal and 2-bit sampling

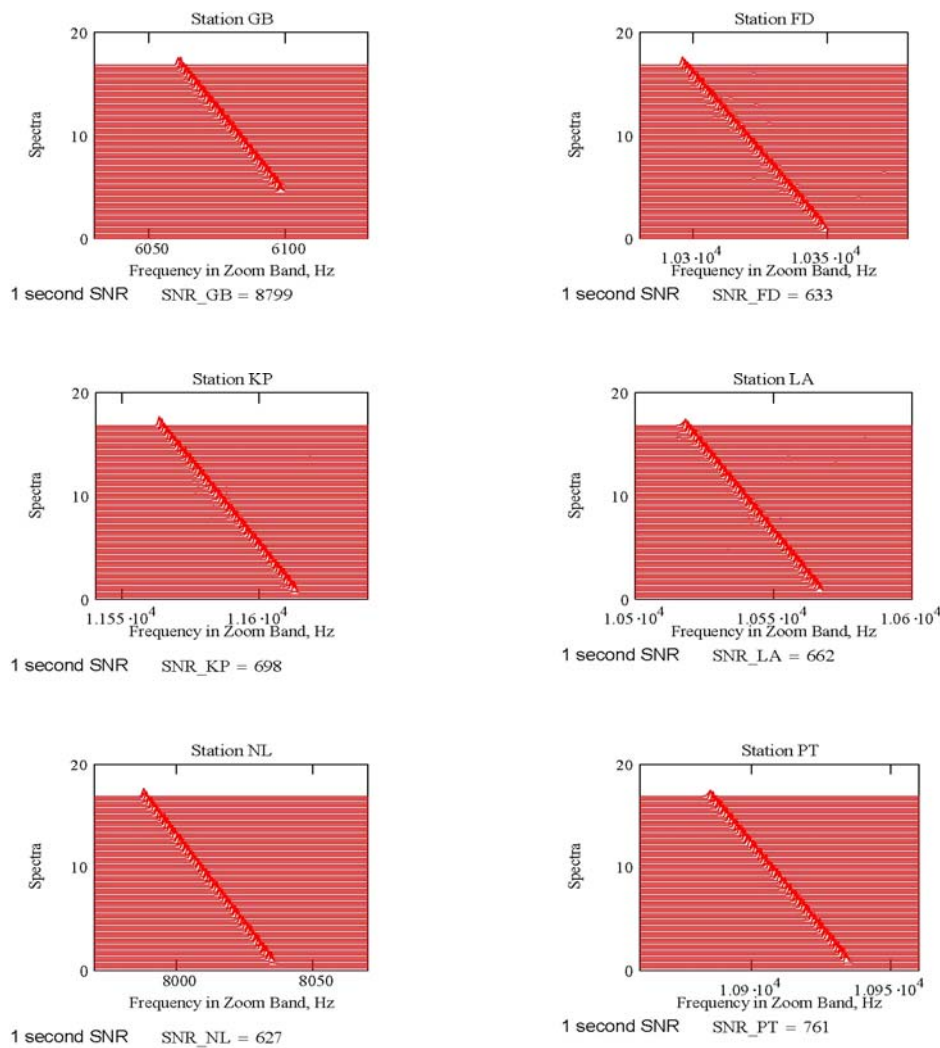
In the current state of the software, the processing pipeline (including data transfer from Mark5s to PCs, base-band extraction, and narrow-band extraction) runs with a coefficient of 12-15 with respect to observed time. To avoid a possible bottleneck in the Huygens data reduction (about 100 hours of aggregate observing time) proper effort in software development is due. Augmenting computing power and equipping more Mark5 units with Gigabit Ethernet cards is also planned. Upgrading the processing PCs with 400GB-disk-based raids on both SATA and PATA controllers will allow us to buffer the full 6 hour data set from a Mark5 disk pack and process it in one go with minimal human attendance.

5.2. PCEVN/MRO-to-Mark5 data conversion

During the GG057A VLBI observing run, the ATNF Parkes 64-meter radio telescope observed the radio source J0019+2021 simultaneously with Shanghai Radio Observatory (which used a Mark4 data acquisition system and a Mark5 recorder) and VLBA stations Mauna Kea and Brewster (both using VLBA DAS's and recording on magnetic tape). Both Mark4-on-Mark5 and VLBA-on-Tape are standard data handling media for the EVN Correlator at JIVE, while Parkes data was recorded using the so-called ATNF DAS data acquisition system sampling four 16 MHz-wide video bands with 2 bits each at 32 Msps, producing an aggregate raw data flow of 256 Mbps. ATNF DAS bit stream outputs were converted to VSI-H (VLBI Standard Interface, see <http://web.haystack.edu/vsi/>) LVDS signal and connector conventions using the "VSIC" universal VSI converter board (see <http://kurp.hut.fi/vlbi/instr/boards/>) and recorded into regular Linux files with the "VSIB" VSI-to-PCI record board (both boards developed at Metsähovi Radio Observatory). To facilitate a sufficient data rate, a two-disk Linux RAID0 disk set was used to record the files. The recorded files were time-stamped and augmented with auxiliary data headers.

In order to correlate ATNF data against VLBA or EVN data we have to convert it to a format acceptable by the correlator.

For this purpose special software (the so-called Software Formatter) was developed at the Metsähovi Radio Observatory of the Helsinki University of Technology (Finalnd).



Dynamic spectra of carrier line in the 16 KHz zoom band, 90 seconds scan, 1 second sampling, 1 Hz resolution

Fig. 5.3. High-resolution dynamic spectra of the Cassini spacecraft X-band carrier line observed during experiment GG057A. Only a 100 Hz wide segment of the 15625 Hz-wide zoom band (software BBC output) is shown. Doppler shift rate is mainly due to the proper motion of the spacecraft.

The two-disk RAID0 set was transported from Australia to JIVE where the disks were mounted in the PATA bays of PC#1, shown in Fig. 5.1. Time code information from the file headers was checked and the raw sampled data was software formatted into Mark4-on-Mark5 format with this time code information. The resulting Mark5-compatible files were concatenated and bulk-transferred to the Mark5A unit (shown in Fig. 5.1 as "MK5 - #14") using a gigabit Ethernet connection and "File2net"/"Net2disk" TCP network transmission programs in the standard Mark5 software package. The resulting Mark5A 8-disk pack of formatted data was correlated in the same fashion as all other Mark5A disk packs, demonstrating that

software formatting produces data comparable to "native" Mark4/5 hardware equipment.

Finally, Parkes data was correlated with the EVN and VLBA data, showing fringe detection on all baselines and all observed sub-bands. To allow the correlator to process ATNF data also took some effort to compose a correlator control VEX file describing Parkes as a "virtual Mark5" station. Figure 5.4 illustrates the resulting correlation functions.

Single sub-band data extraction for the ATNF data (similar to that of the VLBA data processing described above) is also a part of the software package developed at Metsähovi Radio Observatory, although it was not tested with currently available data as Parkes did not participate in the Cassini observation during GG057A. Such a test as well as software formatting of 512 Mbps data rate is a subject for further work.

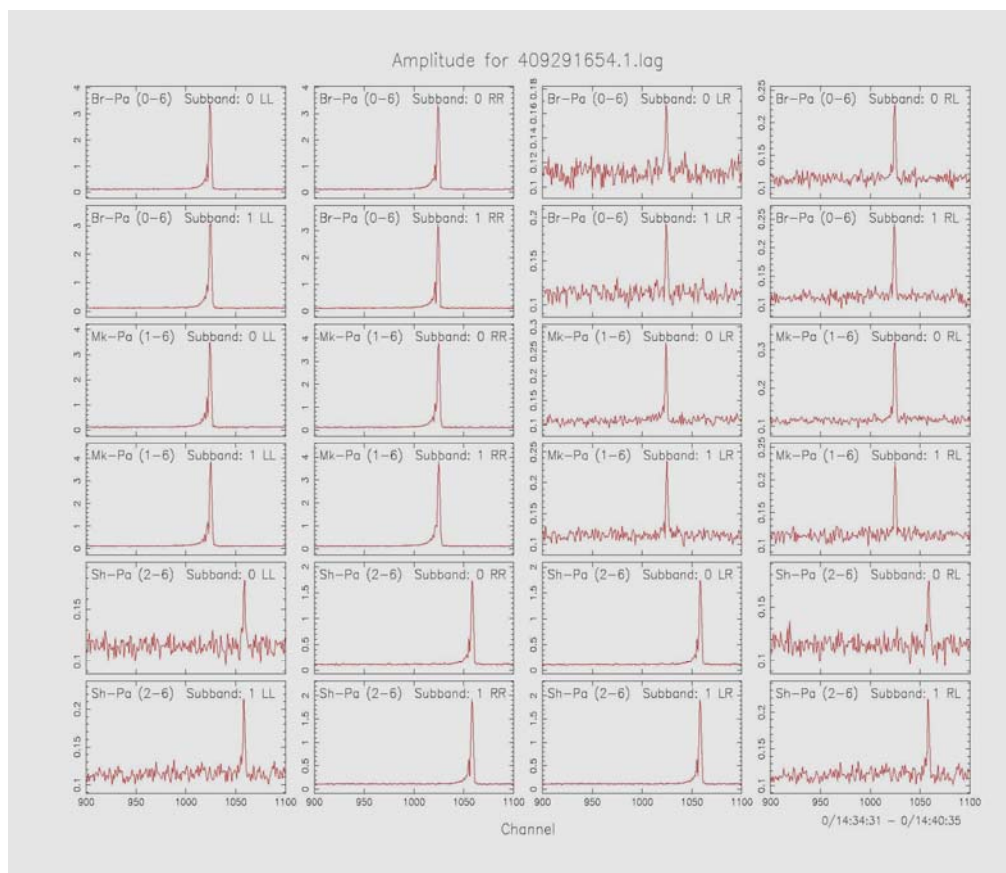


Fig. 5.4. Source J0019+2021 observed during experiment GG057A. Fringes on baselines Mauna Kea, Brewster and Shanghai to Parkes. Parkes data were converted from ATNF format to Mark5 before correlation. Shanghai observed with Mark5, Brewster and Mauna Kea with tapes.

The processing speed of reading the raw data, software formatting it in memory, and writing the formatted data to another set of disks is reasonably fast (approximately 550—600 Mbps), even for the future full-rate 512 Mbps data. Due to an interrupt conflict between the Gigabit Ethernet controller and SATA RAID controller on the EP-8KDA3+ motherboard we had to use an additional file copy step, which slows down the aggregate processing throughput to about 300 Mbps. Transferring the formatted data from the Linux PC to the Mk5 unit using “File2net+Net2disk” over Gigabit Ethernet also increases the elapsed time. With two PC-units and two target Mark5A units working in parallel the full set of ATNF Huygens observation data can be pre-processed in a reasonable amount of time. Equipping the existing PCs with bigger SATA disks will also make the processing pipeline run more smoothly and automatically, which is an important goal of the project.

6. WP 5000: Huygens VLBI Tracking observation 14 January 2005 (GG057C)

6.1. Observing strategy, preparatory status, personnel functions

The main Huygens VLBI observation (global VLBI experiment GG057C) was organised and scheduled according to the operational requirements of the global VLBI network. It involved 17 radio telescopes, all of them verified and tested earlier in the course of two major global Huygens VLBI test runs GG057A and GG057B. The list of radio telescopes is presented in Table 6.1. Note that three different data acquisition control systems, VLBA, VEX (Mk4) and VSOP ought to be used in GG057C. Two of the telescopes, ATCA (Australia) and Urumqi (China) were not involved in receiving the Huygens carrier signal at 2040 MHz (due to incompatibility of their receivers), but participated in the observation of continuum calibrator sources in order to phase-up the network.

Table 6.1. Radio telescope of the observation GG057C

Station	Control	Scans	Scan Hours	Comments
GBT	VLBA	113	3.08	
VLBA_PT	VLBA	194	5.20	On-Titan continuously
VLBA_KP	VLBA	194	5.20	
VLBA_LA	VLBA	184	4.95	
VLBA_BR	VLBA	217	5.77	
VLBA_FD	VLBA	174	4.70	
VLBA_NL	VLBA	154	4.20	
VLBA_OV	VLBA	217	5.77	On-Titan continuously
VLBA_MK	VLBA	217	5.77	
PARKES	VEX	134	3.61	
HOBART	VEX	229	6.13	
MOPRA	VEX	227	6.08	
CEDUNA	VEX	225	6.03	
SHANGHAI	VEX	232	6.11	
KASHIMA	VSOP	255	7.05	
ATCA	VEX	233	6.23	Continuum calibration
URUMQI	VEX	171	4.41	Continuum calibration

The observation schedule began at 09:00 UTC from several scans on continuum calibrator sources DA193 and J0728+2153. From 09:30 UTC, all telescopes which could see Titan were switched to the main phase-referencing cycle of pointing to Titan and the calibrator source J0744+2120. The duty cycle of phase-referencing was 110 s – 70 s (including slewing), with the first scan on Titan (Huygens), and the second one – on the calibrator source (both durations included slewing between the sources, amounting from several to ten seconds at various telescopes).

All telescopes listed in Table 6.1 participated in VLBI data acquisition, and the overall observing schedule of the radio astronomy segment of the Huygens mission was driven by VLBI observations. In addition to VLBI, two other radio astronomy experiments were conducted at a sub-set of telescopes listed in Table 6.1. These included direct Doppler measurements with the NASA-DSN supplied Radio Science Receiver (RSR) and PC-based Digital Doppler Recorders (DDR). Both RSR and

DDR measurements were conducted by JPL teams. The RSR units, capable of real time signal detection were installed at the two largest telescopes of the network, GBT and Parkes. The DDR units were installed at VLBA_PT, VLBA_KP, VLBA_OV and VLBA_MK. Fig. 6.1 Represents the observing configuration in the beginning and end of the experiment.

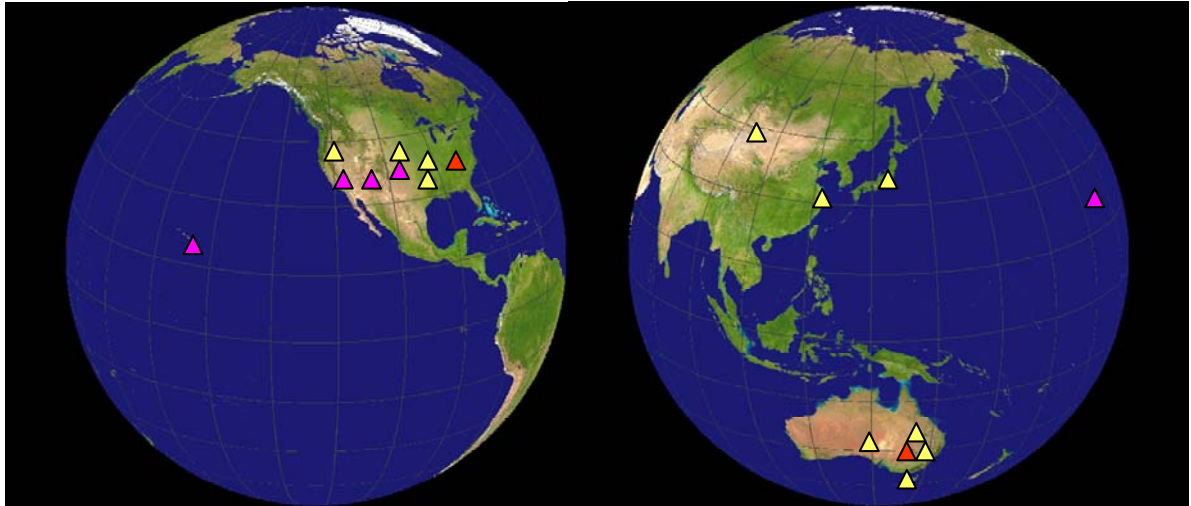


Fig. 6.1. Configuration of the radio telescopes as seen from Titan at the beginning of the observation (left panel) and end (right panel). The GBT and Parkes telescopes (shown in red) were equipped with both VLBI and RSR data acquisition systems., VLBA antennas Pie Town, Pitt Peak, Owens Valley and Mauna Kea (shown in plum) were equipped with VLBI and DDR recorders.

The observation began about half an hour before Huygens signal arrived to Earth and stopped at 16:00 UTC (~14:53 SCET/UTC). All 17 radio telescopes participated in the VLBI observation. Two telescopes shown in red colour, the NRAO R.C. Byrd Green Bank Telescope and CSIRO Parkes Telescope, were equipped in addition to the VLBI data acquisition system by the NASA DSN Radio Science Receiver (RSR) with real-time detection capability. Four NRAO VLBA telescopes shown in purple (Pie Town, Kitt Peak, Owens Valley and Mauna Kea) in addition to VLBI observations conducted also NASA/JPL-led direct Doppler measurements of the Huygens radial velocity (in Earth-bound coordinate system) using the DDR recording system

Phase-referencing of the Huygens carrier signal required interleaved pointings at Huygens and phase-referencing source J0728+2153. However, it was desirable to leave two DDR-equipped antennas on-Titan during the entire observations. Thus, two VLBA antennas, were not involved in nodding phase-referencing, VLBA_PT and VLBA_OV.

Table 6.2 summarizes the on-schedule duration in the GG057C observation for all involved radio telescopes on 14 January 2005.

Table 6.2. Summary of the on-schedule duration of the GG057C observation 14 January 2005

	Telescope	Institute, country	Diameter [m]	Observing time (ERT/UTC)	
				Start	Stop
1	Green Bank (GBT)	NRAO, USA	100	09:31:10	12:15:00
2	VLBA North Liberty	NRAO, USA	25	09:31:10	13:15:00
3	VLBA Fort Davis	NRAO, USA	25	09:31:10	13:45:00
4	VLBA Los Alamos	NRAO, USA	25	09:31:10	14:00:00
5	VLBA Pie Town	NRAO, USA	25	09:31:10	14:15:04
6	VLBA Kitt Peak	NRAO, USA	25	09:31:10	14:15:00
7	VLBA Owens Valley	NRAO, USA	25	09:30:09	14:49:14
8	VLBA Brewster	NRAO, USA	25	09:31:10	14:48:00
9	VLBA Mauna Kea	NRAO, USA	25	09:31:10	16:00:00
10	Kashima	NIICT, Japan	34	09:31:10	16:00:00
11	Sheshan (Shanghai)	NAOC & ShAO, China	25	10:01:10	16:00:00
13	Nanshan (Urumqi)	NAOC, China	25	11:31:10	16:00:00
14	Mopra	ATNF, Australia	22	10:10:10	16:00:00
15	Parkes	ATNF, Australia	70	12:26:23	16:00:00
16	Hobart	U Tasmania, Australia	26	11:13:10	16:00:00
17	Ceduna	U Tasmania Australia	30	10:13:10	16:00:00

6.2. Express “next morning” results and evaluation



Fig. 6.2. A.Tzioumis and C.Phillips (ATNF) carry a box with the disks containing Huygens VLBI tracking data to the charter plane (in the background), around 03:45 local time, 15 January 2005, Mopra, Australia.

Express evaluation of the data obtained in the Huygens observing run GG057C was not foreseen in the current contract. However, based on the know-how developed at JIVE over the months preceding the Huygens VLBI experiment and eVLBI world-wide collaboration. The express evaluation deemed to be a useful a posteriori check of the overall performance of the Earth-base radio astronomy segment of the Huygens mission. Of the 17 radio telescopes involved in GG057C, several telescopes in Australia were chosen as participants of the “near-real-time” e-VLBI verification tests. The reason for this choice was based on the fact that only Australian telescopes from the Huygens VLBI tracking network had been involved in successful e-VLBI tests with the EVN correlator at JIVE prior the GG057C run. The express evaluation involved two ATNF

telescopes, Parkes and Mopra.

Immediately after the end of the Huygens VLBI observing run at 16:30 UTC on 14 January 205 (03:30 15 January local time in Australia) the data stored on PCEVN disks were transported by a chartered Cessna via Narrabri, Coonabrabran (Mopra) and Parkes to the ATNF headquarters in Sydney (Fig. 6.2).

Two 13-minutes segments of data from Parkes and Mopra (100 GB total) containing scans on the calibrator source were relayed to JIVE with the speed up to 300 Mbit/s via a specially arranged network going from Australia to Canada via Pacific, across North America to New York, and then across Atlantic to The Netherlands (Fig. 6.3)..

The data provided by Mopra and Parkes were recorded on PCEVN recorders. The team of the Metsähovi Radio Observatory of the Helsinki University of Technology, Finland (A. Mujunen, J. Ritakari) translated the data into the Mk5 format remotely (from Helsinki) after the data were loaded on the JIVE computers.

The JIVE correlator team then immediately started correlation. Interferometric fringes were found within about an hour (i.e. by about 06:00 15 January local time in Europe) confirming correctness of the observational setup. As this setup was identical at all 17 radio telescopes, it was a strong indication that the overall experiment should have no problems due to incorrect setting. Coupled with the fact of solid Huygens carrier detection at GBT and Parkes by the Radio Science Receiver (RSR), it enabled the VLBI tracking team to conclude that the overall experiment should accomplish the goal.

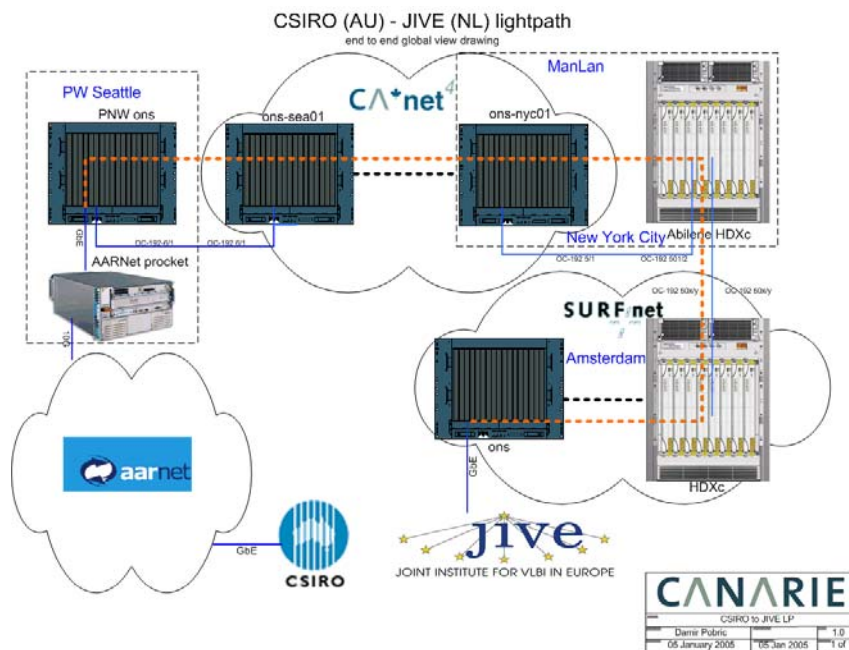


Fig. 6.3. Add-hoc signal-path from Australia (CSIRO) to JIVE for the Huygens VLBI tracking experiment.

An example of the interferometric response on the calibrator signal on the baseline Mopra – Parkes was demonstrated at the Huygens mission briefing at ESOC at 09:00 CET on 15 January 2005. Fig. 6.4 represents the plot shown at the briefing, confirmed correctness of the non-standard VLBI setup of the Huygens VLBI tracking experiment. Combined with the earlier detection of the Huygens Channel A carrier signal at GBT and Parkes with the JPL’s RSR, this result re-assured the participants of the mission that the failure of the communication line between Huygens and Cassini via Channel A and subsequent unavailability of the Doppler Wind Experiment data on the line “Cassini-Huygens” would be fully remedied by the data collected at the Earth-based radio telescopes.

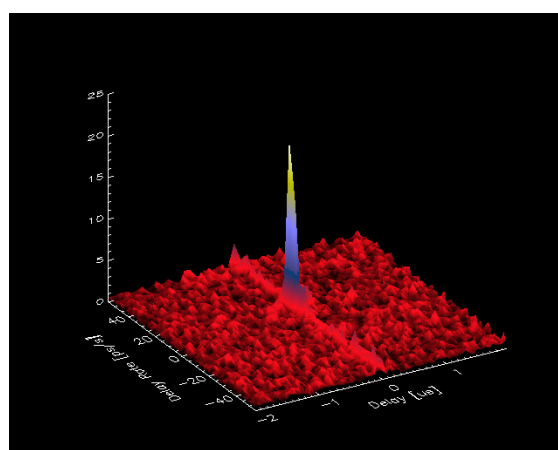


Fig. 6.4. An interferometric detection of a calibrator source in the GG057C experiment on the baseline Parkes-Mopra obtained by means of e-VLBI transfer of data from Australia to JIVE (The Netherlands) a few hours after completion of the Huygens transmission from Titan.

7. Software for fast processing of pre-filtered Huygens data

7.1. Introduction

Processing of the Huygens descent data as received by the radio telescopes involves many steps. This chapter describes the iteration loop and software which processes the pre-filtered Huygens data until the phase correction model is determined accurately enough. The phase correction is a measure for the Huygens motion in the Titan atmosphere. Fig. 7.1 shows the place of the iteration loop in the complete processing chain.

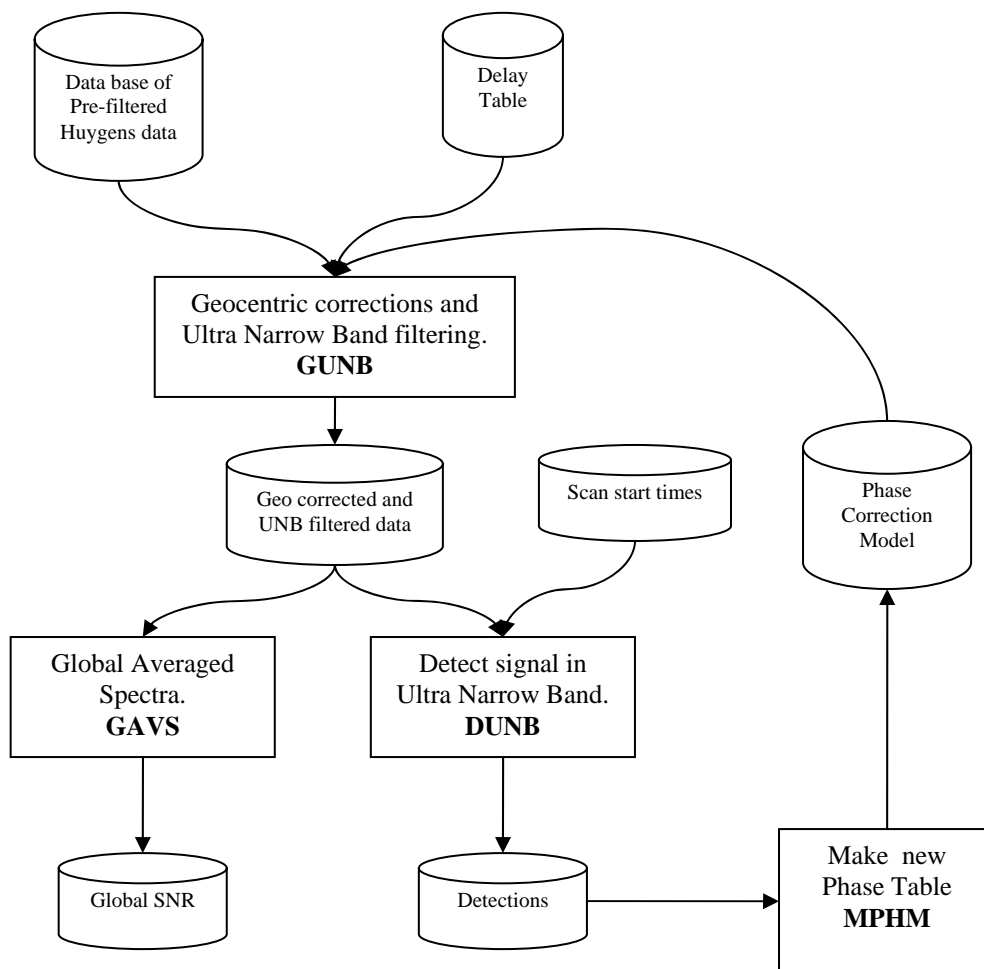


Fig. 7.1. Major processing steps for the pre-filtered data. Bold face: application name

In the first step (GUNB) the pre-filtered data are corrected for Titan motion with respect to centre of Earth and geocentric station positions. This delay table is pre-calculated. These data are then filtered down with a tracking filter into in an ultra narrow band filter (UNB). The next step (DUNB) looks for detections of the Huygens signal in the UNB data and at the same time the global SNR is determined as a monitoring parameter (GAVS). The detection results are used as input for the last step (MPHM) to calculate the new phase correction model to be used as input for the

next iteration loop. The ultimate goal of the iteration process is to obtain an accurate phase correction model, which is a measure for the Huygens motion in the Titan atmosphere along the line of sight.

7.2. The software application design

In the earlier stages of the Huygens project various Mathcad [6] applications were used for processing the pre-filtered data. These worked fine in the software development phase. As the processing of the data progressed, a clearer image emerged how data should be processed. So the next step was to speed up the processing. For this purpose C applications were developed. The functional design of these C applications is described in the coming sections. The MathCAD code served as the C software design prototype.

GUNB is the application which applies the geocentric corrections and the UNB filtering. The primary data base for processing consists of pre-filtered data files (*.fl) which represent the observed signals in a band width of 15625 Hz and are two times over-sampled. A typical size of these files is about 1 GB for 1 hour of observations per station. Total amount of data for the stations GB, PA, BR, CD, FD, KP, MK, MP, OV and PT comprises more than 100 GB. For safety reasons this data base is 4 times copied on different hard disks and also has backups on DVD and DLT.

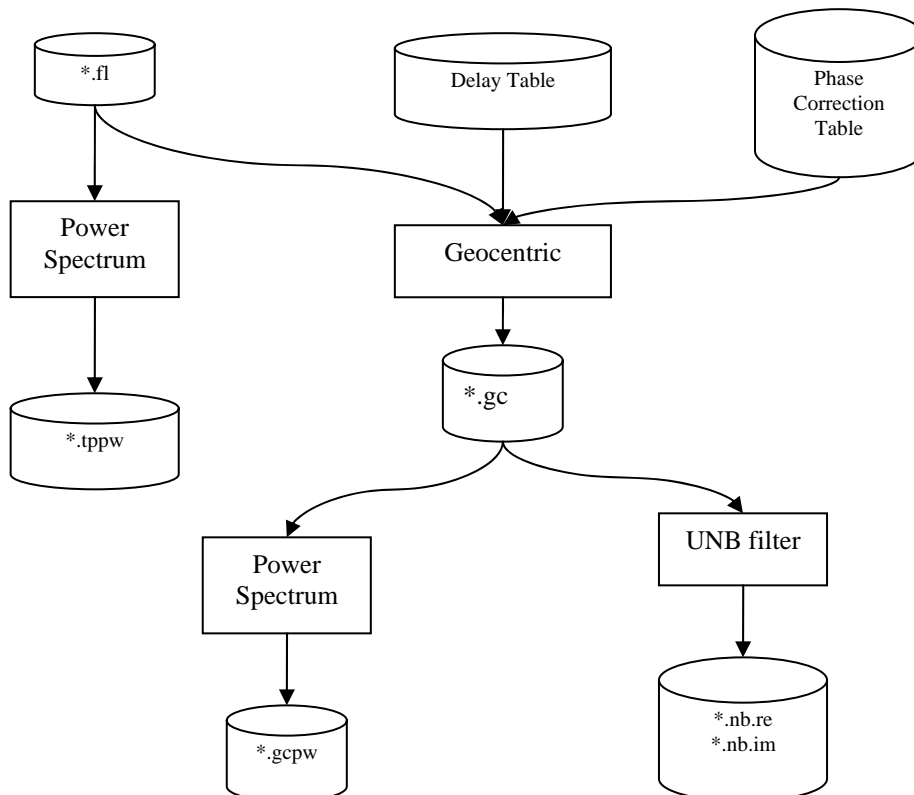


Fig. 7.2. Processing steps and data in GUNB

The pre-filtered data in the *.fl files (time domain) are used as input for the Power Spectrum function. It generates the topocentric power spectrum (frequency domain,

*.tppw files – Fig. 7.3). The data of the more powerful radio telescopes show a clear spectral line in the surrounding noise as can be seen in the data from the Green Bank radio telescope.

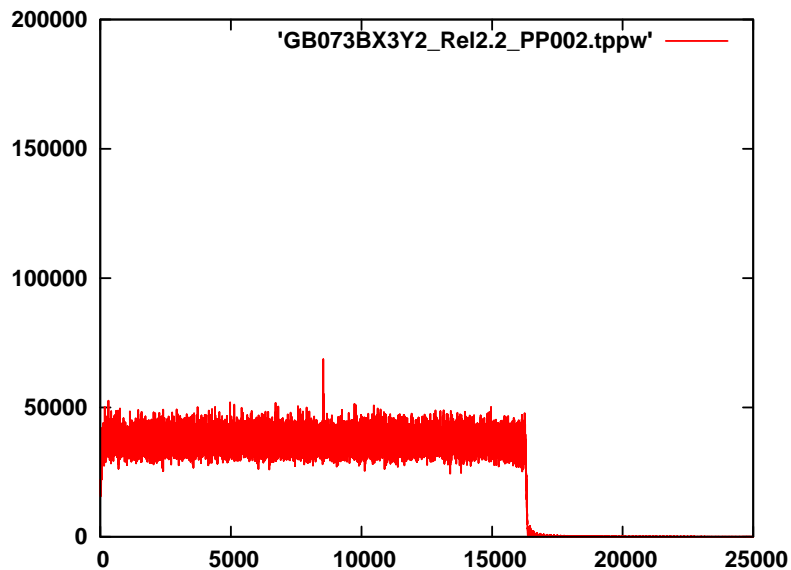


Fig. 7.3. Topocentric power spectrum without geocentric correction.

However the data in the topocentric power spectra (*.tppw files) are not an end product. They are merely used to check if there is a signal in the data. The next processing step comprises the correction of the data in the *.fl files for Titan motion and signal delay with respect to the Earth centre. These geocentric corrections were computed by CALC [5], which is a software package developed over many years by GSFC that can compute radio telescope positions as a function of time in the celestial reference frame, taking into account conventional models for the terrestrial/celestial transformation, the geo-potential, and tidal loading displacements of terrestrial reference points. Delays were computed from these CALC positions and a JPL ephemeris of Titan [6]. They are written to the Delay Table.

GUNB uses the data from the Delay Table to apply the geocentric corrections and saves them in *.gc files (time domain). A typical power spectrum for these corrected data is shown in Fig. 7.4 together with the uncorrected data. The signal is now much stronger and right shifted.

The UNB filter extracts the data in an ultra narrow band from the *.gc files and saves the real and imaginary filtered data in *.nb.re and *.nb.im files (time domain). During the processing the UNB width was gradually narrowed down following the progress of signal phase tracking. We started with 2 kHz and currently it is just 20 Hz with actual analysis width of about 3 Hz. Taking into account that primary MK5 data has a bandwidth 16 MHz we can say that about 1:1000000 filtering ratio is achieved.

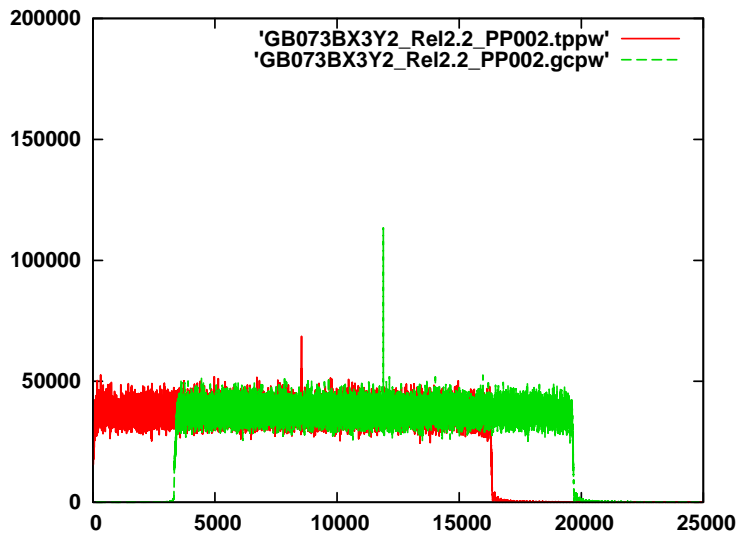


Fig.7.4. The effect of geocentric corrections on the power spectrum.

DUNB is the application which calculates the frequency and power detections from the UNB filtered data (Fig. 7.5). In the first step the time domain data in the *.nb.re file is divided into time segments.

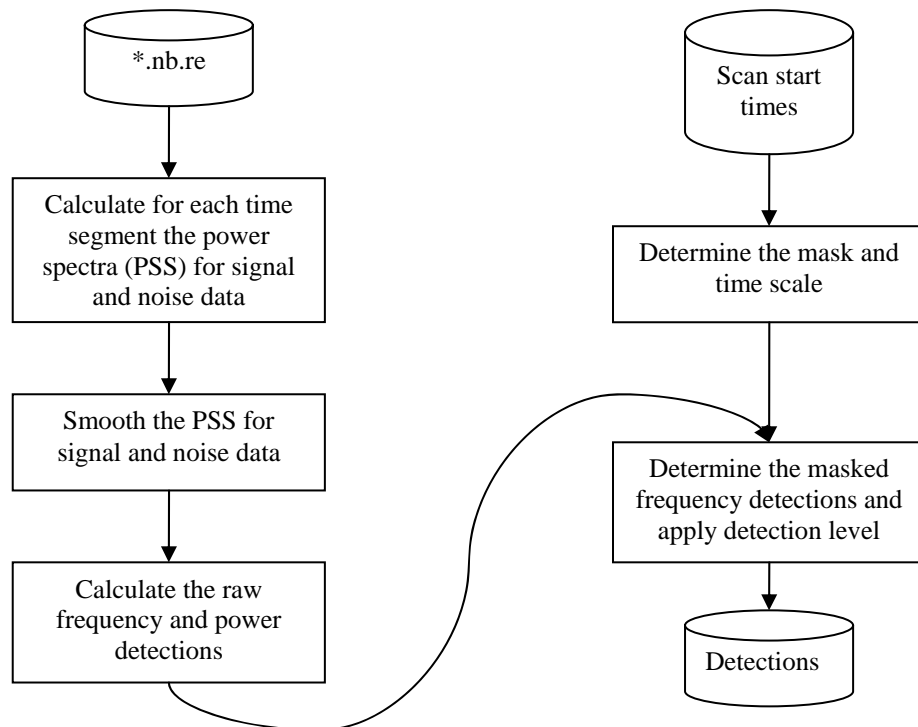


Fig. 7.5. Processing steps and data in DUNB.

For each time segment a power spectrum is calculated. These power spectra are smoothed in the next step. plots the power (contour level=50) as a function of the frequency (vertical axis) for each time segment (horizontal axis).

The Huygens observations were alternated by calibrations by pointing the radio telescope at a background calibration source. Fig. 7.6 shows this effect by concentrations of contour lines when the telescope was aimed at the Huygens probe and by a lack of contour lines when it is was aimed at the calibration source.

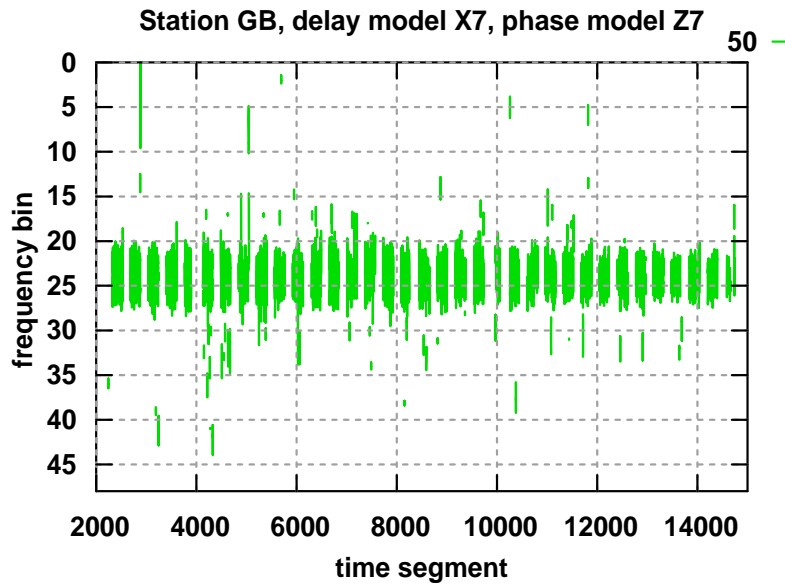


Fig. 7.6: Power as a function of time and frequency

Fig. 7.7. zooms in between time segments 3800 and 3900 clearly showing the Huygens signals around the central frequency bin 24.

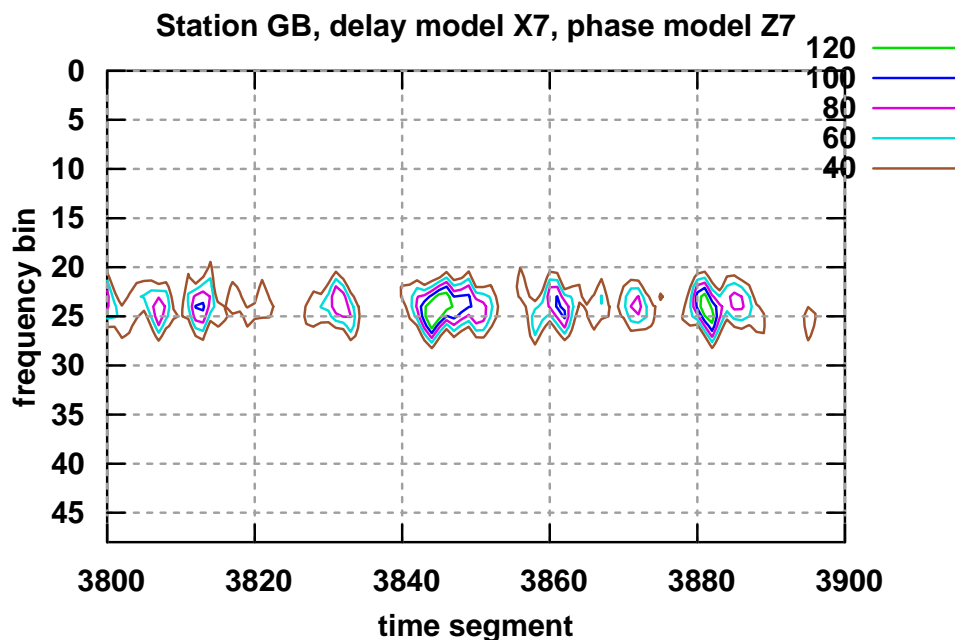


Fig. 7.7. Power as a function of time and frequency. Limited range

In the next processing step for each time segment the maximum power is determined and the corresponding residual frequency (Fig. 7.8) is calculated.

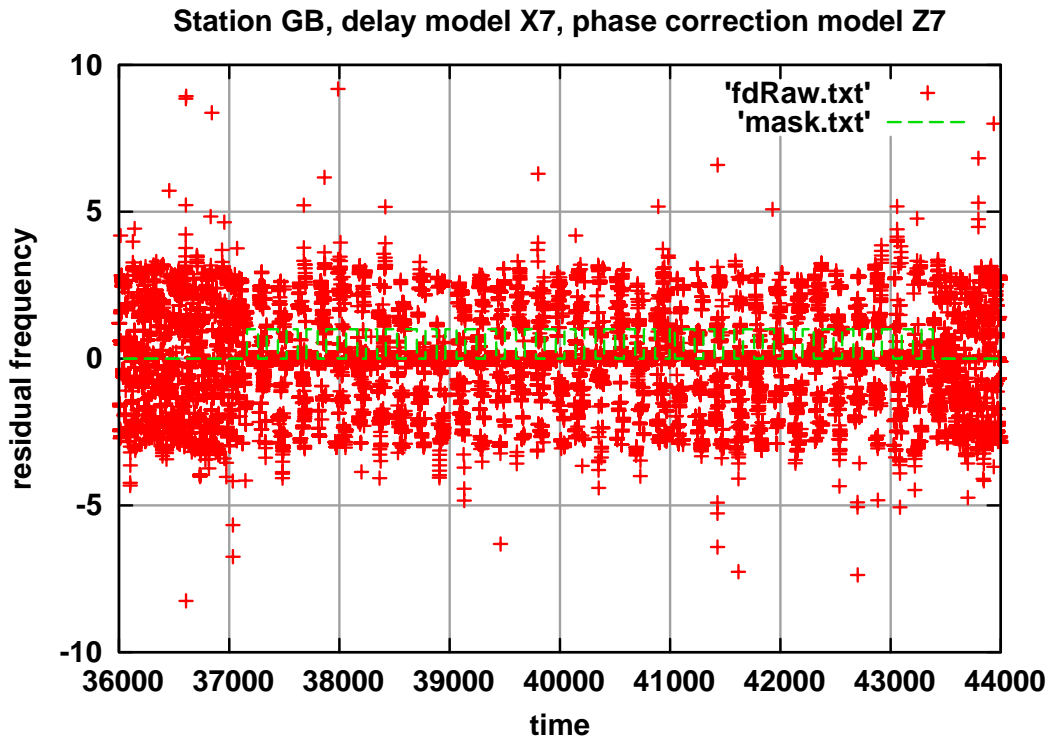


Fig. 7.8: Unmasked (raw) frequency detections.

Observations of calibration sources are thrown away by applying a mask which is based on the observation schedule in the scan start times file. Also a detection level is applied to throw away weak signals. The effect of masking is shown in Figures 7.9 and 7.10.

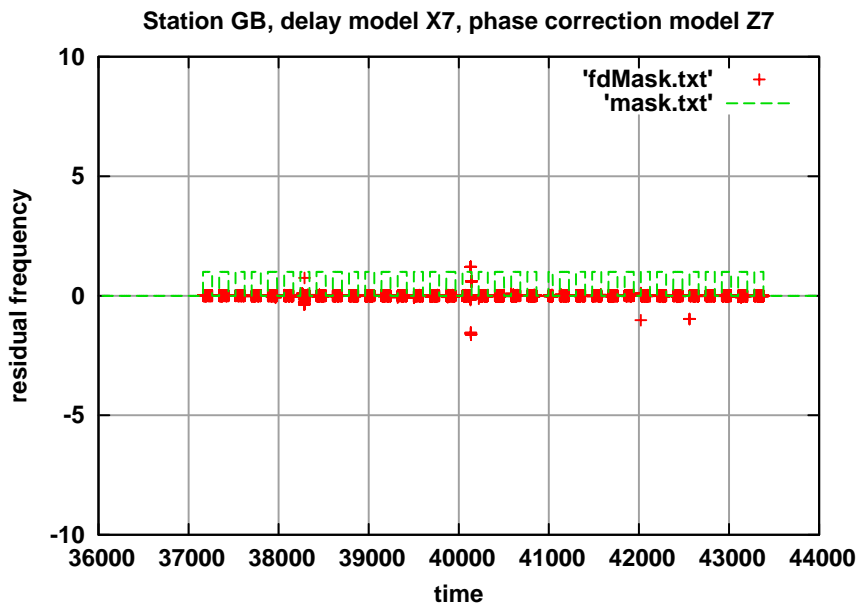


Fig. 7.9. Masked residual frequency detections

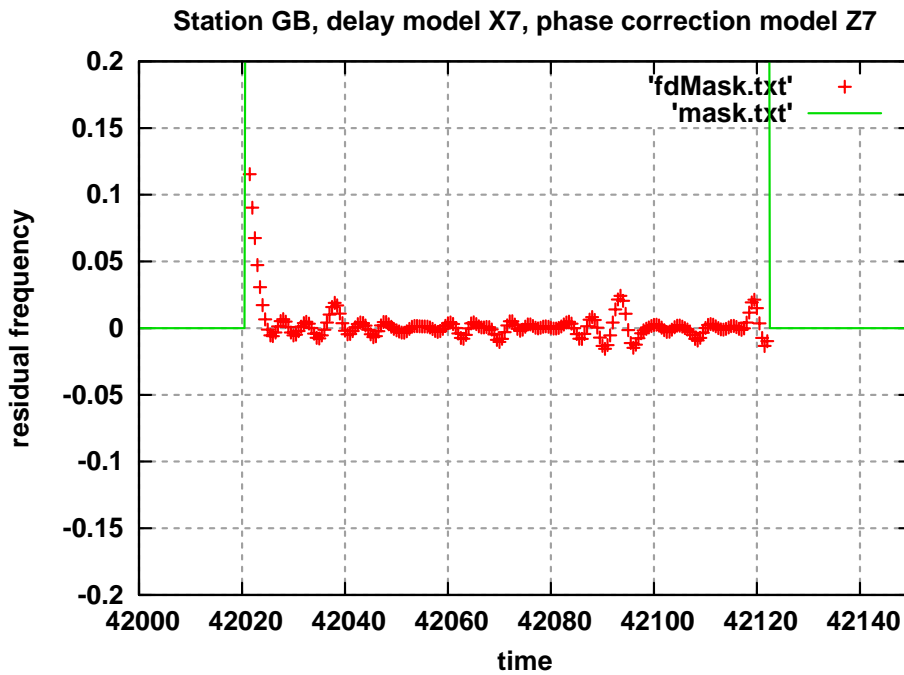


Fig. 7.10. Masked residual frequency detections. Limited time range.

The power and frequency detections are saved in a file for further processing by MPHMM.

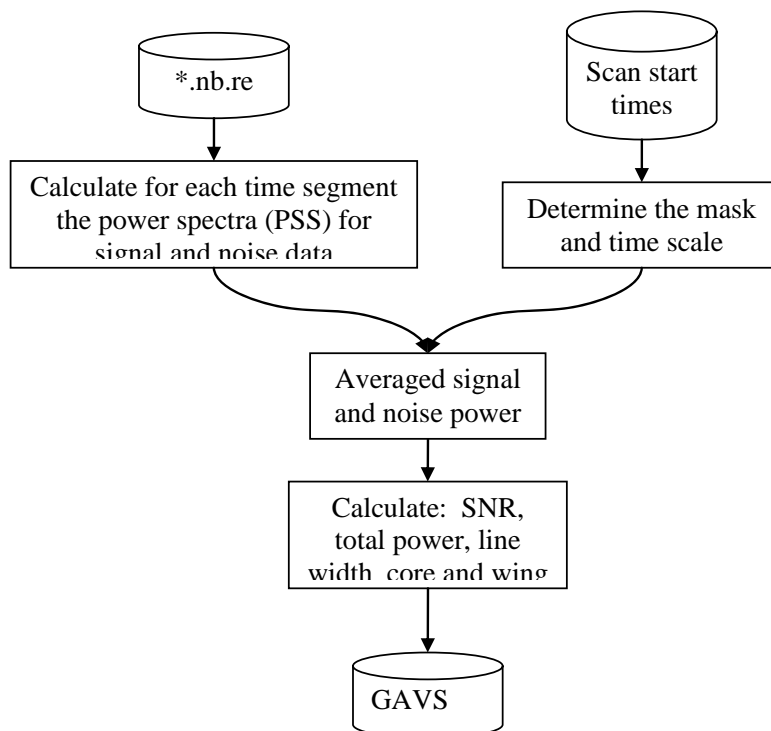


Fig. 7.11. Processing steps and data in GAVS

GAVS (Fig. 7.11) is an application based on DUNB. It is used to calculate monitoring parameters for the iteration process shown in Fig. 7.1. The SNR is the most important one and the others are total power, line width and power in a spectral core and wing.

In the first step the time domain data in the *.nb.re file is divided into time segments, but now a shorter segment length is taken compared to DUNB. For each time segment the power spectrum is calculated. The mask is applied to the power spectrum segments and then the monitoring parameters are calculated, after averaging all the segments.

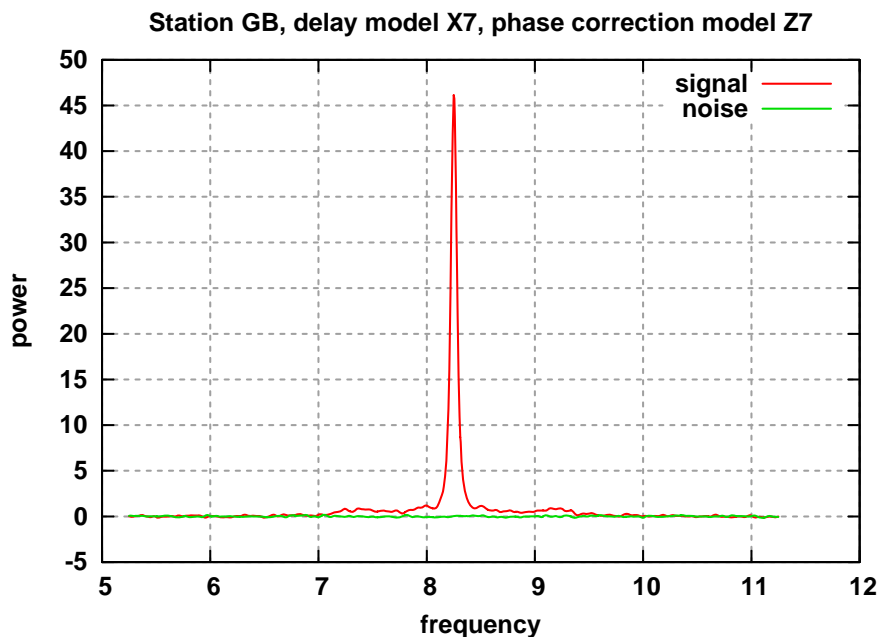


Fig. 7.12. Averaged power for signal and noise.

Fig. 7.12 shows the averaged power for all time segments as a function of the frequency for one single delay phase model combination (X7Z7). The signal and noise data from Fig. 7.12 are used to calculate global SNR, total power (TP), line width, core and wing.

SNR = max (averaged power) / stdev(averaged noise)

TP = integral of the spectral density over a specified band width

Line width = TP / max (averaged power)

Core = (power in the centre) / TP

Wing = (power left and right of the maximum) / TP

Fig. 7.13 clearly shows there is more energy in the core and less in the wings for model X9A4 compared to model X5C9. And the line width is smaller for the newest model X9A4 as expected.

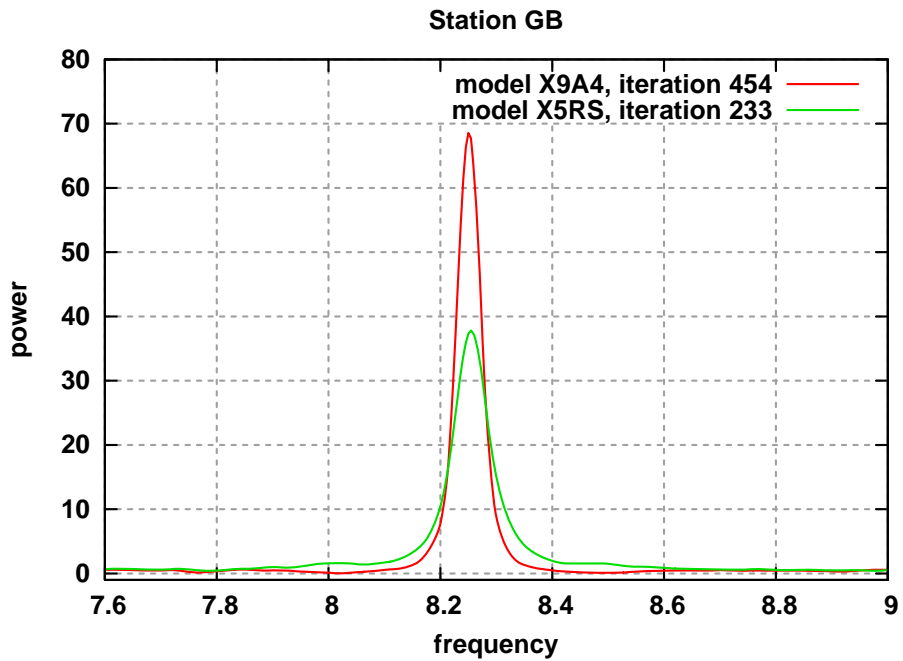


Fig. 7.13. The effect of improved phase correction on signal power

The SNR improvement is shown in Fig. 7.14 as a function of increasing iteration number. The iteration number stands for a delay phase correction model combination.

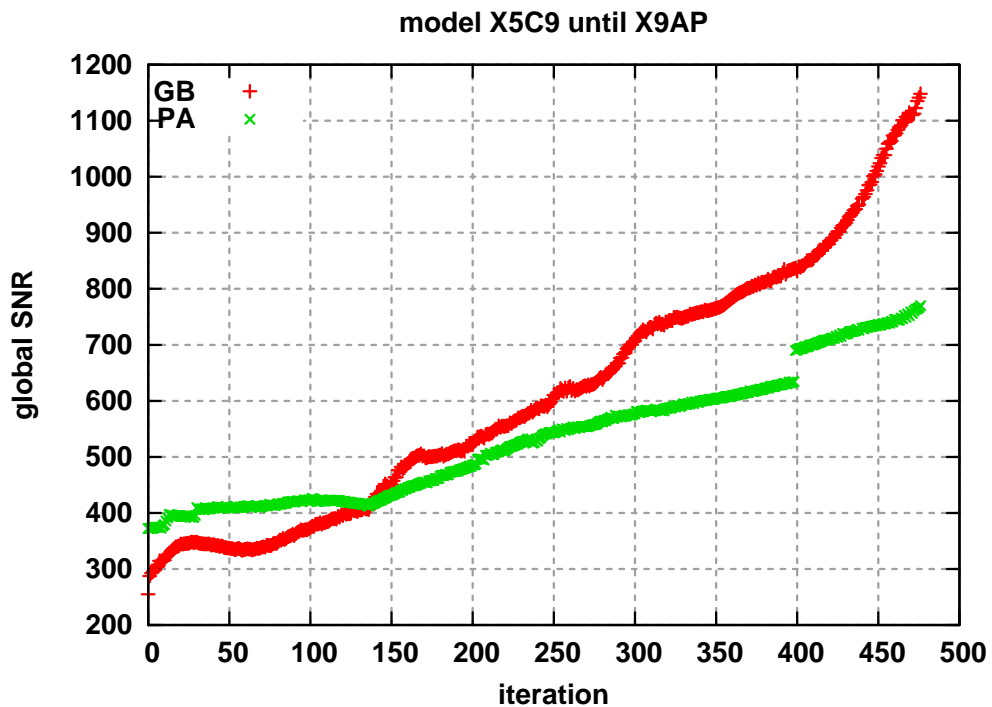


Fig. 7.14. The global SNR for the Green Bank (red) and Parkes (Green) data.

Figures 7.15 and 7.16 plot the core, wing and line widths for Green Bank and Parkes for increasing iteration number.

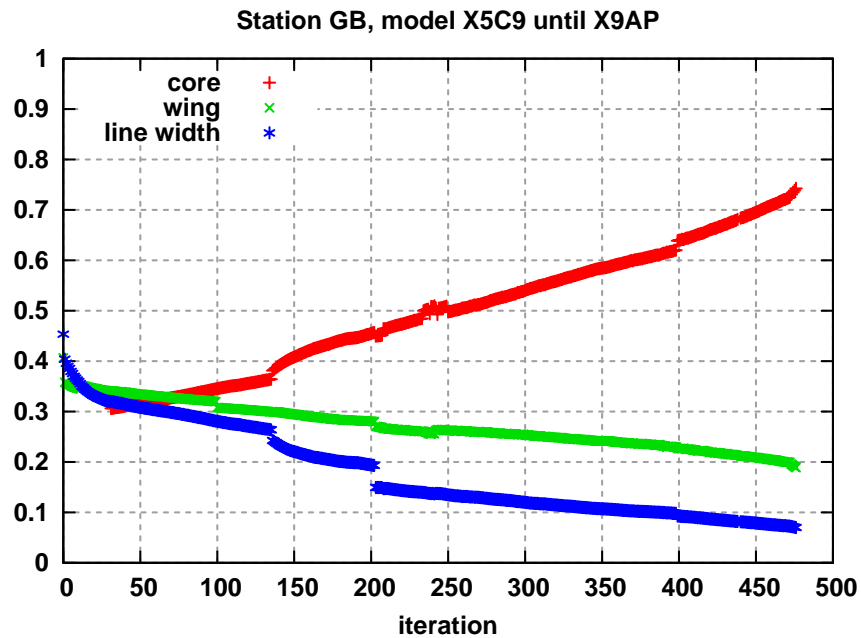


Fig. 7.15. Core, wing and line width for Green Bank

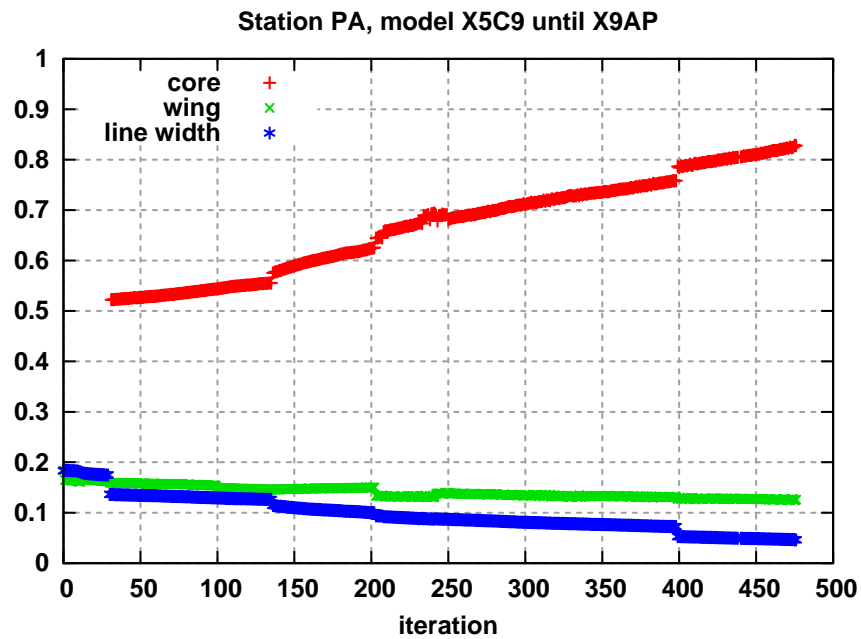


Fig. 7.16. Core, wing and line width for Parkes

The core should increase and wing and line width should decrease steadily for each new phase correction model. The steady increase or decrease is caused by the phase model changes and the jumps are caused by major model changes or tuning of detection parameters.

MPHM is short for Make Phase correction Model. Basically, what MPHM does is integrating all detected frequencies to obtain the new phase increments which are added to the previous phase correction model to obtain the new phase correction model for the next iteration loop (see Fig. 7.1). Its functional diagram is shown in Fig. 7.17.

A time frequency relation at a regular time interval is input for the calculation of the phase increments. The following steps have to be taken: concatenate GB and PA frequency detection data, set frequencies to zero in middle of non Huygens observations, merge these arrays into one time-frequency matrix, calculate the frequencies by linear interpolation into a regular time grid and multiply the frequencies with the appropriate gain corrections for GB and PA.

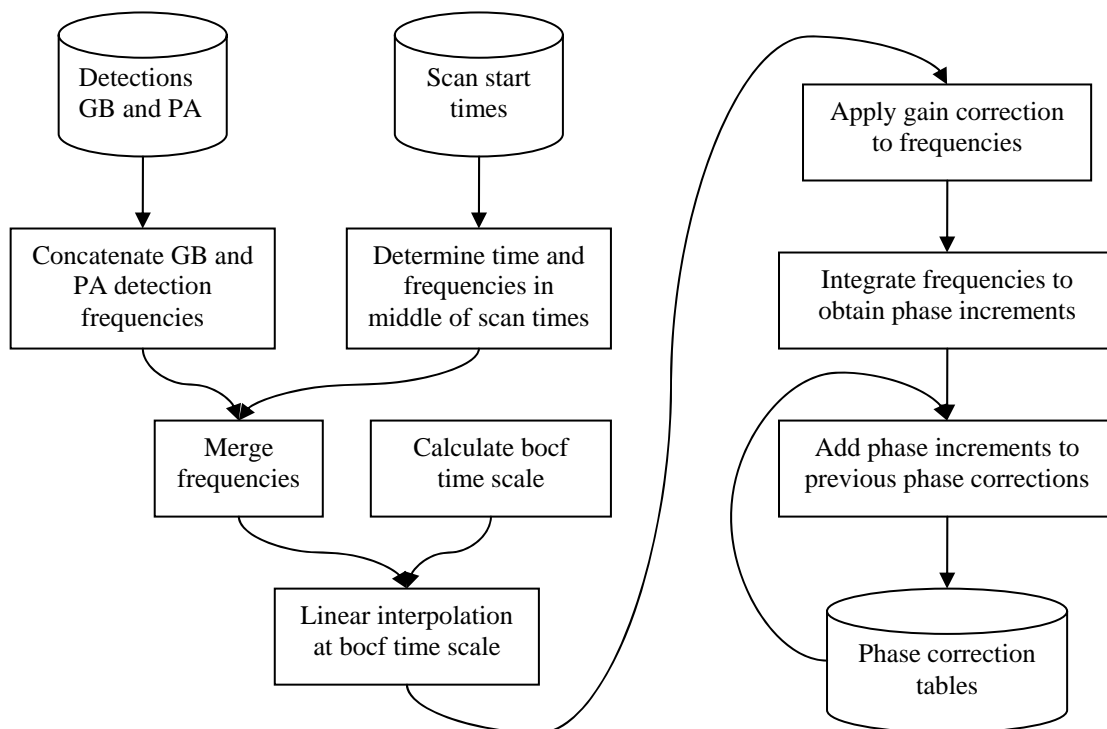


Fig. 7.17. Processing steps and data in MPHM

The more energy is concentrated in the peak of the power spectrum the better is the phase correction model: Fig. 7.18 shows a power spectrum without and with phase correction for the full frequency range, it shows a clearly higher peak (red line) for the phase corrected data.

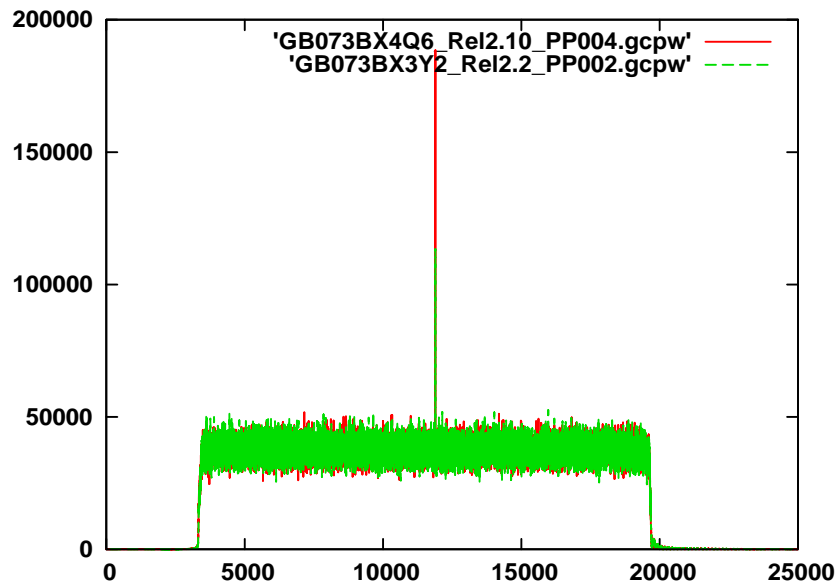


Fig. 7.18. Power spectra without (Y2, green) and with (Q6, red) phase correction.

Fig. 7.19: zooms in on the region around the signal. More energy is concentrated in the narrower peak of the power spectrum.

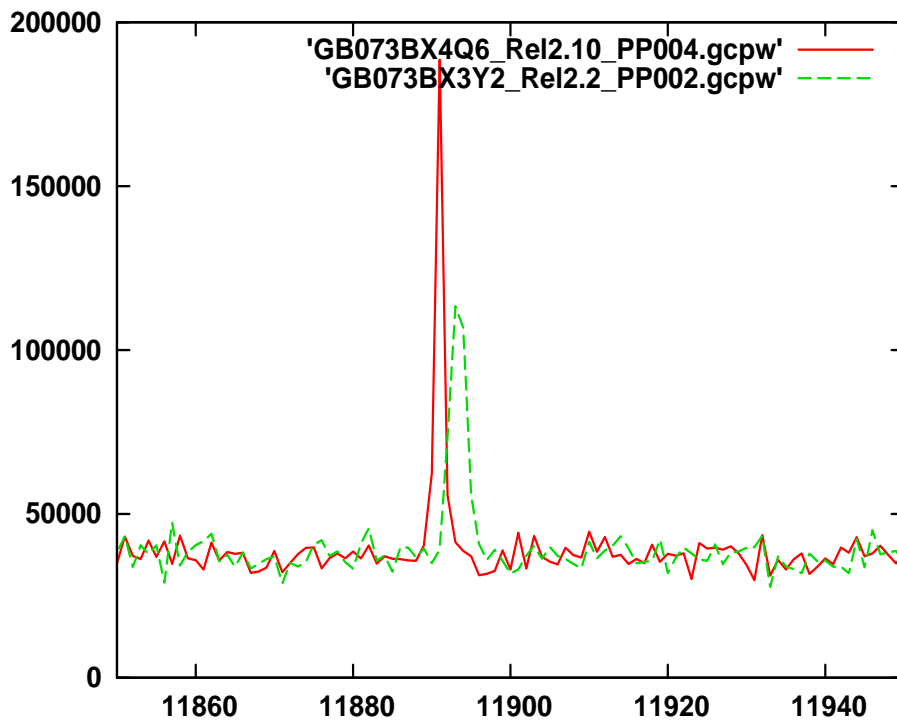


Fig. 7.19. Power spectra without (Y2, green) and with (Q6, red) phase correction.

7.3. Some software and hardware characteristics

The design specifications for the C applications were deduced from MathCAD prototype programs. This resulted in functional designs for GUNB, DUNB, GAVS and MPHM. Some algorithms were further optimized with respect to processing time and memory usage

For the production version Ansi C was chosen as the programming language. The source code comprises about 5000 lines of code and is divided over several source files, each containing functions of a certain class. To generate an executable from these source code files, several makefiles were developed. Furthermore the code is put under version control using CVS so an older version can be run again easily.

GUNB, DUNB and GAVS apply filter algorithms, which use the fast Fourier transforms. For this purpose the FFT's from the widely used, well-known free software library FFTW were used.

The results of the C applications were compared numerically with the results of their Mathcad counterparts. They were within the expected accuracy limits (32 bit or 64 bit when applicable). So production processing could be started with great confidence.

In first instance the processing was done at a stand alone PC with a 3.00 GHz Intel processor. The processing of the pre-filtered data in the *.fl files of all radio telescopes took about 5.5 hours. Processing was done during the night and the next day the new Phase Table was determined from these results. At the end of the day calculations were started with the new Phase Table as input.

So every processing cycle took about one day at the stand alone PC. In order to speed up the processing all data and software were moved to a ten node dual 64 bit Operon CPU computational and data storage cluster. Eight processes ran now simultaneously reducing the processing time to about 45 minutes. Now five to six cycles were possible in one day.

In later iteration loops only the Green Bank and Parkes data were used to determine new phase correction models. Now more than 30 iteration loops per day were possible. At the end of each week, the newest phase correction model was applied to the data of all radio telescopes, which took about 1.5 hours of processing time on the cluster.

8. Huygens VLBI data processing and preliminary results

The Huygens VLBI tracking data processing block diagram is shown on Fig. 8.1. The setup consists of two major branches: broad band processing of the phase-referencing celestial calibrator source (a quasar) and narrow band processing branch of the spacecraft signal.

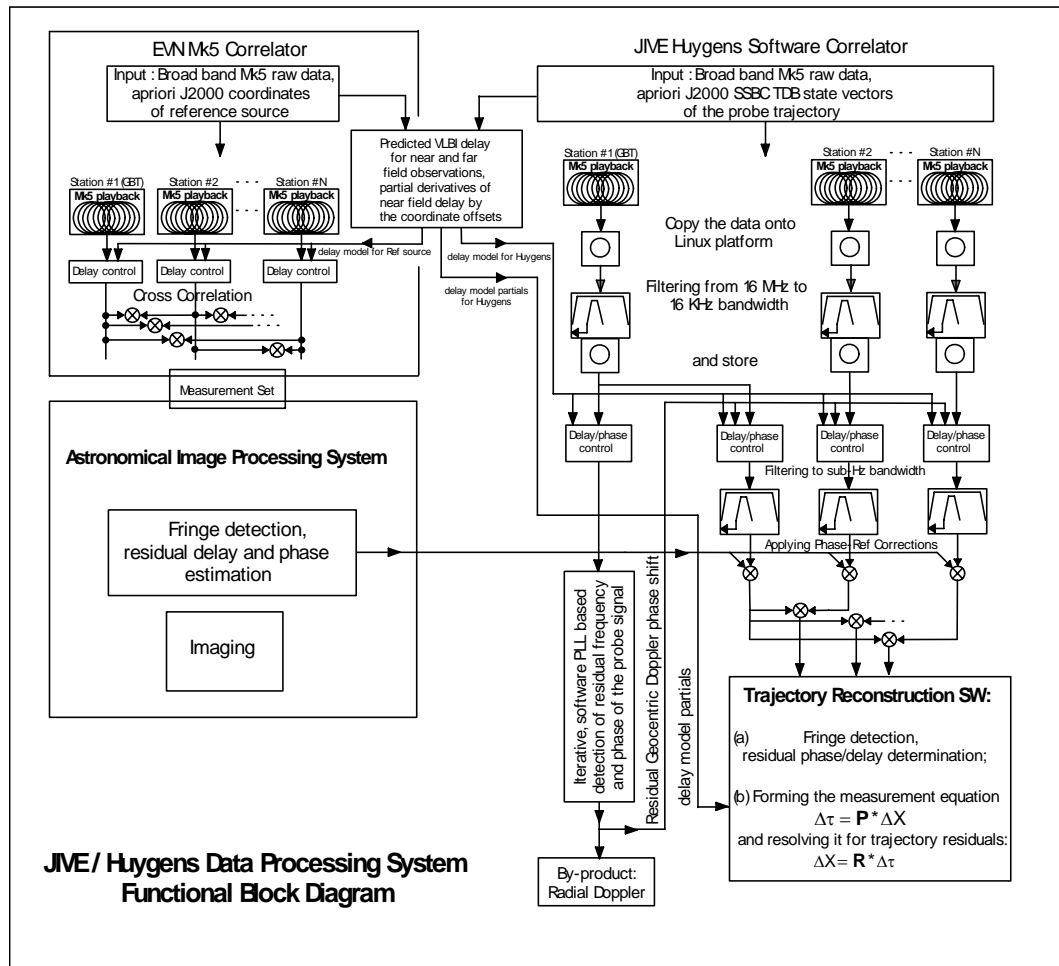


Fig. 8.1. JIVE/Huygens VLBI tracking data processing setup block diagram.

8.1. Broad-band processing of the calibrator signal

The broad band processing part is implemented on the EVN Mark4 Correlator, a specialised high-performance VLBI processor, developed by international consortium of MIT/Haystack, NASA/Goddard, EVN/JIVE and USNO in 1990's [8] and upgraded in earlier 2000s with Haystack observatory developed disk-based data recorders [9] and capable of processing VLBI data from up to 16 radio telescopes with a bandwidth of up to 256 MHz (with 2 bit coding). Fig. 8.2 illustrates the hardware setup of the correlator.

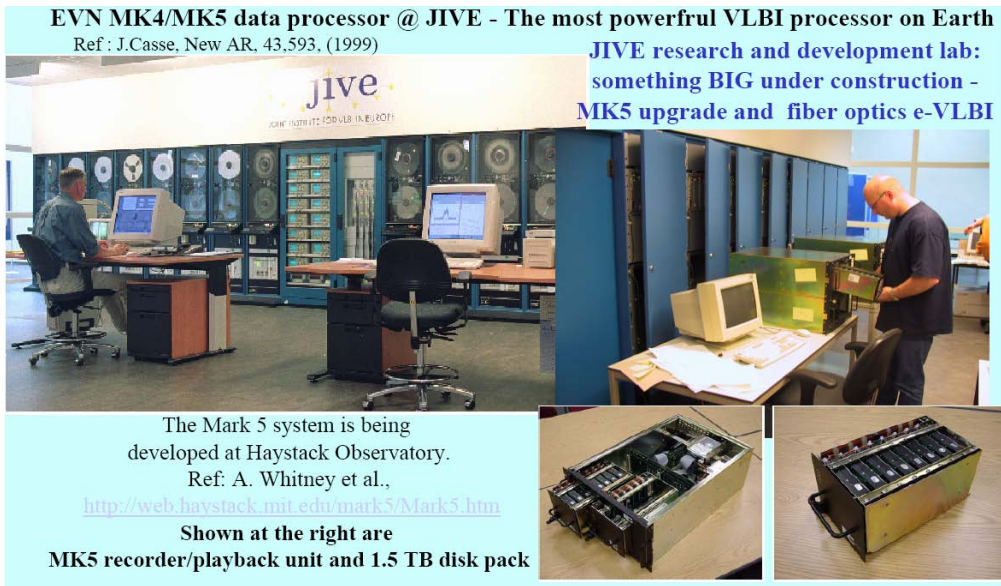


Fig. 8.2. Setup of the EVN Mark4 Correlator at JIVE, as it was during the Huygens VLBI experiment (upper panel), disk based Mark5 VLBI recorder unit and multi-TByte disk pack (lower panel).

Post-processing and analysis of the broad-band Huygens VLBI tracking data were performed using the standard AIPS (Astronomical Image Processing System) package developed by NRAO.

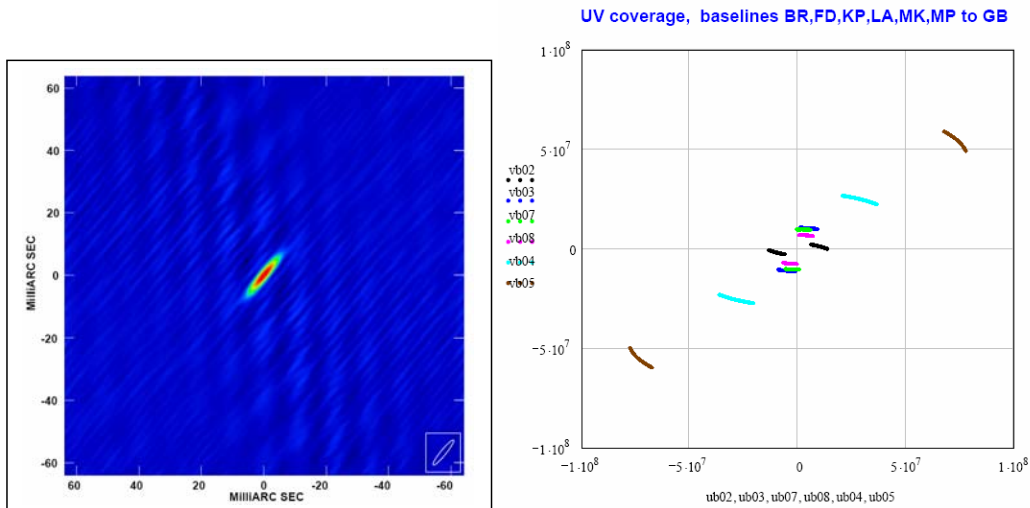


Fig. 8.3. An S-band VLBI image (left) and corresponding uv-coverage of the Huygens phase-referencing source (quasar J0744+2120) reconstructed with AIPS for a ~2-hour observation during the probe descent using GBT, FD, KP, LA, BR, MK and MP telescopes. The longest baseline, GBT-MP, was about 70 Mλ.

8.2. Calibrator data analysis

The radio image presented on Fig. 8.3 allows us to derive phases on all VLBI baselines. The reliability and accuracy of the derived phases depend on the signal-to-noise ratio achieved per solution time interval, determined by the nodding cycle (~60 seconds on referencing source, ~100 s on the Huygens probe and 2x10 s slewing time losses; the total duration of the phase-referencing cycle is 180 s). Fig. 8.4 illustrates the SNR achieved on the baseline GBT to Mauna Kea, and Table 8.1 summarizes the results for all 6 baselines which showed the reliable detections (all baselines to GBT).

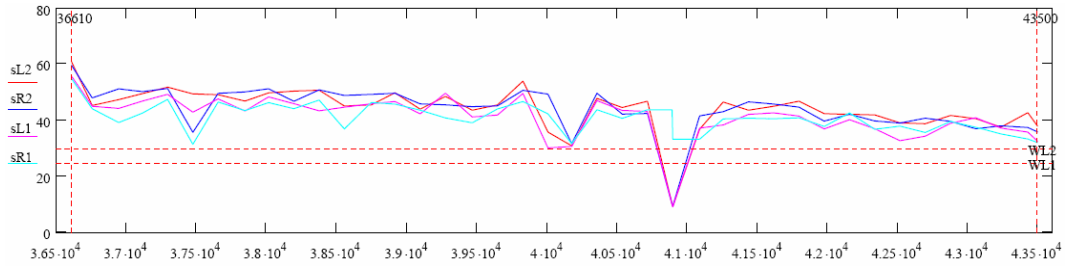


Fig. 8.4. The signal-to-noise ratio obtained for a baseline GBT-MK on the phase referencing source (~50 mJy at S-band), for a solution intervals 60 s and nodding cycle 180 s during the ~2-hour tracking interval. Horizontal axis – time, UT seconds after midnight on 2005.01.14. Vertical axis - SNR for 4 of 16 MHz sub-bands (USB and LSB at RCP and LCP around 2040 MHz). Note the decrease of SNR with time which is due to the decrease of the elevation angle of the source. Also note a drop of the SNR at 4.1×10^4 s caused by a strong wind at the GBT site.

Table 8.1. Average SNR per single 16 MHz band achieved on the J0744+2120 (50 mJy) per baseline per integration time of 60 s.

Baseline	GB-FD	GB-KP	GB-LA	GB-BR	GB-MK	GB-MP
SNR	39	40	39	45	44	35

The SNR achieved corresponds to the following single-band group delay measurement accuracy (over an interval of 60 s)

$$\sigma(\tau) = 1/(BW*SNR)=1.5 \text{ ns},$$

and a (formal) phase measurement accuracy of

$$\sigma(\varphi) = 1/SNR=0.025 \text{ radian}.$$

Practical estimates of phase accuracy can be inflated 3-4 times giving a 0.1 radian error level, which can be translated into the phase delay accuracy estimate as follows

$$\sigma(\tau\varphi) = 0.1*500\text{ps}/2\pi = 10 \text{ ps}$$

where $500 \text{ ps} = (2 \text{ GHz})^{-1}$ is a period of the signal radio wave.

Phases for each baseline between GBT and other stations (detected within 60 s intervals) were interpolated into a denser time grid. Fig. 8.5 illustrates interpolated phases for GB-MK and GB-LA baselines over the time interval from the start of the probe transmission till the end of the GBT visibility.

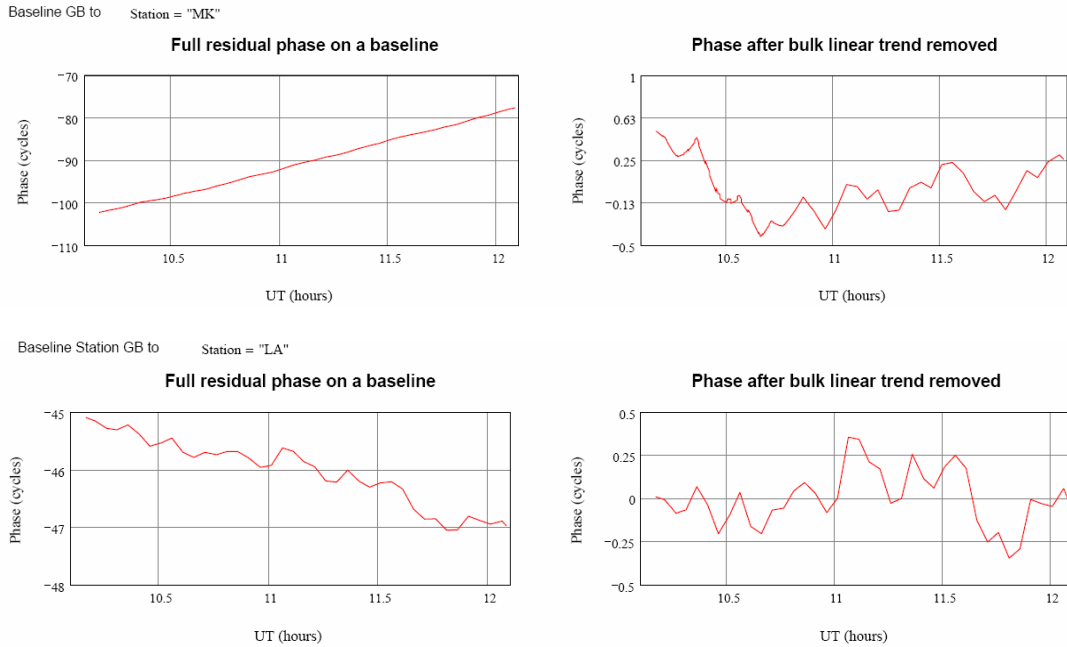


Fig. 8.5. Detected calibrator phases on two baselines, GB-MK (top) and GB-LA (bottom). Note the overall linear trend of phases by many 2π cycles over the 2-hour interval and the random walk excursions at the level of a fraction of a cycle on a time scale of minutes.

Although the observations were made using 8 sub-bands (4 tuned to the Channel A frequency and 4 – to the Channel B frequency) only 2 sub-bands at LCP Channel A were actually available for phase referencing, since observations were performed with Phase Calibration signal switched off not to interfere with on-line RSR detection. That made impossible to align the phases at different polarizations for different base-band converters. Only LCP UCB and LSB centred around 2040 MHz were phase-aligned (as they were from the same base-band converter) and used for group delay analysis. Phase Calibration signal generates monochromatic tones with predictable phase and with 1 MHz spacing over the whole observing band, which makes it possible to align phases of different base-band converters and improve the signal-to-noise ratio for broad-band detection. But at the same time it can also damage the narrow band signal of the probe.

It is still an opened question how to use Phase Calibration signal for phase-referencing spacecraft tracking and what the optimal observational strategy, hardware setup and software processing algorithms should be developed to allow both reliable detection of the weak narrow band signals from spacecraft and phase alignment for broad band detection of background celestial reference sources.

Another important issue is a multi-band group delay, which enables calibration of phase delays with accuracy good enough to resolve the so-called 2π ambiguity. However, the multi-band group delay cannot be used in our case.

Fig. 8.6 shows the time behaviour of the calibrator group delay (black line) computed as the average for two adjacent bands, LSB and USB for LCP with 60 s coherent integration time (ON reference source part of the phase-referencing nodding cycle) and phase delay (blue line) derived from the detected phase for the GB-MK baseline. Note that while the group delay and phase delay are independent measurables, and should give the same phase solution, the accuracy of these solutions for a given SNR are very different: the rms error of group delay $\sigma(\tau_g) = 1/(\Delta F \times \text{SNR})$ (where ΔF is the bandwidth of the sub-band, 16 MHz in our case), but rms error of phase delay $\sigma(\tau_p) = 1/(f_o \times \text{SNR})$ (where f_o is the observational frequency, 2040 MHz in our case). That's why the scatter of the group delay and phase delay is so different. The group delay (although not that accurate) is a "true delay" while the phase delay is derived from the measured phase and may be subject of a 2π ambiguity. Since phases are 2π uncertain, the phase delay might have a bias of several cycles of ~ 500 ps at our observational frequency.

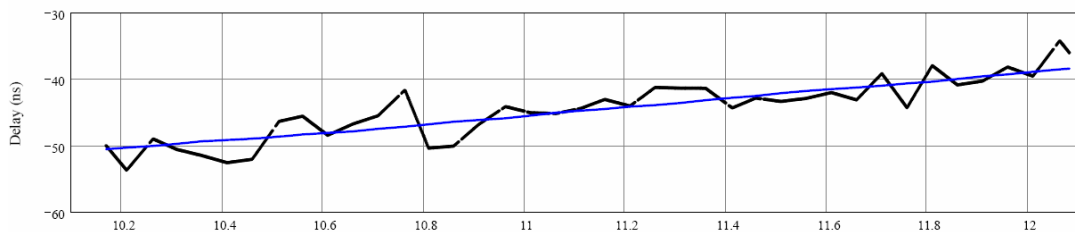


Fig. 8.6. Group delay (black line) and phase delay (blue line) for GBT time span, baseline GB-MK. Horizontal axis – time (hours).

To check the phase delay versus group delay consistency, we computed the uncertainty of the fit of the phase delay to group delay. In the case of the GB-MK baseline, this uncertainty is 290 ps, while for other baselines it ranges from 230 ps and 500 ps, not good enough to resolve the 2π or 500 ps ambiguity. Table 8.2 summarizes this uncertainty $\bar{\delta}(\tau_g - \tau_p)$ for our baselines.

Table 8.2. Phase delay to group delay origin uncertainty for different baselines.

Baseline	GB-FD	GB-KP	GB-LA	GB-BR	GB-MK	GB-MP
$\bar{\delta}(\tau_g - \tau_p)$, ps	440	230	480	330	290	500

The second check on phase delay versus group delay consistency was performed by comparing phases and delays for two adjacent bands of the same base-band converter.

Fig. 8.7 illustrates the principle of group delay calibration in our case of two adjacent bands (LSB and USB, 16 MHz wide each). The essential point here is that both sub-bands are down-converted from IF to video band using the same local oscillator, so the signals should not have a systematic phase bias between these two sub-bands.

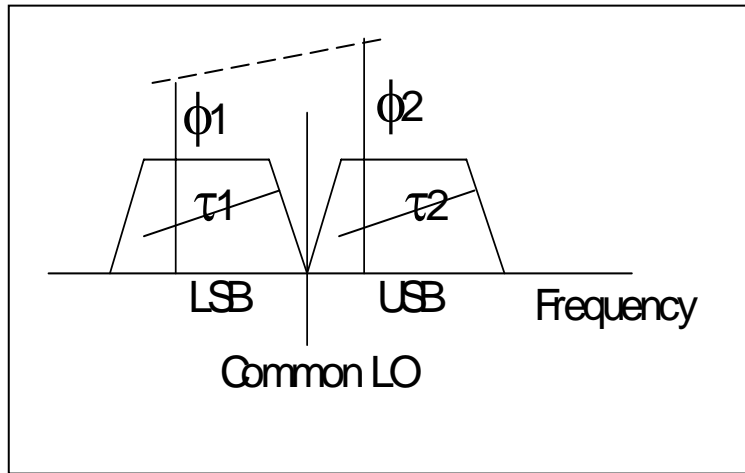


Fig. 8.7. Illustration of group delay calibration and 2π ambiguity check.

Single band group delays τ_1 and τ_2 are measured independently, as well as mean phases ϕ_1 and ϕ_2 for each sub-band. Using the relation $\tau = d\phi/df$, we can conclude that the measured phases and group delay should obey the following relation:

$$(\phi_2 + n2\pi - \phi_1 - m2\pi)/DF = \tau_g$$

where n and m are the arbitrary integer numbers which can be ideally calibrated out if our phase delay to group delay uncertainty is significantly (say, 3-4 times) less than 500 ps. That could be achieved in our case even with a 50 mJy calibrator source if by using Phase Calibration signal to align different base-band converters and properly distribute the observational bands not setting four “redundant” bands too far away in frequency (to attempt to detect the Channel B signal). These measures could improve the group delay accuracy by factor 3-4 to a ~ 100 ps level.

When this two-band check is applied to our data it clearly shows that some baselines can be 2π ambiguous. As shown in Fig. 8.8, the baseline GB-MK has a 62.9 ns phase delay shift between two sub-bands, while the baseline GB-LA has a 1.2 ns, considering that a 2π shift in phases corresponds to a 62.5 ns delay shift over the band separation of 16 MHz. It indicates that we are close to resolving the 2π ambiguity.

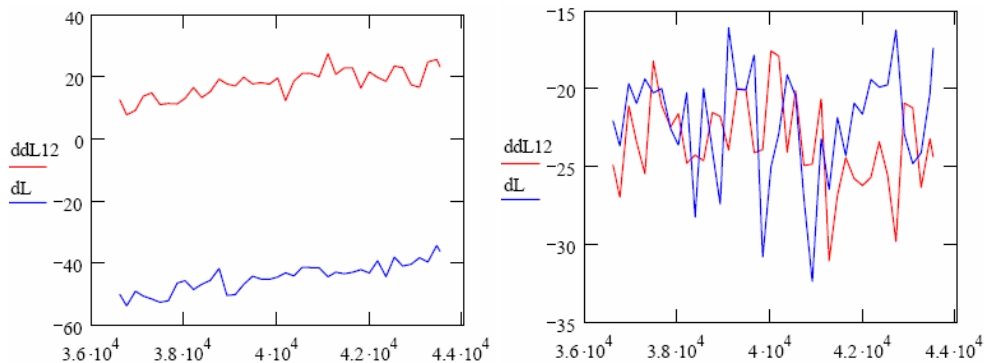


Fig. 8.8. A comparison of the two-band phase delay/group delay mismatch for different baselines. GB-MK (left) shows a 62.5 ns shift between the two base-bands, while GB-LA (right) shows a perfect match.

8.3. Narrow band processing of the Huygens Probe signal

Narrow band processing of the Probe's signal was conducted on the general purpose Linux cluster (shown in Fig. 8.9), using software developed specially for this experiment.



Fig. 8.9. Linux cluster used for narrow band Huygens VLBI processing. It consists of 6 dual core Opteron nodes equipped with 1.5 TB disk raids each interconnected via a FireWire switch and connected to Mark 5 VLBI recorders via optical 1GB Ethernet lines.

The first step for narrow band processing was to move the data from the recorded media (Mark 5 disk packs for VLBA data and ATNF disk raids for data obtained with the Australian telescopes) into the general purpose Linux computers. For Mark 5 data the built-in Mark 5 software functions were used. Software to deal with ATNF data (move and re-format it) was developed at the Metsähovi Radio Observatory, (HUT, Finland). The rest of the processing software was developed at JIVE.

Development of this software started less than a year before the Huygens experiment and its first version it was ready just 2 months prior to the observations of 14 January 2005. The software was exercised and tested with the GG057 A and B test observations of the Cassini spacecraft and Mars Express orbiter. These were technological tests to check a highly non-standard VLBI observational and data processing pipeline.

8.4. Single dish detection of the probe's signal

As shown in Fig. 8.1, narrow band processing is split into two major branches:

- Single dish detection branch, dealing with signals from large antennas, GBT and Parkes;
- Array processing branch, dealing with both large and smaller antennas.

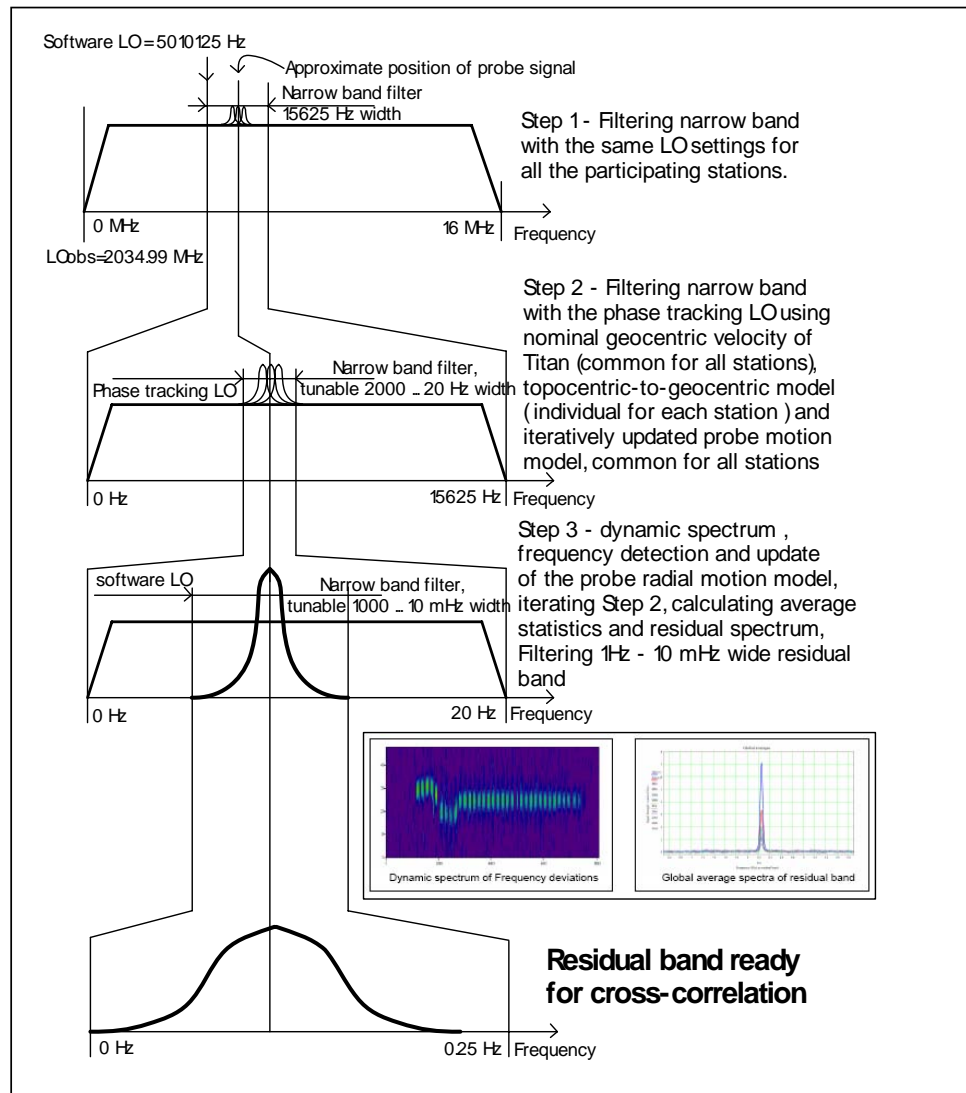


Fig. 8.10. Single dish data processing pipeline.

This split is dictated by the nature and characteristics of the Huygens signal – essentially, a single harmonic with its spectrum “smeared” primarily due to the limited stability of the on-board ultra-stable oscillator (TUSO) and signal propagation effects. In order to calibrate the observation, one needs to get phases of cross-correlated signals from a continuum background source in close vicinity to Huygens on the celestial plane. A relative weakness of such the source (about 50 mJy at 2 GHz in our case of the only available calibrator in the Huygens Field, the quasar J0744+2120) necessitates use of as a wide detection band (and therefore data rate) as possible. Thus, the maximum available data rate at all participating stations (varying from 128 to 512 Mbps) was used in the Huygens VLBI tracking experiment. However, cross-correlating the narrow-band Huygens signal “embedded” in the wide-band data stream would be prohibitively demanding in terms of computational power. Thus, removal of the Doppler shift from the data before cross-correlation makes it possible to narrow the spectral window of data processing thus decreasing the

demand on computational resources. As a natural by-product, this stage produces the estimate radial Doppler shift of the signal and provide this data for independent analysis (e.g. as an additional set of data for DWE).

At a given power level of $5 \cdot 10^{-26}$ W/m² of the probe's carrier line signal at Earth, only the largest antennas (100m GBT and 64m Parkes telescopes) were capable to independently detect it with a reliable SNR at 3-5 level within 1-3 seconds integration time, while smaller 25-20 m class antennas would have an SNR of more than an order of magnitude less, and the probe motion and internal fluctuations of local oscillator would not allow more than an order of magnitude longer independent integration time for small dishes. Fig. 8.10 illustrates the single dish data processing pipeline.

After the Mark5 and ATNF recorded data was moved from recording media into Linux cluster and re-formatted in such way that a single observed sub-band was represented as a separate file, the actual signal processing started.

As it is shown in Fig. 8.10, the first operation was to extract 16 kHz wide band containing the probe's signal from 16 MHz recorded band. This was done using the digital FFT-based down-converter and Low-pass filter. The bandwidth of 16 kHz was selected to cover the Titan-to Earth and probe's proper Doppler range for all the stations during the full duration of the mission. Local oscillator of this software down-converter was set to the same value and zero initial phase for all the stations, so making the 16 kHz data band to look like it was independently observed, but phase coherent with the broad band data.

The next step in the pipeline is the signal delay/phase correction from the topocentric time/coordinate frame to geocentric frame, common to all the stations. For this correction we used the a-priory SSBC state vector of the Entry Point of the DTWG descent trajectory, and predicted delays for each station were computed using near-field enabled VTD software package (L. Petrov, NASA/GSFC), the same package which was used to compute the far field theoretical delay for calibrator source, using the same Earth model, station positions, tropospheric delay model, General Relativity corrections and Solar system ephemeris (DE 405). Far field delay prediction accuracy of VTD package was verified on available IVS geodetic/Astrometric observations and was proven to be accurate to sub-ps level.

Worth to mention that delay computation was made using improved reference source coordinates, obtained in 2005 using IVS geodetic observations and improved Australian station coordinates obtained in 2006 using VT08 geodetic observation run.

Fig. 8.11 illustrates the system geometry used to compute near field delays for probe's signal and far field delays for reference source.

Explanation of terms for Fig 8.11.

All vectors are in J2000.0 coordinate frame.

GC – center of Earth;

Vg – Earth center velocity in SSBC;

Xs1 and **Xs2** – geocentric coordinates of telescopes' phase centers;

Vs1 and **Vs2** – geocentric velocities of telescopes' phase centers (not shown);

Pref – pointing vector to the phase referencing radio source;

Mn – nominal motion model of the target (ephemerid), which can be presented as spherical or Cartesian vector in different frames: (a) pure geometrical state vector, (b) light time corrected astrometric position, or (c) light time and stellar aberration corrected geocentric vector;

Pt – geocentric astrometric pointing vector of nominal motion model, it is derived from light time only corrected motion model **Mn**;

Ps1 and **Ps2** – local, station based pointing vectors accounting for near field effects; these vectors corresponds to light time and stellar aberration corrected motion model **Mn**.

And ,finally, **Ma** is the actual motion model to be determined.

Of course, this diagram does not show explicitly the relativistic bending of light propagation geodesics. When near field delay was computed for each station, partial derivatives of it with respect to the probe's coordinate offset were computed also for the purpose of trajectory reconstruction.

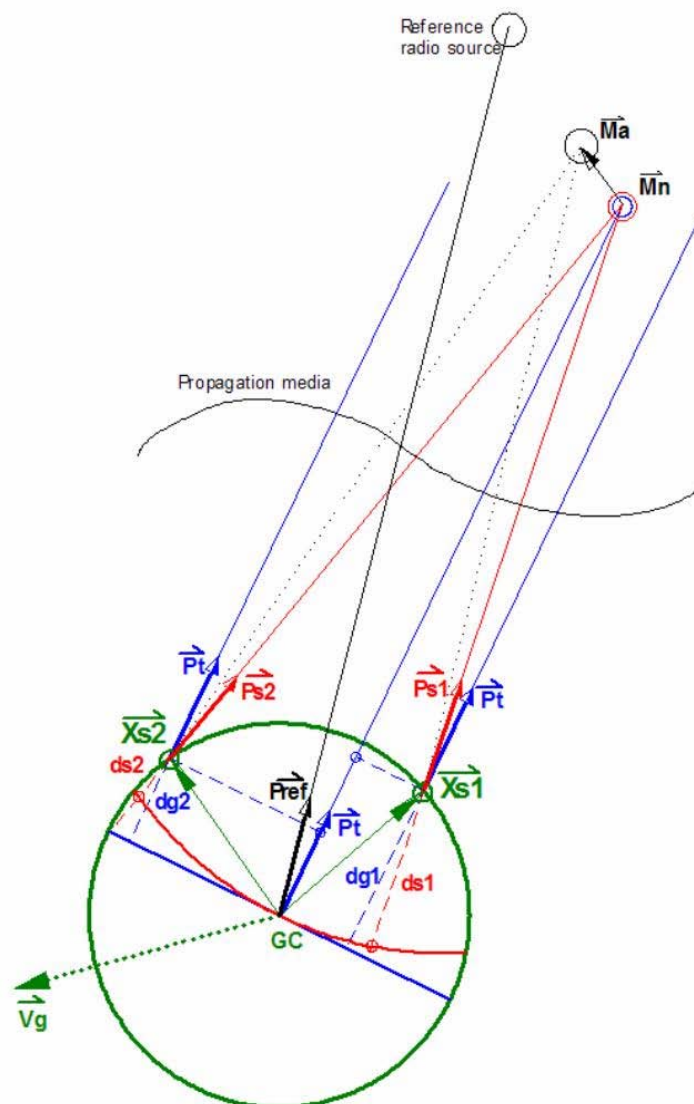


Fig. 8.11. Illustration of the system geometry used to compute near field and far field delays.

After applying the near field delay model derived from a-priori probe's state vector to the signals in 16 kHz band we obtained the signals as they would be seen (in a flat space-time) by stations located on the sphere with a radius starting from the a-priori probe's position at the moment of emission and ending at the geocenter at the moment of detection. Analytically this transform can be expressed the following formula:

$$S_{gc}(t_{gc}) = S_{topo}(t_{topo} - \tau_{gctopo}),$$

Where S_{gc} and S_{topo} are analytical signals (after Hilbert transform) at sky frequency, t_{gc} and t_{topo} – time labels per data sample in geocentric and topocentric (related to thy station) time frames and τ_{gctopo} is a time delay of the signal propagation between these to frames.

Effectively it was done using Fourier interpolation, when the time shift of an integer number of samples was done by simple address shift of the data block in a file, while fractional sample delay was performed by corresponding phase rotation of the signal's spectral components in spectral domain.

8.5. Single dish detections

For a search of the signal in “geocentric” band we applied an iterative software phase lock loop (PLL) technique: first we detected frequency of the signal within a time interval long enough to give a reliable detection but short enough to not allow the signal be smeared by residual Doppler variation. For different parts of the descent/landing trajectory and for different telescopes and for different iterations of the signal search this time interval varied in a range from 10 to 1 second.

At each iteration detected frequency was integrated to phase with zero integration constant, and a fraction of the detected phase was applied to the signal at the next iteration. Phase removal gain (fraction of the detected phase to be removed from the signal), detection interval and detection threshold were varying from iteration to iteration with a manual control for the process convergence with respect to criteria of improving the SNR and narrowing the residual spectrum.

After several hundred of iterations the Doppler frequency and phase (as the integral of the frequency with zero integration constant) were obtained. We stopped the iterations when the global average residual spectra for both GBT and Parkes showed ~30 mHz width at 60 seconds (Cosine) spectral window. 30 mHz boundary for PLL processing was set in accordance with estimated difference by the probe's Doppler shift as seen by different stations to be of the order of several mHz for possible probe's displacement ~100 km with respect to a-priori state vector.

Fig. 8.12 illustrates the detected frequency curve and corresponding SNR of detections for combined GBT and Parkes data sets with linear interpolation over the gaps of the Titan-Reference nodding cycle. This last iteration PLL time constants (for Gaussian window), which define the time resolution of the Doppler detection were set to 1s for GBT and 3 s for Parkes data. The longer time constant for Parkes case was due to 4 time smaller collecting area and so the signal strength. This choice of time constants made the final SNR for both GBT and Parkes about equal, as it can be seen on Fig.8.12, SNR (blue line) for Parkes is about 30% less than that for GBT.

It should be mentioned that subtracting the same phase from signals of different stations (with whatever integration constant it was obtained from frequency

detections) cannot affect the cross-correlation phase, since cross-correlation of narrow band signals is just a multiplication of one signal by a complex conjugate of another one, so the common phase subtracted from both simply drops out from the solution.

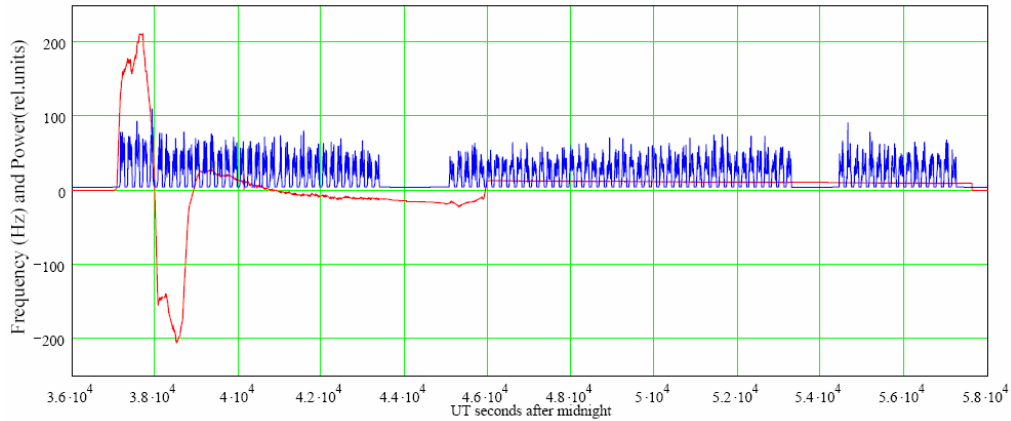


Fig.8.12. Detected Doppler shift frequency (red line) and SNR of detections (blue line) for GBT and Parkes combined data set. No time overlapping between GBT and Parkes data. Gaps are linearly interpolated. Gaussian window detection time is 1 s for GBT and 3s for Parkes data.

Global (over the whole time range available for each telescope) average residual spectra for all the stations, obtained after the detected phase was removed are shown in Fig. 8.13. Although 12 stations (as plotted) had showed a clear detection of the probe's signal, only 7 finally were found to be suitable for phase-referenced calibration.

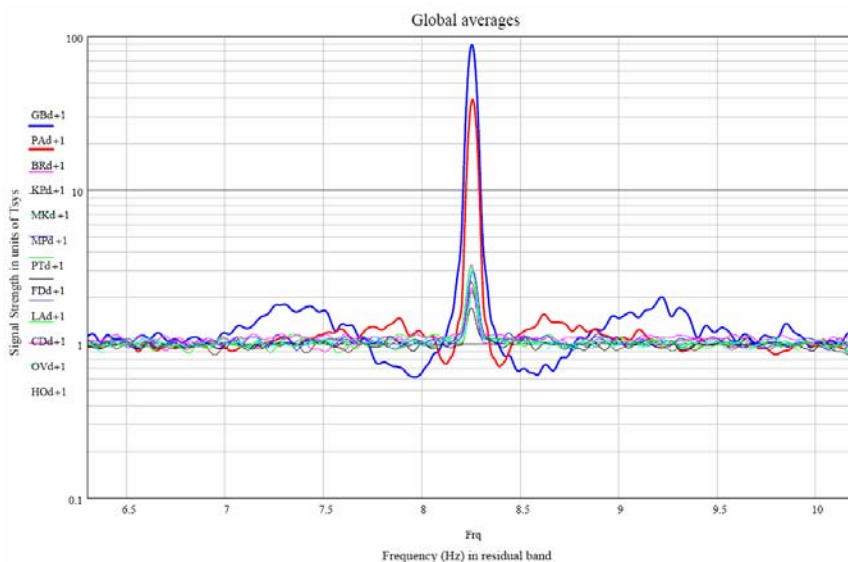


Fig. 8.13. Global (over whole available time range) averaged spectra for 12 stations after subtracting GBT/Parkes detection phase curve. The stations are GB, PA, BR, KP, MK, PT, FD, LA, CD, OV and HO.

Second checks on data consistency were done using so-called “ultimate resolution” residual spectra, e.g. single Fourier transform over the whole time span available. For a time span of about 2 hours in GBT case it corresponds to ~150 microHz resolution. Fig. 8.14 shows these spectra for GB and BR stations. Note that spectral power is concentrated within central 30 mHz of frequency span.

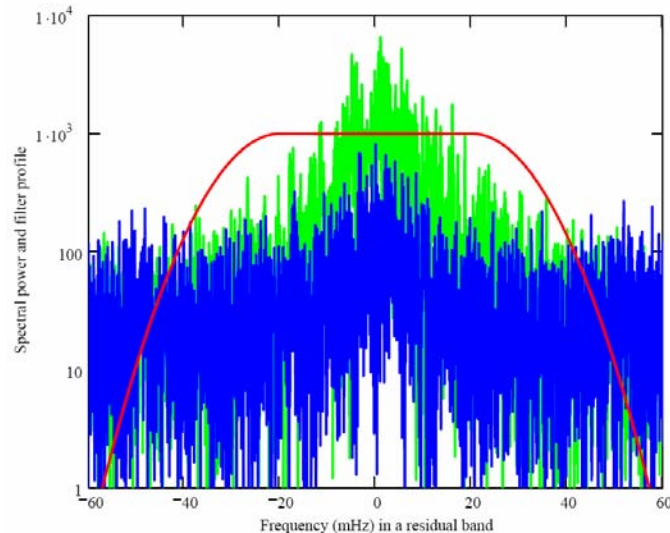


Fig. 8.14. 150 μ Hz resolution spectra of GBT (green line) and Brewster (blue line) observed signals after a “common phase” subtraction. Red line represents 75 mHz wide frequency range to filter before cross-correlation

The third check on data consistency was done using a “period folding” technique. As it can be seen in Fig. 8.12, the power level of GBT and Parkes detections follows the 180 nodding cycle with 100 s ON-Huygens, 60 s ON-Ref (OFF-Huygens) and 2x10 s slew between pointings. When power counts in the residual band for these large antennas are folded with 180 s period they clearly outline the nodding cycle, as it is shown on a top panel of Fig. 8.15. When the same folding is applied to the power counts in residual band (70 mHz wide) for small antennas after they were corrected for a-priory Doppler and GBT/Parkes detected Doppler, the nodding cycle appears as well (Fig. 8.15, bottom panel). It’s a significant confirmation of the consistency of the phase detection, correction and adaptive filtering. Since no phase correction can change the power level of the noise-like signal it means that quasi-monochromatic signal is present in the small antenna data and it is phase consistent with large antenna detections.

Worth to mention that power level of the Huygens probe carrier signal at Earth was at the level of ~0.1 radio photons per second per square meter, or 20-25 photons per second per collecting area of 25 m dish.

After these check we decided that residual, geocentric interpolated and Doppler corrected signals are ready for ultra narrow band filtering with 100-10 mHz wide filter and subsequent cross-correlation and phase referencing. But before doing that we made another closer look at the single dish detections.

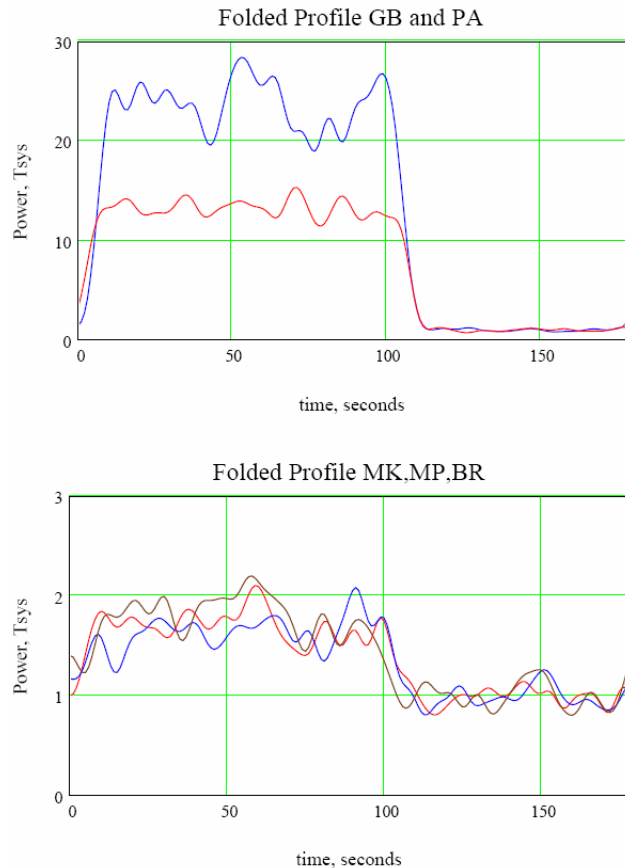


Fig. 8.15. Folded profiles of power level (independently) detected with large antennas – top panel and small antennas (after phase corrected for geocentric Doppler phase) – bottom panel.

8.6. Closer look into the single dish detections data

The Huygens VLBI tracking experiment was unique in many respects such as signal power level at which detections were made, distance to the probe, uncertainties in flight dynamics during it's descent through the Titan's atmosphere, surprisingly long time of the probe's transmission time from the Titan's surface, signal propagation through a dense and turbulent atmosphere of Titan, all that combined was not initially put into the project definition and certainly will require a closer look from many different perspectives. Many questions can be asked about the performance of our detection algorithms, since they were developed on the live run of the experiment and did not foreseen by the project plans and verified by a multitude of test on similar experiments.

The data quality check can be done on using this unique data itself. Parkes telescope was lucky to detect the probe's signal at both parachuting and landed phases of the mission and gives the unique opportunity to compare the signal behavior during these distinctively different phases.

Fig. 8.16 shows an overlay of frequency detections for several scans (100s long with 80s gaps between them due to nodding), with 3 s (Gaussian) sampling window and long term trend removed, obtained during parachuting phase of the mission (red line) and landed phase (blue line).

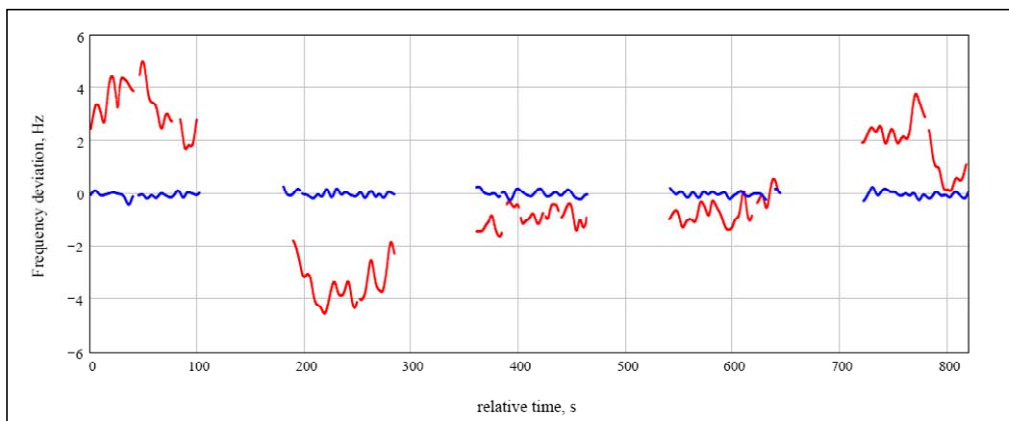


Fig 8.16. An overlay of several scans of frequency detections (Parkes) for parachuting phase of the mission (red line) and landed phase (blue line). A difference of the frequency behaviour is evident.

RMS of frequency deviations during the landed phase is 150 mHz, or 2.5 cm/s in velocity terms and a near-Gaussian distribution (see the histogram in Fig. 8.17), while the red line – frequency deviations during the parachuting phase, shows 2-3 Hz (or ~0.5 m/s) excursions on time scale ~10-20s, definitely due to short time scale (close to the eigenperiod of probe's penduling) flight dynamics effects and can provide an information on small scale turbulence of Titan atmosphere at low altitudes.

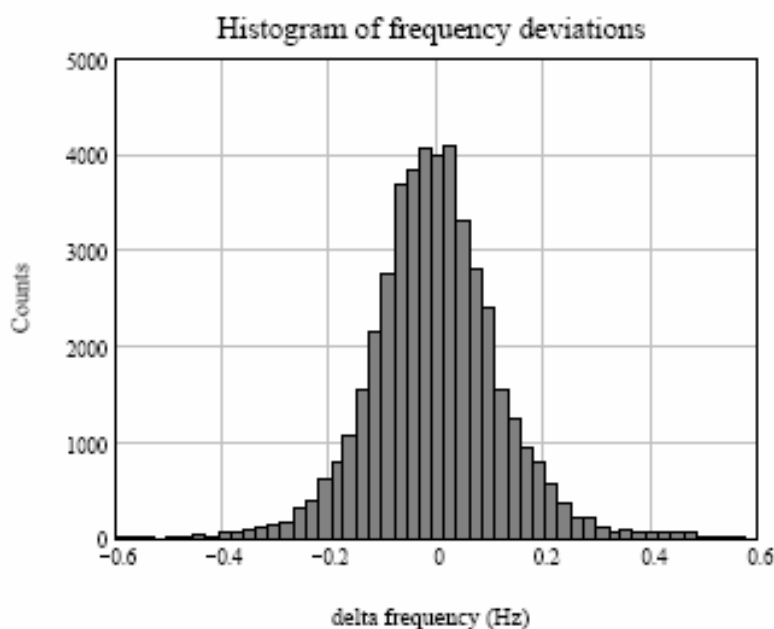


Fig. 8.17. Histogram of frequency deviations (after long term trend removed) for Parkes detections of “landed” phase of the mission. Distribution shows near-Gaussian shape with width ~150 mHz.

Spectral analysis (see Fig. 8.18) of the short term frequency behavior data for both parachuting and landed phases (Parkes data only) shows a distinguished feature at a frequency 60 mHz (period 15-16 s) during parachuting phase, which is absent during the landed phase. That seems to be another indication of the turbulence induced small-scale probe velocity variations on time scales close to the probe-parachute system eigenperiod.

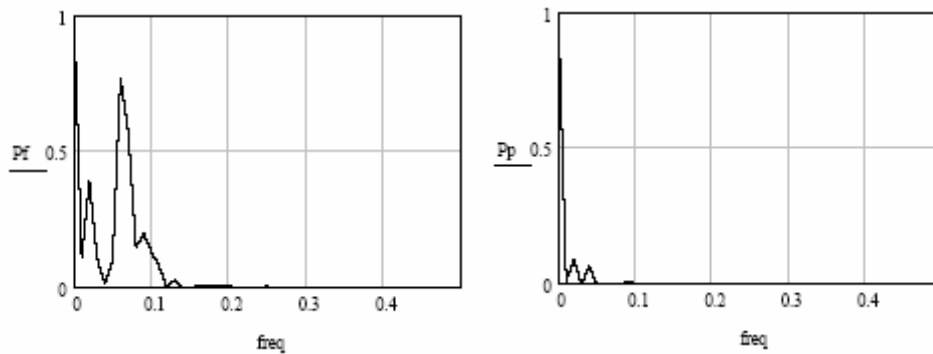


Fig.8.18. Spectra of detected Doppler frequency deviations (Parkes data) for parachuting phase of the mission (left panel) and landed phase (right panel). Horizontal axis – frequency of frequency deviations, vertical axis – relative “power” of deviations.

Even more evident, almost quasi-monochromatic oscillation-like pattern of the probe’s velocity behavior can be seen on several scans of Green Band data (Fig. 8.19) with the similar period 10-20 s and amplitude ~1 m/s.

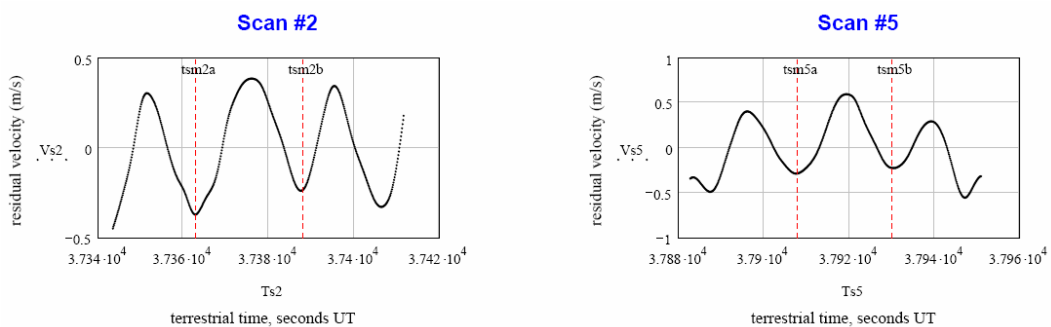


Fig. 8.19. Short time scale radial Doppler velocity oscillations of the probe’s motion during stratospheric part of the parachuting phase of the mission, as detected by Green Bank telescope.

Another interesting feature found in Parkes data is the signal frequency behavior just after the landing (Fig. 8.20). The feature shows exponential relaxation pattern

$$f(t) = A_f \times \exp(-t/TD)$$

with an amplitude $A_f = 200$ mHz and time decrement $TD = 5$ minutes. To our opinion it can be contributed to the temperature change of the probe’s local oscillator after the probe was landed into “snow” on the Titan surface. Relative to the nominal carrier

line frequency of 2.040 GHz this 200 mHz variation yields 10^{-10} change of the local oscillator frequency within 5-10 minutes after the landing.

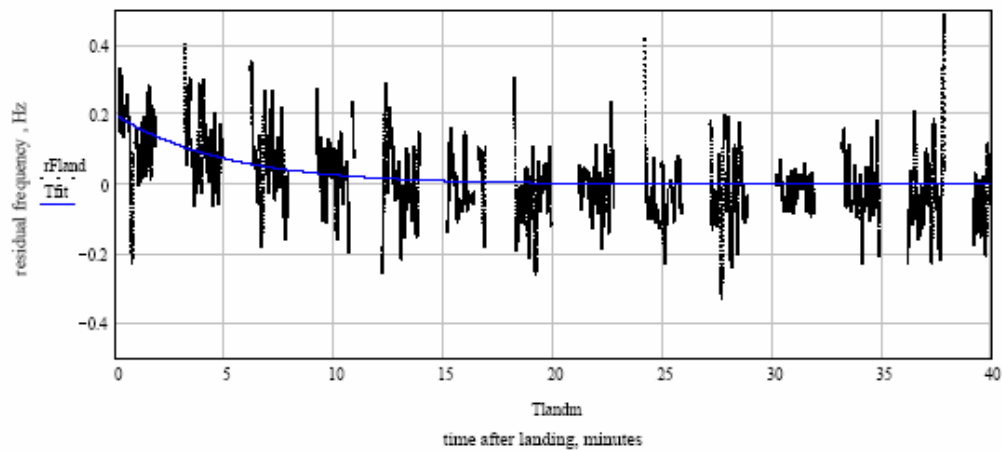


Fig. 8.20. Probe's signal frequency deviation pattern just after the landing (as detected by Parkes) – black dots, and exponential relaxation curve fit with an amplitude 200 mHz and time decrement 5 minutes – blue line.

8.7. Cross-correlation, phase referencing and phase/delay detection

After the single dish probe's signal detections (a-priori delay and apparent Doppler corrected to the geocentric frame) were properly filtered, analyzed and checked for consistency, and residual phases for phase-referencing source were available, the cross correlation of these signals were performed using the following relation

$$X_{12}(t) = S_1(t) * Conj(S_2(t)) * exp(-i\varphi_{12}(t))$$

Where $S_1(t)$ and $S_2(t)$ are the analytical (in Hilbert sense) signals from stations 1 and 2 respectively in the same "geocentric" time frame, $Conj$ stays for complex conjugate, and $\varphi_{12}(t)$ is the residual phase of the reference source broad band detection. This relation explicitly shows that any phase correction common for both stations will simply be cancelled in the cross-correlation product since it is basically a product of one signal by complex conjugate of another signal. Phase of the cross-correlation coefficient can be found as $\varphi = arg(X)$ and converted to delay using a relation $\tau = \varphi / f_0$, where f_0 is the frequency of the signal in the same frame, provided we are sure that 2π ambiguity is resolved (unfortunately, we cannot be sure in our case).

Also unfortunately, only baselines from 25m antennas (FD-VLBA, KP-VLBA, LA-VLBA, BR-VLBA, MK-VLBA and MP-ATNF) to the VLBA 100 m Green Bank Telescope (the most sensitive fully steerable radio telescope in the world) were sensitive and technically robust enough to both Huygens and phase-referencing source signals to provide reliable and continuous solutions.

Since both narrow band filtered probe's signals and reference phases are in sub-Hz bandwidth, final correlation and fringe search, as well as trajectory reconstruction was performed on my laptop computer using Mathcad-12 software platform.

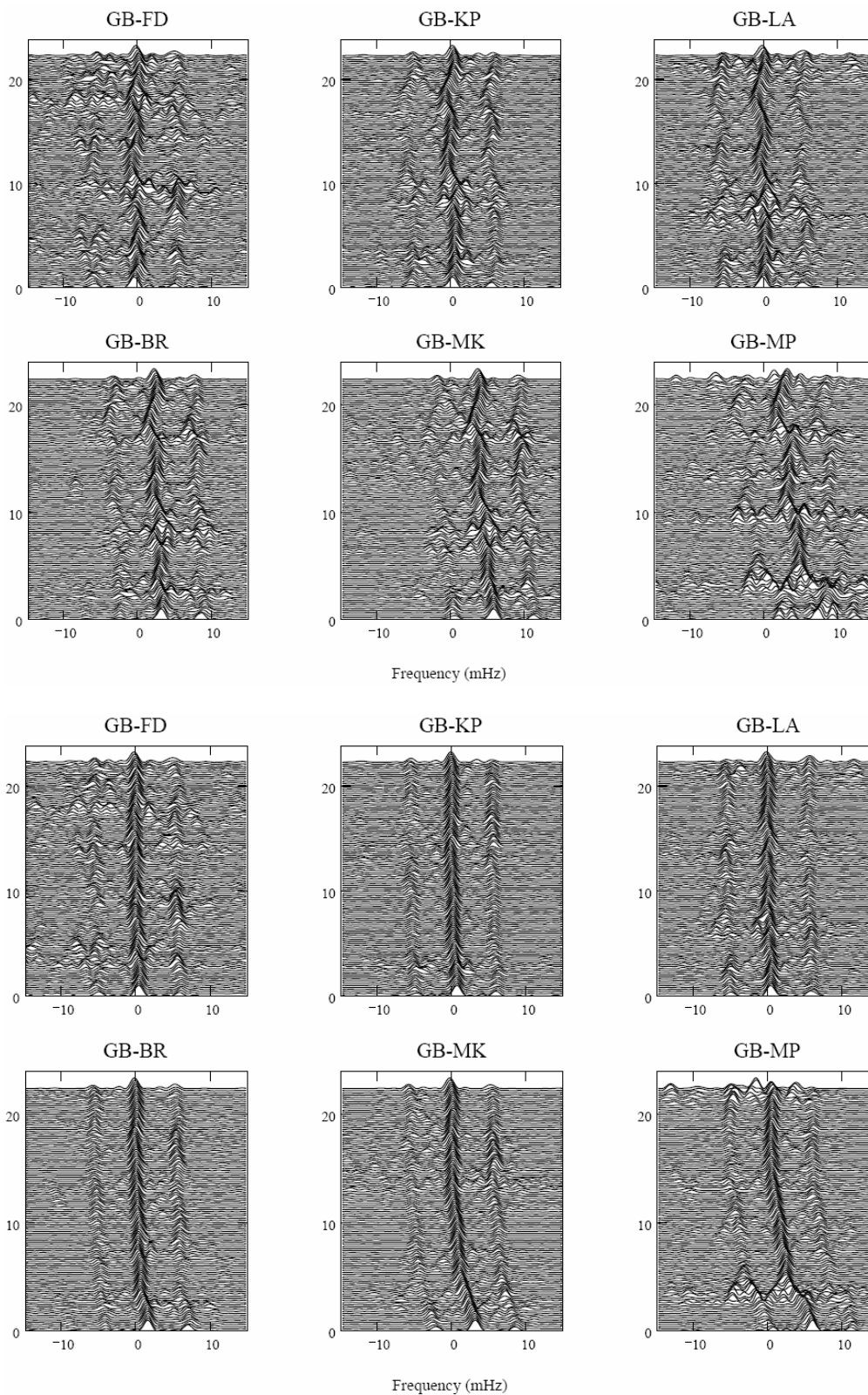


Fig. 8.21. Fringe display - Dynamic spectra of the cross-correlation coefficient for different baselines before the calibrator phases were applied (top panel) and after (bottom panel). Spectral resolution here is 1.5 mHz (corresponding to 700 s Fourier window). Sidelobes seen at 6 mHz separation from the main fringe are due to the nodding cycle 180 s window.

Fringe search for cross-correlation patterns was performed using different Fourier windows in time domain in a range 100 to 1000 s. The 700 s window (with high overlapping ration of 8-16) was found to be the shortest one to yield the reliable fringe detection, embracing 3-4 nodding cycles.

Fig. 8.21 shows the fringe search display results for 700 s and 16 times overlapping Fourier window without and with reference phases applied.

It clearly illustrates that it would be simply impossible to get phase/delay solutions without phase referencing for such a weak signal as we got from the Huygens probe. Phase referencing not only removed a considerable (several mHz) long term bias of the fringes, but also corrected them for shorter term frequency/phase excursions at sub-MHz level.

These dynamic spectra allowed us to sample the phase-referenced fringe frequency with sub-mHz accuracy, as it is shown in Fig. 8.22, left panel.

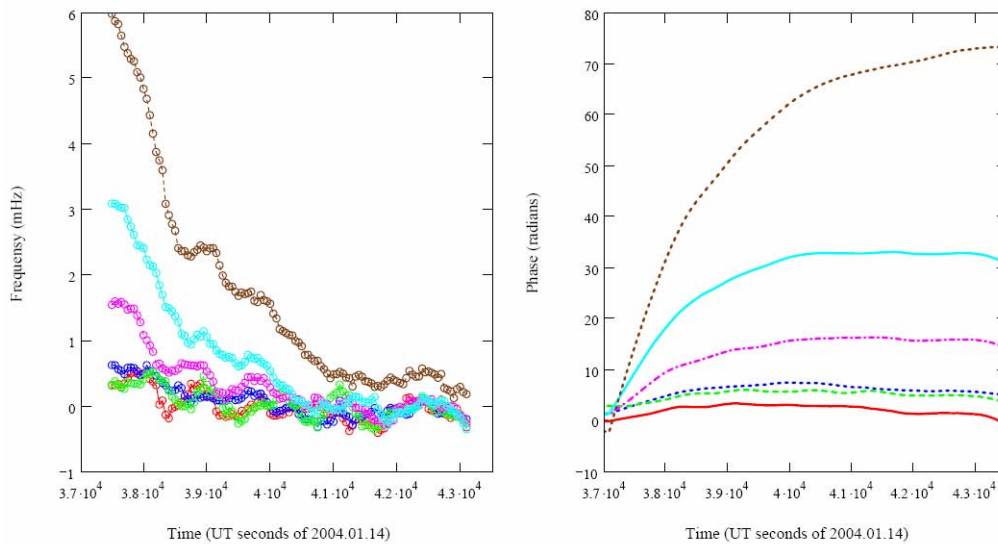


Fig .8.22. Baseline based and phase-referenced fringe frequency detections obtained with 16 times overlapping 700 s Fourier window (left panel) and fitted phases, 500 s window, 16 times overlapped (right panel).

Phase search for the fringes was done in two steps. First, the frequency detection (as shown in Fig. 22, left) were integrated over time with zero integration constant. These phases were applied as an additional correction for a fringe search. They affectively stopped the residual fringe rate to several microHz level (less than one cycle in 2 hours). The residual phases after this first iteration are shown in Fig. 8.23.

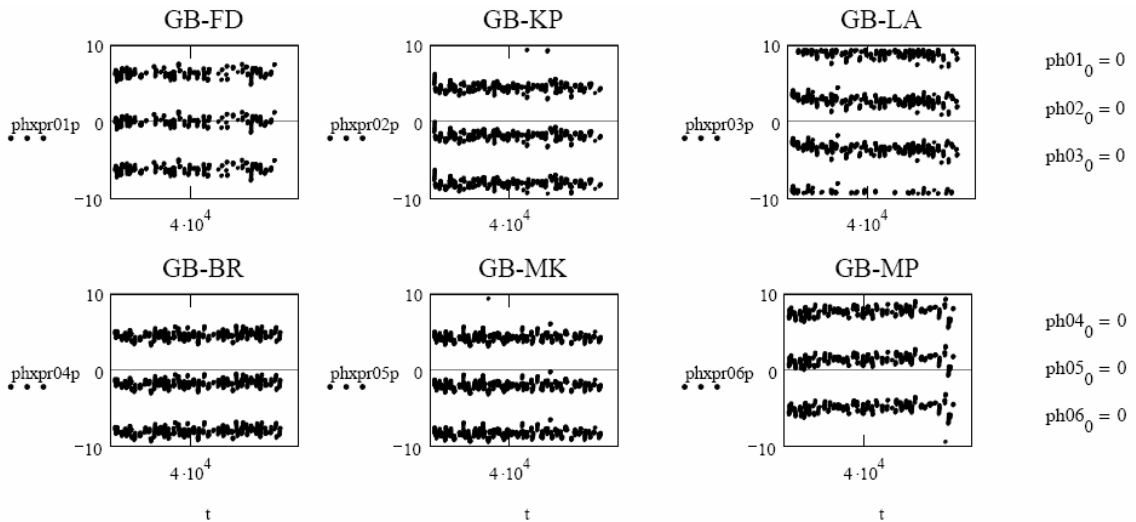


Fig. 8.23. Baseline based residual phases after first iteration of fringe search. Horizontal axis – time (s), vertical axes – phase (radians), covering about 3 cycles (± 10 radians).

Note that these residual phases are 2π repeatable, although the principle solution stays within less than $\pm \pi$ boundaries from nominal zero line.

Second iteration was to fit the polynomial with effective 500s sampling window to the principle (closest to zero line) branches of residual phases. When the first and second iterations phases are added together and applied to the fringe again, they completely stop the fringe, as it is shown in Fig.8.24, leaving the RMS of the residual phase (500 s smoothed) at the level of 0.1-0.2 radians or 10-20 ps in delay terms.

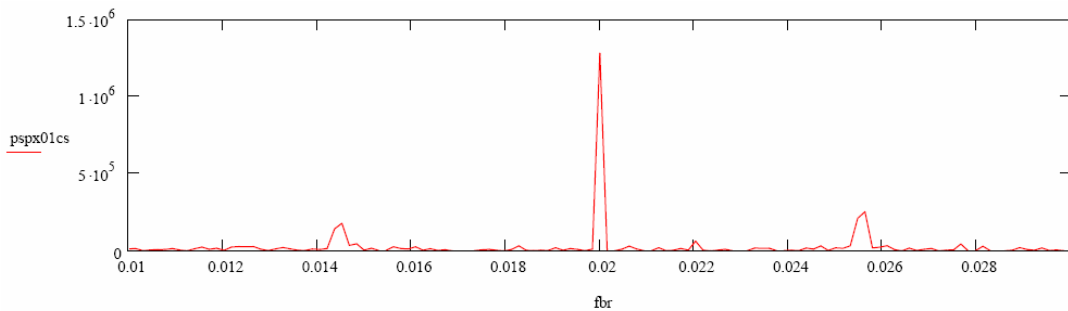


Fig. 8.24. Residual spectrum of the cross-correlation fringe on baseline GB-FD after the detected phase was removed. Fourier window 700s, resolution 150 microHz, averaging 2 hours (full GBT time range). The main lobe is shifted to 20 mHz bin. Note the main lobe is concentrated in a single spectral bin. Nodding cycle sidelobes (± 6 mHz separated from the main lobe) are also narrowed down.

Detected phases, (with 500 s independent sampling, although sampled with 2 s interval), which stop the baseline fringes, are shown in Fig. 8.22, right panel. Note that there is a noticeable phase skew of initial phases for different baselines at a level

of radians or tens of ps in delay terms or tens of km in position offset with respect to the a-priory starting point.

These phases can be converted to delays with reservation that their initial values may be biased by 2π ambiguity or any other constant phase shift. After that the delays are ready for trajectory reconstruction.

8.8. Probe's trajectory reconstruction algorithm

A-priory near field delays τ for the probe's fringe search were computed using the VTD software package developed by L. Petrov (NASA/GSFC) using the SSBC state vectors of the motion of the DTWG entry point as a zero-reference point. The same time we computed the (time dependant) partial derivatives $\delta\tau/\delta x$ of these delays with respect to the probe's displacements \mathbf{x} for all three coordinates – latitude, longitude and altitude in Titan-centric coordinate frame. These are baseline delays and partial derivatives of the baseline delays for a signal emitted at a given TBD from the position defined by SSBC state vector (as a sum of SSBC state vector of the center of Titan and Titanocentric state vector of the probe at the same TBD) and measured at Earth by two stations at a given UTC, which is light time related to the TBD of emission.

Given the Jacobian of these partial derivatives \mathbf{P} and measured and calibrated delays \mathbf{T}_m are available, the trajectory vector \mathbf{x} can be in principle reconstructed by inverting the so-called mapping equation

$$\mathbf{T}_m = \mathbf{P} * \mathbf{x}$$

Least mean square inversion of it can be found as

$$\mathbf{x} = (\mathbf{P}^T * \mathbf{P})^{-1} * \mathbf{P}^T * \mathbf{T}_m$$

Nevertheless, by the specific nature of VLBI, inversion of the matrix $(\mathbf{P}^T * \mathbf{P})^{-1}$ is an ill-determined in the case of 3 coordinates and equation cannot be resolved without applying other constrains to reduce the number of unknowns in the vector \mathbf{x} from 3 to 2.

Potentially it is possible to use the radial Doppler velocity and integrate it into the radial distance and use it as constrain, but it will involve another unknown integration constant.

In our case we decided to use the DTWG altitude as constrain to reduce the number of unknowns from 3 to 2.

Another complication is caused by the fact that our phase/delay solutions are effectively 500 s smoothed due to SNR reasons, so to use the DTWG altitude we have to smooth is with the adequate kernel. Fig. 8.25 illustrates the effect the smoothing caused to the DTWG altitude. The 500 s kernel effectively removes 500 s at the start and at the end of the observation; these two intervals should be treated as a smoothing filter set-up time.

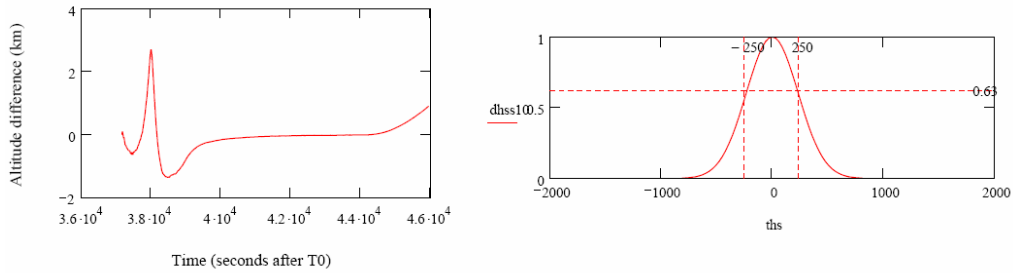


Fig. 8.25. Difference between the 500 s smoothed and original DTWG altitude (left) and Gaussian kernel used for smoothing (right).

After splitting the Jacobian matrix \mathbf{P} in the mapping equation in to parts (\mathbf{P}_t is responsible for coordinates \mathbf{x}_t tangential to Titan surface, e.g. latitude and longitude , and \mathbf{P}_a responsible for altitude coordinate \mathbf{x}_a) the mapping equation can be re-written in the form :

$$\mathbf{T}_m - \mathbf{P}_a \mathbf{x}_a = \mathbf{P}_t \mathbf{x}_t$$

and its inversion in the form :

$$\mathbf{x}_t = (\mathbf{P}_t^T \mathbf{P}_t)^{-1} \mathbf{P}_t^T (\mathbf{T}_m - \mathbf{P}_a \mathbf{x}_a)$$

where the matrix $(\mathbf{P}_t^T \mathbf{P}_t)$ is now invertible so the solution can be found and we proceed this way. This modified mapping equation also allow to compute the error scatter ellipses and “clouds” in Monte-Carlo way, when substituting the $(\mathbf{T}_m - \mathbf{P}_a \mathbf{x}_a)$ term in the left side by noise vectors with proper RMS.

Fig. 8.26 illustrates the structure of matrix \mathbf{P}_t . These partial derivatives are close analogy of the UV coordinates used in VLBI for far field source mapping.

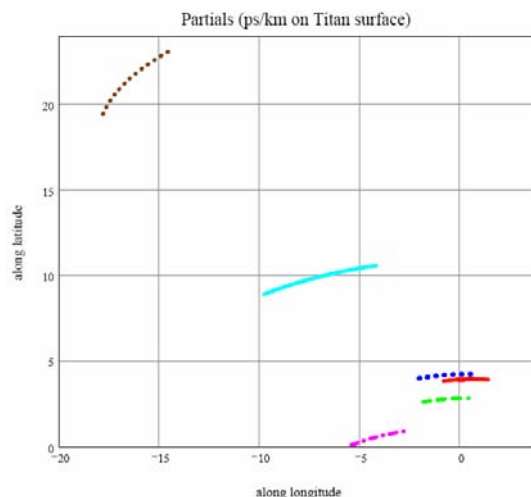
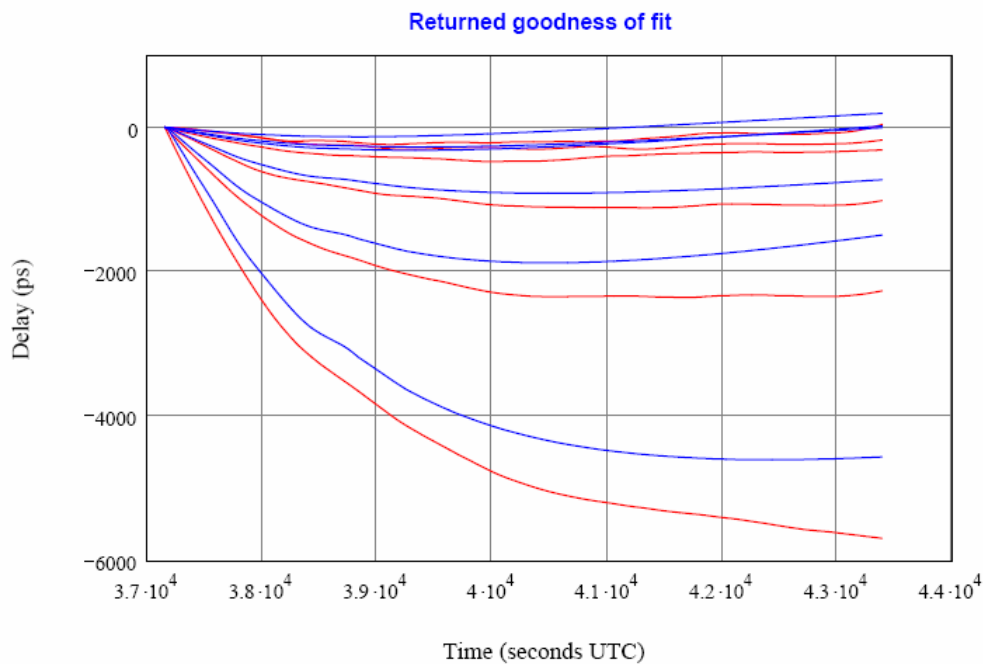


Fig. 8.26. Partial derivatives of baseline delay by the offsets on Titan surface for baselines FD, KP, LA, BR, MK and MP to GBT, in ps/km. The longest baseline, GB-MP has a spatial sensitivity ~ 20 ps of delay per 1 km of the probe displacement along both meridian and circle of the nominal latitude/longitude of the entry point.

As the zero iteration of the trajectory reconstruction, we started with direct feed of the DTWG trajectory into our mapping equation to get the delays which would be measured if the probe will move along it.

The returned delays (as illustrated in Fig. 8.27) show the significant difference with respect to the measured delays. Here the initial phase offsets of measured delays (red lines) were set to 0, since we cannot exclude 2π bias or any other initial phase bias in our measurements, so to fulfill the assumption that DTWG entry point and our entry point coincide exactly. The difference between measured delays (red line) and predicted from DTWG trajectory (blue line) differ by ~ 500 ps on the longest baselines, well above the expect noise level, and it corresponds to 20-30 km offset over the time range of about 2 hours.



Measured delays (red) and returned delays of DTWG trajectory

Fig. 8.27. Comparison of the measured delays for our baselines (red lines) and delays computed by feeding the mapping equation with the DTWG 3-D trajectory (blue lines).

At the first iteration of the trajectory reconstruction we fed our measured delays into the altitude modified mapping equation and computed the 2π ambiguity error ellipses and noise scatter ellipses based on the residual goodness of fit errors. Fig. 8.27 illustrates the result in Titano-centric coordinates where X axis goes along the longitudinal circle and Y-axis goes along the meridian in South-to-North direction. The entry point is at the right side of the plot. Red line represents the trajectory solution, black error cloud represents the solution noise, a black ellipse at the starting point of the trajectory represents the 2π ambiguity error ellipse, a blue ellipse represents the 3σ error scatter noise based on the RMS error of goodness of fit, which (baseline averaged) is about 40 ps. The overall motion is Westward with tilt to South.

Fig. 8.28 shows the residual delays for different baselines after the first iteration of trajectory reconstruction. Residual delays clearly show systematic trends which can be explained by possible ionospheric gradients between the reference source and target (38 arcmin distance). We checked possible delay gradients using the standard ionospheric model, and estimated delay gradients can be in the range 10-50 ps and vary with the time, as it is shown in Fig. 8.29.

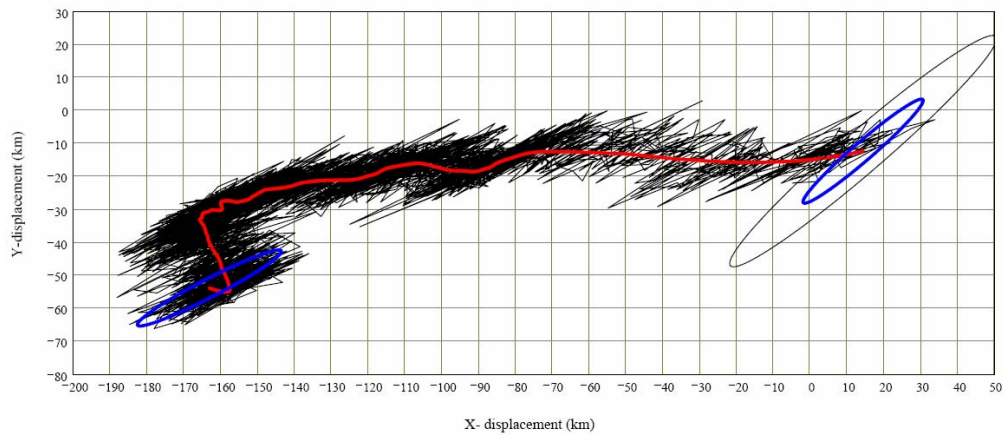


Fig. 8.28. The first iteration of the trajectory reconstruction using the modified mapping equation. The origin of the grid corresponds to the starting point of the DTWG trajectory in the IAU Titan system. The horizontal and vertical axes correspond to deviations (in kilometres) from the origin along the latitudinal circle and meridian, respectively.

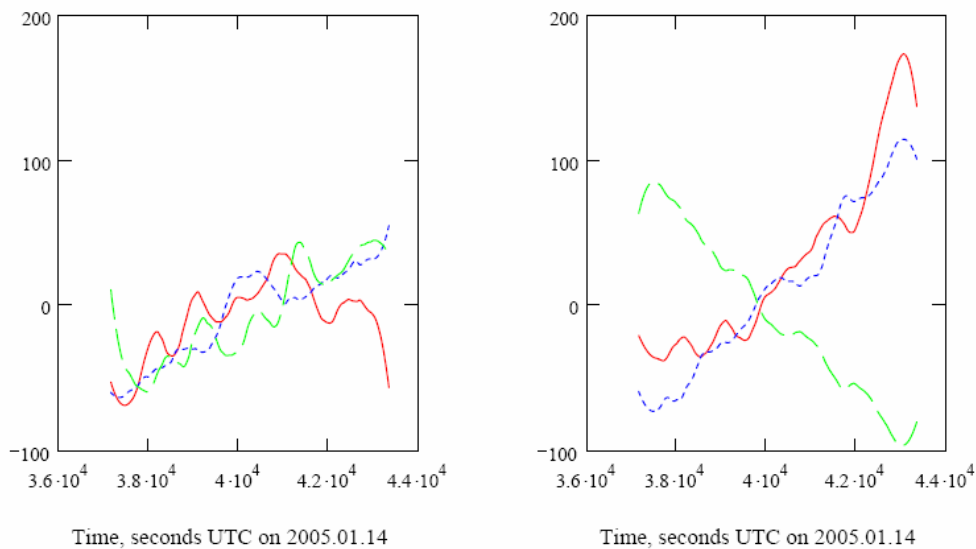


Fig. 8.29. Residual delays (goodness of fit) for first iteration. Short baselines left panel (red – FD, blue KP, green LA), long baselines – right panel (red – BR, blue – MK, green – MP).

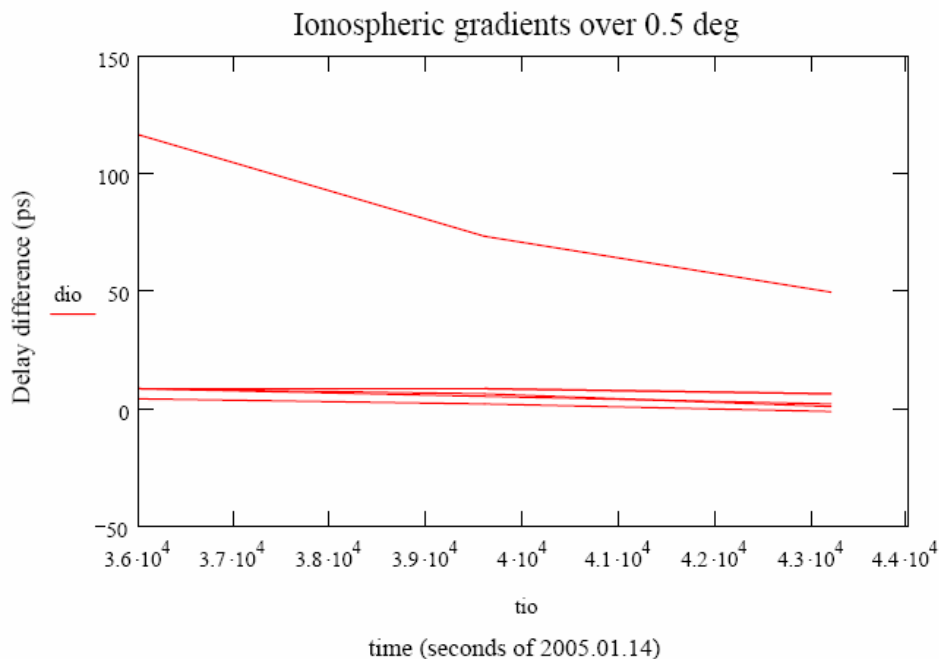


Fig. 8.30. Estimation of the possible ionospheric delay gradients between ref.source and Titan for our observation time, based on the standard ionospheric model.

Systematic character of the residual delay after the first iteration and sufficient redundancy of our array (6 baselines wrt 2 unknowns) and 11 independent measurement points corresponding to 500 s measurement interval over 6000s observing time span allowed us to resolve for possible linear trends in residual delays (2 free parameters per baseline). That also limited our lower altitude to ~15-20 km.

After these considerations were taken into account, the second iteration of the trajectory (presented in Fig. 8.31) reconstruction showed a considerable improvement and goodness of fit residual delays were reduced to 10-15 ps level (Fig. 8.32), so the error cloud around trajectory and error scatter ellipses were reduced by about 3 time, although the 2π ambiguity error ellipse is the same and defines an uncertainty of the starting point positioning. Further test showed that different biases of the initial phase/delay values result in parallel translation of the trajectory within a range corresponding to 2π ambiguity ellipse.

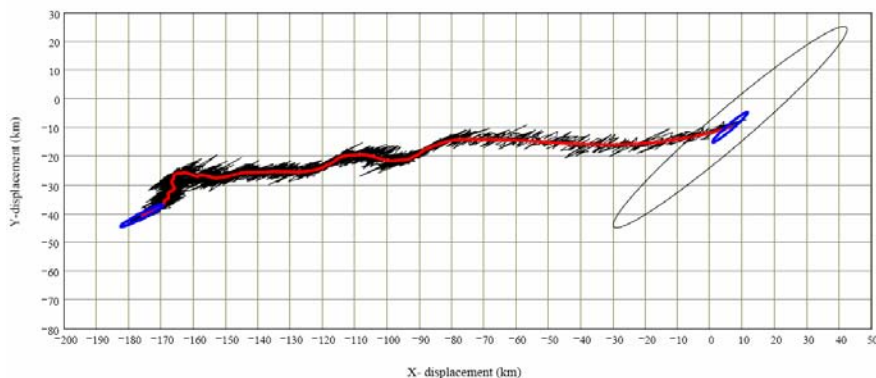


Fig. 8.31. The Probe's trajectory after the second iteration. The origin and grid – the same as in Fig. 8.27.

Error scatter ellipses computed using the goodness of fit residual RMS error 15 ps are shown in Fig. 8.32. They are variable with a time as the baseline configuration changes. They also represent the covariance between X and Y coordinate solutions.

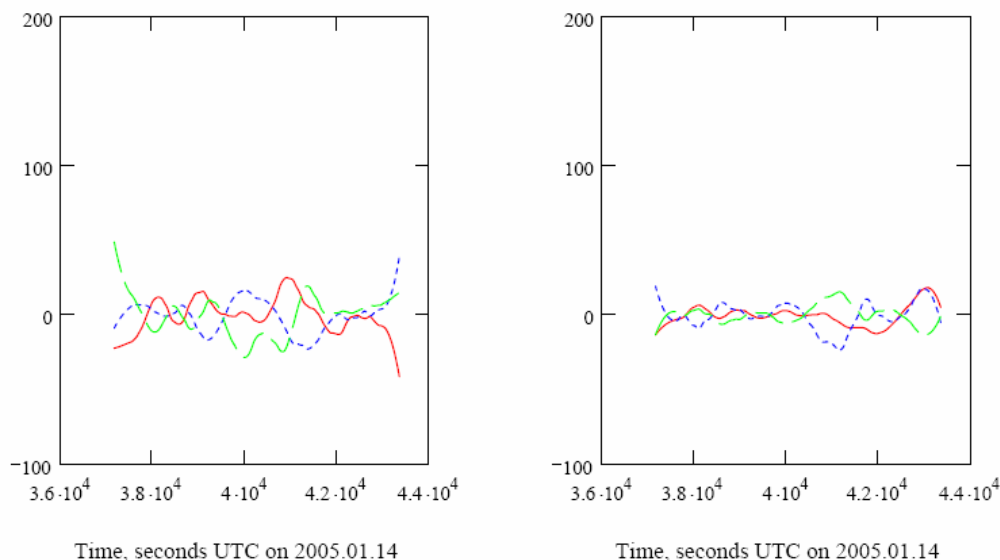


Fig. 8.32. Residual delays after second iteration. Goodness of fit (RMS of residual delays) at 15 ps level. Distribution over panels and colour coding the same as in Fig. 8.28.

It is necessary to mention that although the reconstructed trajectory (as it is shown in Fig. 8.31) appears as a continuous line, it has only 11 independent measurement points, sampled at 500 s intervals, as it will be presented in the next chapter.

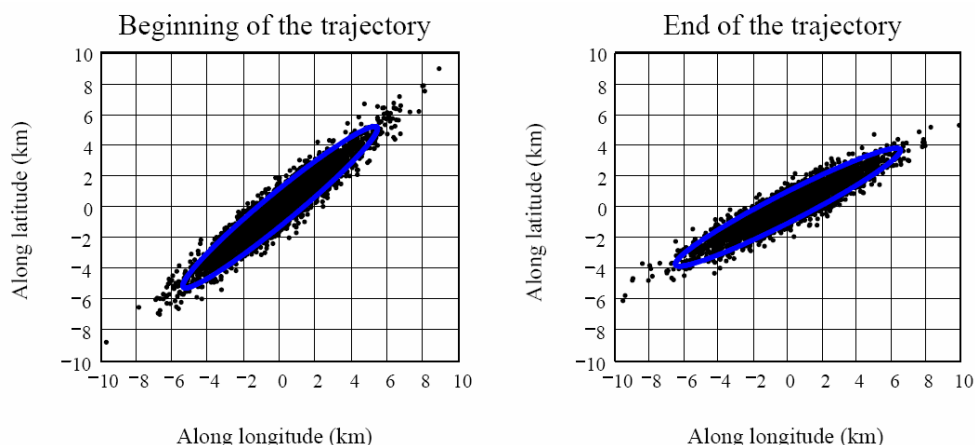


Fig. 8.33. 3-sigma error scatter ellipses (projected to the Titan surface), computed with the noise equivalent to 15 ps of the goodness of fit RMS error of the second iteration. 1Sigma semi-axis size of the ellipses is 0.5 km for shorter semi-axis (along the 30 ps/km sensitive baseline GB-MP and 15 ps/km sensitive baseline GB-MK) and 2.5 km along the longer semi-axis (defined by the GB to continental VLBA baselines).

8.9. Resulting trajectory and meridional wind

First, let us count the number of degrees of freedom in our solution.

As it was mentioned in the previous chapter, we had 11 independent measurement points per each of 6 baselines considering the 500 s sampling interval due to SNR issues to get reliable phase-referenced solutions for phase and delay. That totals to 66 degrees of freedom in our input data set. Two degrees of freedom per baseline were absorbed by introducing 2 free parameters to self-calibrate phase gradients, leaving us with 54 degrees of freedom left. Introducing the altitude constrain into our mapping equation we removed another 11 degrees of freedom, resulting with 43 of them left. Solving the mapping equation for 2 coordinates from 6 baselines reduced the number of degrees of freedom by a factor of 6 for each coordinate, although improving the statistical weight per each solution by a factor of something between 1 and $\sqrt{6}$, giving us 14 degrees of freedom or 7 per each coordinate (longitude and latitude).

This is just enough to calculate 2 significant parameters for each of the coordinates: offset and velocity with respect to a-priori trajectory (DTWG trajectory in our case).

The net result is presented in Fig. 8.34 and Table 8.4.

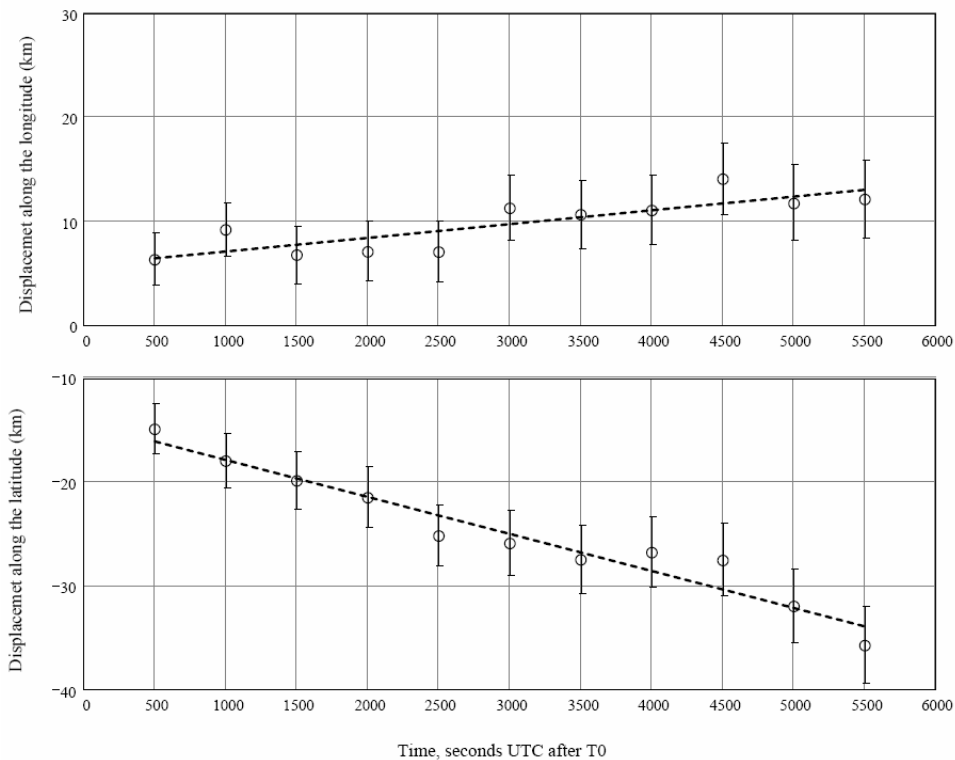


Fig. 8.34. Position and velocity offsets of VLBI trajectory with respect to the DTWG trajectory for the time range from T0+500 s to T0+5500 s.

Table 8.4. Position and velocity offsets of VLBI trajectory with respect to the DTWG trajectory for the time range from T0+500 s to T0+5500 s.

Quantity	Value	Error (1 sigma)
Longitudal position offset	7.0 km Eastward	2.0 km
Longitudal velocity offset	1.5 m/s Westward	0.4 m/s
Latitudal position offset	14.0 km Southward	2.0 km
Latitudal velocity offset	3.5 m/s Southward	0.4 m/s

Fig. 8.35 shows the 3D reconstruction of the Huygens descent trajectory based on the 2D data represented in Fig 8.31 and altitude values from the DTWG data base [11].

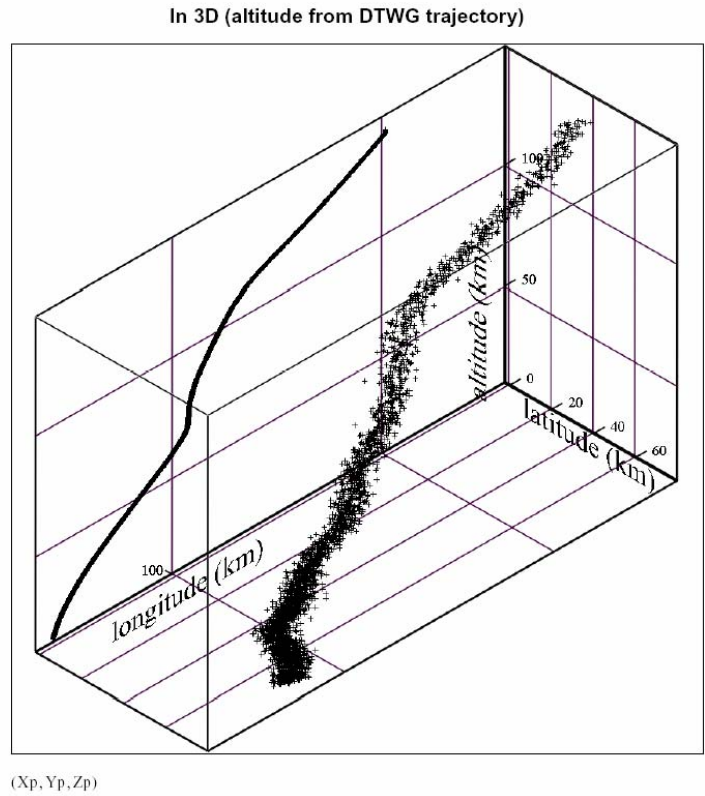


Fig. 8.35. 3D Huygens trajectory based on the 2D VLBI data and altitude measurements from the DTWG data base [11].

9. VLBI Delay Computation

9.1. VLBI Time Delay

The measured quantity in VLBI experiments is the delay in arrival time of a signal at two stations. More precisely, it is the difference of two proper time intervals. Imagine two observers, each with a clock; at some epoch in the past the clocks were synchronized. A signal arrives from some direction, is detected by each observer and tagged with his clock time. The difference between these two times is the fundamental VLBI observable.

The software packages which compute *a priori* VLBI delays have been developed incrementally over 40 years [10]. The absolute precision of these models is of order 0.1 picosecond (although unpredictable contributions, such as the ionosphere and troposphere, limit the *a priori* accuracy to a few nanoseconds). The difference between the observed and expected delays can be used to constrain model parameters such as source coordinates or structure, or antenna location.

In the analysis of the Huygens probe observations, we used the VTD software for VLBI Time Delay estimation [L. Petrov, private communication]. The delays calculated by this software are consistent at the 0.1 ps level with those produced by the “consensus model,” the software suite used to reduce VLBI observations which define the International Celestial Reference Frame and the International Terrestrial Reference Frame [IERS Technical Note No. 32, 2004]. An important additional feature of the VTD package is that sources in the near field of the Earth, where wavefront curvature will contribute more than 0.1 ps to the time delay, are treated correctly. On an Earth-diameter baseline, wavefront curvature would contribute a delay of 1ps for a source 30 light years distant. Obviously, it is a significant effect for Titan. VTD uses the JPL DE403 ephemeris for calculations involving solar system object state vectors, such as the gravitational deflection of light.

9.2 Huygens VLBI Time Delay Calculation

The difference between the predicted and observed delays can be interpreted as a position shift of the source. Over time, we have used several reference positions for the Huygens probe. Most recently, we have adopted the DTWG3 trajectory as a reference [11]. In these data files the reconstructed Titan-centric coordinates of the Huygens probe as a function of time are tabulated. As fiducial point we take the first entry in file HUY_DTWG_DESCENT_POS.DAT:

UTC	Altitude (km) wrt Surface Impact Point	West Longitude (deg)	Latitude (deg)
2005-01-14 09:11:54.999	145.21422000	195.910000	-10.340000

This point, fixed with respect to the Titan’s centre but otherwise moving as Titan does in the Solar System, is taken as a reference position for all times in the experiment.

The model Huygens delay is computed by transforming the Titan-centered fixed coordinates to time-varying Solar System Barycentric coordinates with the SPICE package (cspice, the C-language implementation, [12]). The SPICE kernels used for this coordinate transformation are: naif0008.tls (a leap seconds kernel file), 050214R_SCPSE_04336_05015.bsp (a reconstructed ephemeris of the Saturn

system taken from the JPL Cassini mission site), and cpck11Aug2006.tpc (a planetary constants definition file that includes Titan).

VTD takes the SSBC coordinate vectors as input and produces model delays at desired times.

9.3 VLBI Time Delay Partial Derivatives

To interpret the Huygens residual delays as motion on the scale of kilometres, the function $\tau(\vec{X})$ (capitals indicate SSBC coordinates) must be characterized in the vicinity of the model delay, $\tau(\vec{X}_0)$. This is done numerically by computing model delays for various deviations around the fiducial \vec{X}_0 .

We take the plane passing through the fiducial point and perpendicular to the line from the fiducial point to Titan's centre. We would like orthonormal vectors tangent to latitude Φ , longitude Λ , and altitude r at \vec{x}_0 (lowercase indicates Titan-centric rectangular coordinates). SPICE provides a function to deliver the Jacobian for the transformation from planetographic to rectangular body-centred coordinates,

$$J = \begin{vmatrix} \frac{\partial \Lambda}{\partial x} & \frac{\partial \Lambda}{\partial y} & \frac{\partial \Lambda}{\partial z} \\ \frac{\partial \Phi}{\partial x} & \frac{\partial \Phi}{\partial y} & \frac{\partial \Phi}{\partial z} \\ \frac{\partial r}{\partial x} & \frac{\partial r}{\partial y} & \frac{\partial r}{\partial z} \end{vmatrix}_{\vec{x}_0}$$

Unit vectors along latitude, longitude, and altitude at \vec{x}_0 are created

$$\hat{e}_\Lambda = \left\| J^T \hat{x} \right\|, \hat{e}_\Phi = \left\| J^T \hat{y} \right\|, \hat{e}_r = \left\| J^T \hat{z} \right\|$$

The geometry is illustrated in Figure 1. A set of sample points near \vec{x}_0 is created, $\vec{x}_i = \vec{x}_0 + c_i \hat{e}_{\Lambda, \Phi, r}$ for a set of coefficients $c_i = \{-500, -100, -50, -10, -5, -1, 1, 5, 10, 50, 100, 500\}$, converted to SSBC coordinate vectors \vec{X}_i , and used to compute VLBI delays.

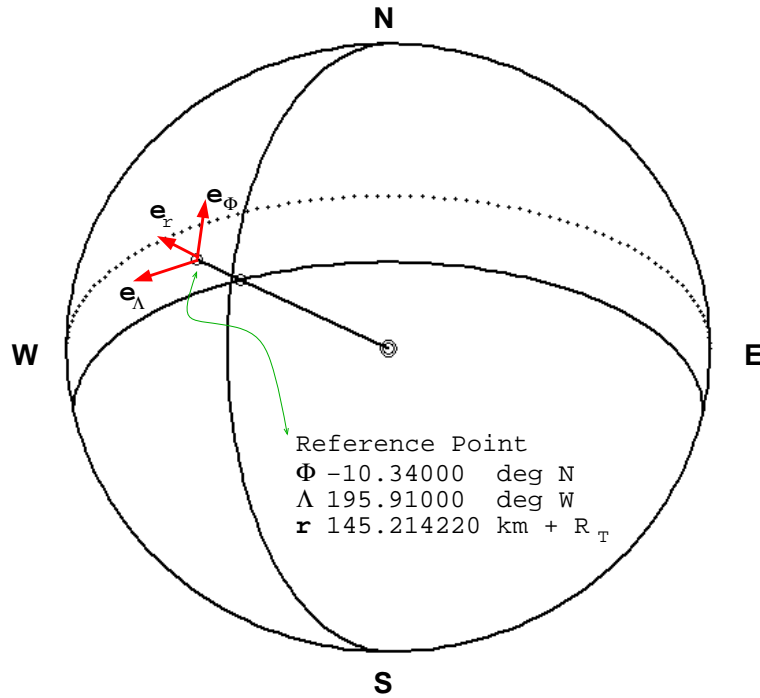


Fig. 9.1. Geometry for Huygens trajectory reconstruction. Model VLBI delays are computed for a reference point fixed with respect to the center of Titan. This point is along the DWTG3 reconstructed trajectory at a time near the first VLBI detection. The motion of the probe in physical units is derived by interpreting delay residuals as deviations in position from the reference point.

The set of delay differences $\tau(\vec{X}_i) - \tau(\vec{X}_0)$ with $(\vec{X}_i - \vec{X}_0) = u\hat{e}_\Lambda$ (or \hat{e}_Φ or \hat{e}_r) is fit to the functional form $\tau(\vec{X}_i) - \tau(\vec{X}_0) = \frac{\partial\tau}{\partial u}\Delta u + \frac{1}{2}\frac{\partial^2\tau}{\partial u^2}(\Delta u)^2$.

The delay function for deviations of 500km or less is very linear, with the ratio of the quadratic to linear fit coefficients of about 10^{-7} ; in fact the quadratic terms are not statistically significant. On the longest baselines, which are most sensitive to probe motion, the magnitude of the linear coefficient is about 20 ps/km, and the quadratic less than 2×10^{-5} (ps/km)². The latter, for a probe motion of 200km, would contribute 1ps of delay, well below our present noise level.

Given the set of partial derivatives $\frac{\partial\tau}{\partial u}$ along the directions Λ , Φ , and r , the measurement equation $d\tau = \frac{d\tau}{d\vec{u}}d\vec{u}$ can be inverted to solve for $d\vec{u}$.

10. WPCCN-2000, 3000 and 4000: High resolution (time/frequency) Doppler data extraction and post-landing analysis

10.1. Doppler data extraction from VLBI recordings

VLBI data acquisition and appropriate data processing makes it possible to analyse the Probe's signal with high-resolution in frequency and time domains. In this work-package we developed and applied to the Huygens data novel algorithms aimed at implementing this time-domain analysis of the data. In a sense, the results described in this section of the report represent a by-product of VLBI tracking of the Huygens Probe. The place of the Doppler extraction data in the overall Huygens VLBI data processing diagram described in this section are illustrated in Fig. 10.1.

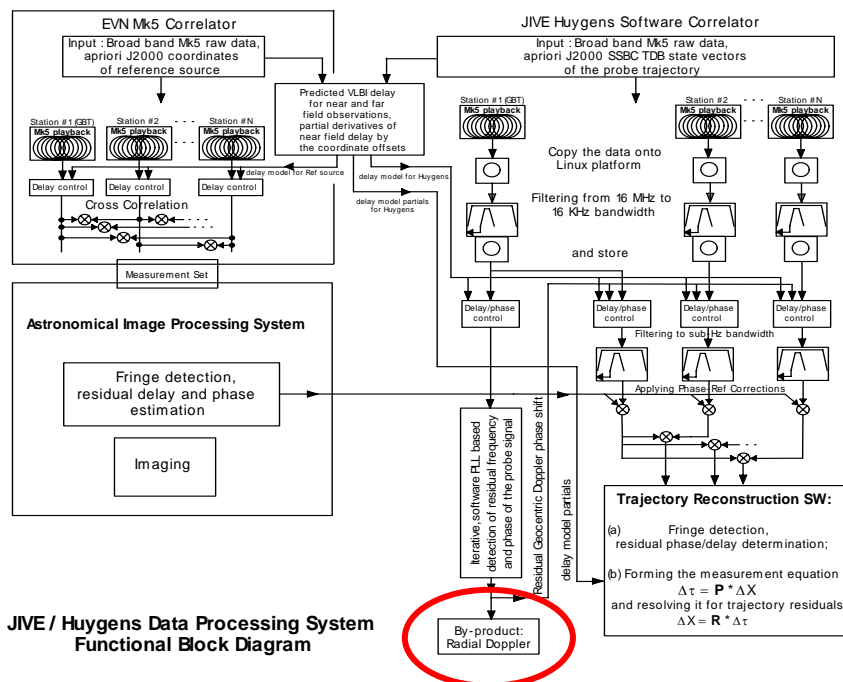


Fig. 10.1. Block-diagram of VLBI processing of the Huygens Channel A signal. The “by-product” Doppler extraction is encircled in red.

Fig. 10.2 represents the whole set of Doppler-extraction data for the entire Huygens tracking experiment based on measurements at Green Bank and Parkes. The blue curve shows the antenna noise and the red one – the residual radial Doppler frequency within a 500-kHz-wide band. The residuals resulted from extraction of a priori Doppler shift due to the relative motion of Titan and the telescopes in the geocentric system. A frequency off-set was also added to the signal to shift it closer to the centre of the 500 kHz band. Note the gap around 44,000 s for about 20 minutes corresponding to the time interval when Huygens was visible neither by GBT nor Parkes .

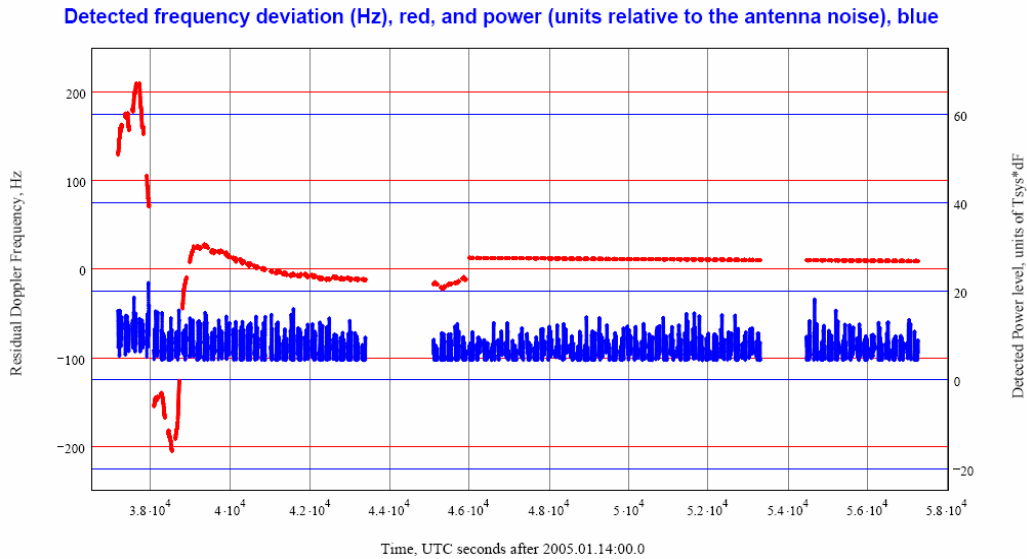


Fig. 10.2. The residual Doppler frequency of the signal detected by GBT and Parkes (red curve) after removal of Doppler shift terms defined by a priori model of motion of the Titan centre and the telescopes in the geocentric system. The blue curve shows the antenna noise temperature. The gap in the data around 44,000 s represents the interval when Huygens was below horizon at both GBT and Parkes. The gap in data around 54,000 s corresponds to the calibration scans when the Parkes telescope was pointed at a calibrator source.

The Doppler frequency data can be converted directly into the radial velocity as presented in Fig. 10.3.

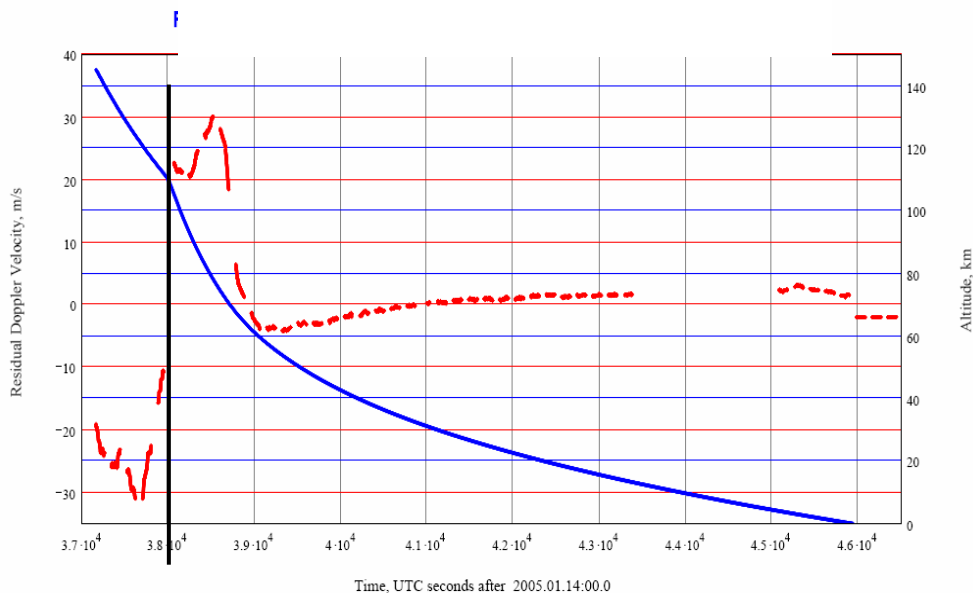


Fig. 10.3. The radial velocity based on the Doppler data shown in Fig. 10.2 (red curve) and the DTWG descent trajectory [11], blue curve) as functions of time (in seconds after 2005.01.14:00.0). The green vertical line marks the parachute exchange.

For the Probe's carrier nominal transmitting power of 3.5 W and the transmission antenna gain of 3 dBi within a +/- 60 degree cone at the distance of 8.2 AU, the carrier flux at an Earth-based receiving antenna is $P_s=50 \times 10^{-26} \text{ W} \cdot \text{m}^{-2}$ (50 Jy·Hz, where 1 Jy = $10^{-26} \text{ W} \cdot \text{m}^{-2} \cdot \text{Hz}^{-1}$). The System Effective Flux Density (SEFD) for GBT and Parkes are 12 Jy and 40 Jy, respectively.

For detection and tracking of the Chanel A carrier signal, we used $\cos^{1.0...0.25}$ FFT window (adaptively) of $\Delta t = 2$ s for GBT and $\Delta t = 4$ s for Parkes (also adaptively), aiming to achieve the power ratio $P_s/P_n = P_s \cdot \Delta t / \text{SEFD}$. This value is equal to 8 for GBT and 5 for Parkes.

As shown in Fig. 9.2, the actual mean P_s/P_n of our detections is 8.2 for GBT and 7.1 for Parkes. Note that P_s/P_n is indicative of SNR, $P_s/P_n = \eta \cdot \text{SNR}$, where the instrumental coefficient $\eta = 1/1.12$ for Mk5 2-bit sampling. Further minor degradation of SNR due to other instrumental effects is present as well.

The power ratio can be used for a priori estimates of frequency/velocity detection accuracy according to the following relations:

$$\delta f = 2 / (\Delta t \cdot \eta \cdot P_s / P_n) \quad \text{and} \quad \delta v / c = \delta f / f_0$$

Thus the stochastic accuracy of detection is 140 mHz and 110 mHz in frequency terms or 2.1 cm/s and 1.6 cm/s in velocity terms for GBT and Parkes, respectively.

10.2. The after-landing data set as a calibrator

The Parkes data set covers two different phases of the mission: parachuting and post-landing (Fig. 10.4).

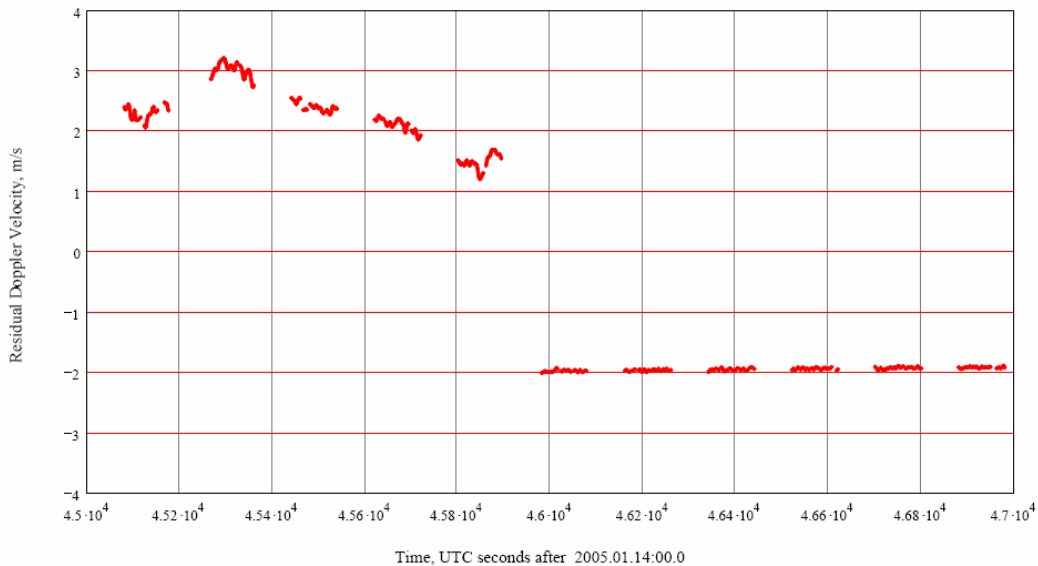


Fig. 10.4. Residual Doppler velocity estimated for five pre-touch-down and six post-touch-down scans of Parkes data.

The detected Doppler velocity for the entire Parkes parachuting phase and part of the post-landing phase, with a smooth polynomial fit removed, are shown in Fig. 10.5, together with their histograms. The after-landing Doppler measurements must be free of effects of the aerodynamical motion of the probe. It makes the after-landing data set a suitable calibrator for instrumental and algorithmic effects in the Doppler data.

While the RMS velocity for the post-landing data is 1.65 cm/s, the parachuting data shows an RMS value of 7.1 cm/s. Note that the velocity distribution for the parachuting phase deviates from a Gaussian distribution much more evidently than that of the post-landing phase of the mission.

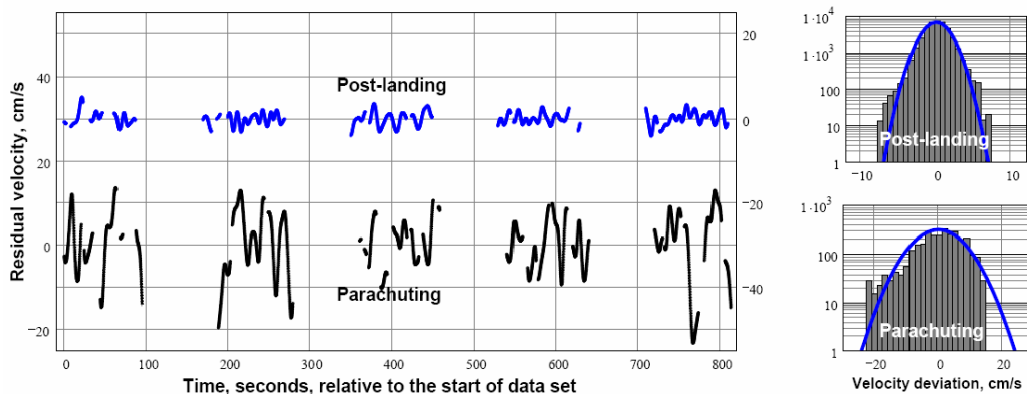


Fig. 10.5. A post-fit residual Doppler velocity for the Parkes parachuting (lower trace) and post-landing (upper trace) data sets (left panel), and their histograms (right panel). The solid line on the histograms represents Gaussian fit with equivalent RMS.

To characterize the temporal properties of these signals we computed their auto correlation functions and corresponding spectra. The ACFs were computed for a time lag range of 256 s and are shown in the upper panel of Fig. 10.6, where the ACF for the parachuting phase is scaled down 10 times for plotting. The corresponding spectra derived from the ACFs are shown in the middle panel of Fig. 10.6. A distinctive (SNR 10) spectral feature in the parachuting phase spectrum at 0.02 Hz corresponds to the probe spinning at 1.2 rpm with a visible velocity amplitude of 2 cm/s, which is in agreement with the in-situ spin rate estimates [13] and the expected velocity amplitude (taking a distance of 36 cm between the transmitter antenna and the spin axis and ~40 degree angle between a local vertical (assumed parallel to the spin axis) and our line of sight). The spin-related radial velocity variation with detected frequency, phase, and amplitude is shown in overlay with the velocity deviation curve in the lower panel of Fig. 10.6.

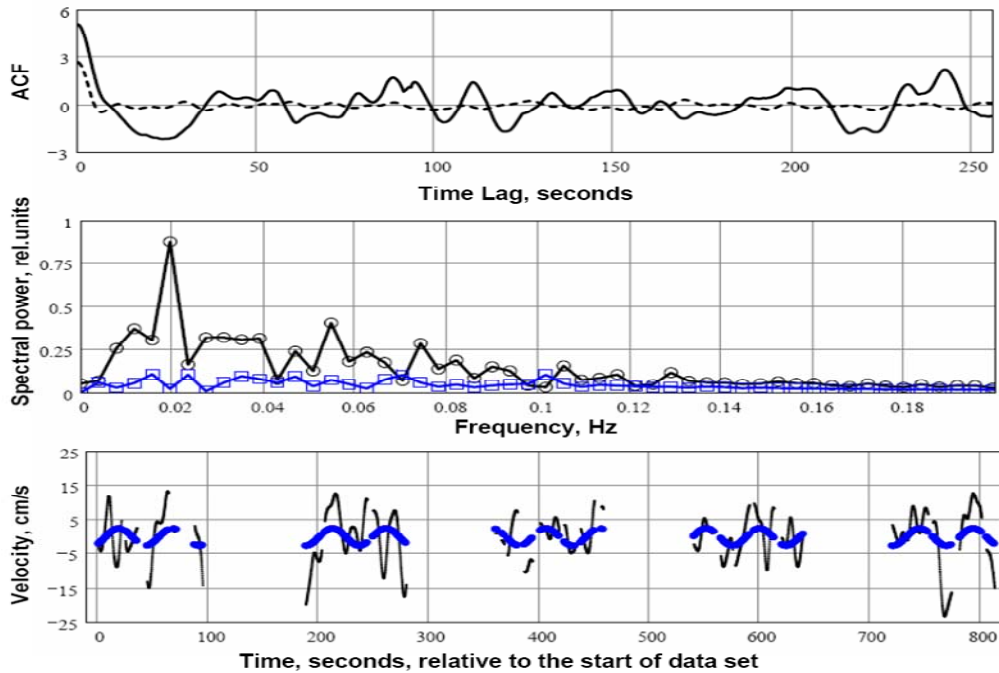


Fig. 10.6. Upper panel: ACFs for the post-landing (dash line) and parachuting (solid line) Parkes data. Middle panel: the velocity deviation spectra – boxes for post-landing and circles for parachuting, showing the 0.02 Hz and 2 cm/s probe’s spin spectral feature. Lower panel: an overlay of the estimated spin-induced radial velocity variation component (thick line) over the parachuting velocity deviation curve (thin line).

The spin-induced velocity component can be excised from the ACF of the parachuting phase, as it is a Fourier component orthogonal by definition to the rest of the data. The post-landing ACF can be considered as a system response characterization at 0 velocity deviation (accounting for such effects as the probe’s local oscillator instability, scintillations in the propagation media, telescope noise, digitization, recording and processing imperfections). It has an amplitude of $(1.65 \text{ cm/s})^2$ and FWHP time of 5.5 s. As a system response noise, it can also be subtracted from the “signal” ACF. The parachuting phase ACF (after subtraction of the spin-induced and system response ACFs) is characterized by a $(6.6 \text{ cm/s})^2$ amplitude and 8.5 s FWHP time, as shown in Fig. 10.7.

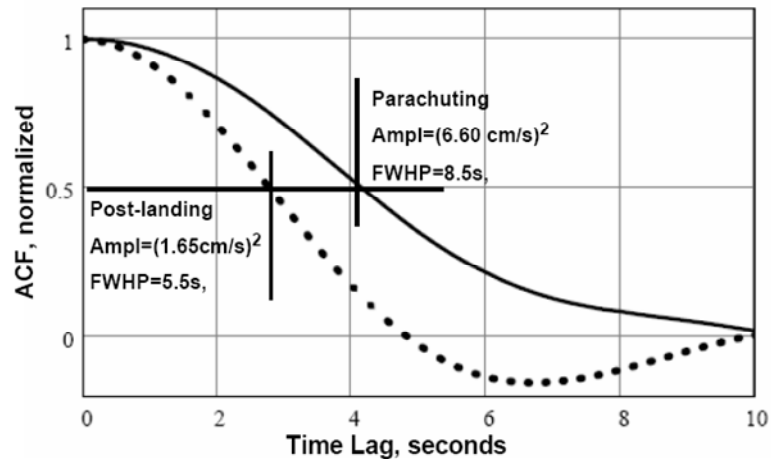


Fig. 10.7. Normalized ACFs for the Parkes data set: post-landing - dotted line, and parachuting (after spin velocity and post-landing ACFs subtracted) – solid line. FWHP markers outlined.

The post-landing data were also split into 9 segments (~15 minutes long), and the ACF analysis applied to each segment. The solutions obtained show good consistency and allow us to estimate the relative accuracy for the amplitude and FWHP determination at the 15% level. These estimates of relative accuracy can be extrapolated to the results obtained with the rest of the data.

While the characteristic velocity and FWHP time for post-landing ACF is in good agreement with our a-priori estimates of the system response characteristics, the parachuting phase ACF parameters deviate from those, and can be considered as a characterization of the short-time scale velocity fluctuations of the probe motion during the last 15 minutes of the descent.

10.3. The Green Bank data - a smooth ride data set

The Green Bank Doppler data show a variety of motion patterns. For the current study we selected the so-called “smooth ride” phase, which starts about 40 minutes after T0 and lasts until the end of Green Bank visibility.

A sub-set of the smooth ride data, a polynomial fit to it, and the residual velocity and approximate spin-induced velocity pattern are shown in Fig. 10.8.

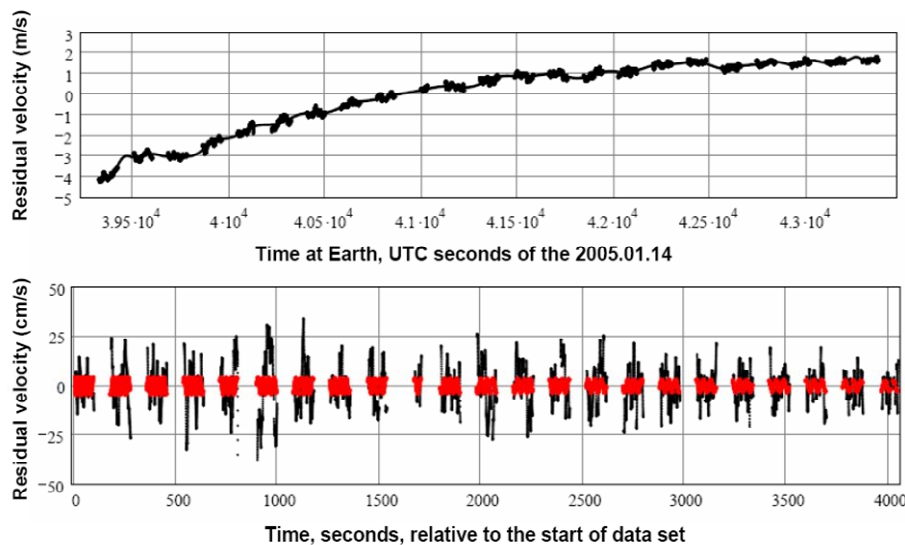


Fig.10.8. Upper panel: the smooth ride mission phase Doppler velocity (dots) overlaid with a 46th order weighted Chebyshev fit (solid line). Lower panel: the post-fit residual velocity overlaid with a pattern of a possible spin-induced radial velocity deviation for a spin rate linearly varying from 2.5 to 1.5 rpm (according to [13]).

The ACF and spectra for the post-fit data show no evident spin-induced spectral features, even after corrections for a linear trend of the spin rate, possibly due to the sporadic changes in the actual spin rate and phase, as it can be seen in the in-situ data [13]. Nevertheless, we consider that a spin-induced velocity model with an arbitrary initial phase and linear spin rate change profile corresponding to that from [9], which also accounts for the angle between the spin axis and the line of sight and the distance of the transmitter antenna from the spin center, can be a good approximation for its ACF estimate. The ACFs computed for the observational data and the spin model for a time lag span of 256 s are shown in Fig. 8, left panel. The feature seen at the time lag of 80 s can be explained as a residual of the polynomial fit (46th order over 4000 s), while another feature at 180 s corresponds to the telescope nodding cycle. For the purpose of short time scale analysis we will concentrate on the central core of the ACF, as shown in the right panel of Fig.10. 8.

The central core of the ACF has an amplitude of $(10.5 \text{ cm/s})^2$ and can be decomposed into 3 components: the expected spin contribution with an amplitude of $(2.6 \text{ cm/s})^2$ and FWHP of 10 s, a “fast near-Gaussian” process with an amplitude of $(6.3 \text{ cm/s})^2$ and FWHP time of 3.3 s, and a “slow near-Gaussian” process with an amplitude of $(7.9 \text{ cm/s})^2$ and FWHP time of 14 s.

The characteristic time of the fast process, 3.3s, is close to what can be expected for the system response noise with the 3.2 s window used for the Green Bank data set, although the amplitude is more than 3 times larger than a-priori estimates based on the signal strength, telescope sensitivity and scaling of the system response noise derived from the Parkes post-landing data. It can be considered as an upper limit for the system response noise for the Green Bank data set, although a contribution of some flight dynamics effects with this characteristic time (or shorter) can not be ruled out. The slow process can be used as a first order approximation to characterize the

short time scale flight dynamics effects observed during the “smooth ride” phase of the mission.

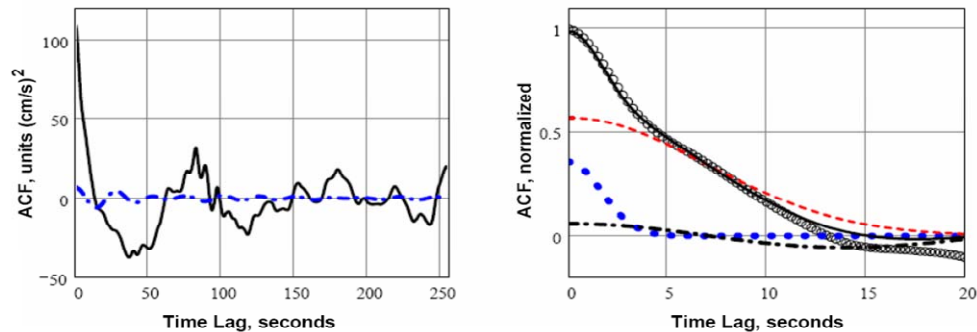


Fig. 10.9. Left panel: ACFs for the Green Bank post-fit velocity variation (solid line) and spin velocity model (dash-dot line) for the spin with a linear rate change in the range 2.5 – 1.5 rpm, transmitting antenna displacement 36 cm from the spin axis and 40 degrees angle between our line of sight and local vertical. Right panel: decomposition of the central core of the measured ACF (open circles) into 3 components – the spin-induced ACF (dash-dot line), fast Gaussian component (dot line), slow Gaussian component (dash line), and a sum of the three plotted as a solid line. The slow near-Gaussian process can be related to various flight dynamics effects.

10.4. Conclusions

- 1). The high time-resolution analysis of the Huygens Doppler extractions from VLBI data allows us to characterize the Doppler measurement system response noise as a near-Gaussian process with a characteristic time of 5.5 s for the Parkes data set and 3.3 s for the Green Bank “smooth ride” data set, with characteristic velocities of 1.65 cm/s and 6.3 cm/s (as the upper envelope) respectively.
- 2). Short time scale radial velocity fluctuations, induced by the probe’s flight dynamics effects during the Parkes parachuting and the Green Bank “smooth ride” phases of the mission, can be characterized by 8.5 and 14 s characteristic time and 6.6 and 7.9 cm/s characteristic velocities, respectively, with relative accuracies of 15%.
- 3). A clear detection (with SNR 10) of the probe’s spin-induced radial velocity variation during the last 15 minutes of the descent with an amplitude of 2.0 +/- 0.2 cm/s and frequency of 1.2 +/- 0.1 rpm is in agreement with the in-situ spin estimates [9] and validates our approach.
- 4). Detected and characterized short time-scale radial Doppler velocity fluctuations provide an indication of the presence of turbulence in Titan’s atmosphere. The observational VLBI data available allow to analyze the turbulence and flight dynamic effects further.
- 5). Analysis of the “Main Chute” and “Rough ride” phases of the Green Bank data (which would require a scan-by-scan approach), and the higher time-resolution PEa5 release of the Doppler detections, can be a subject for a further study.

11. WPCCN-1000: Archiving and maintenance of Mk5 disc-packs with raw VLBI data from Huygens VLBI tracking experiment

Raw data from all 17 radio telescopes involved in the Huygens VLBI Experiment (GG057C) arrived in JIVE either directly in Mk5 disc-packs or were translated and recorded onto Mk5 disc-packs (Fig. 11.1 top). The latter operation was needed for data from the telescopes not equipped with Mk5 DAS (see section 3.3 for details). The total amount of raw data obtained in the Huygens VLBI tracking experiment is about 27 TB. The normal practice of the European VLBI Network (EVN) as well as that of all other world VLBI networks is to re-cycle raw data medium (Mk5 disc-packs) after correlation and verification of the data. However, due to the unique nature of the Huygens VLBI tracking data, the disc-packs from GG057C have been stored at JIVE and will remain at the JIVE storage (Fig. 11.1 bottom).



Fig. 11.1. Two Mk5 disc-packs (top) and the automated Mk5 disc-pack storage at JIVE (bottom)

12. Australian Test Geodetic Experiment VT08A

12.1. Introduction

An error in the Earth-fixed coordinates of a VLBI-participating telescope, ΔX , leads to an error in the a priori rate of order $\omega_{\text{Earth}}\Delta X$, or a rate error of about 2 mHz. That is a large apparent motion. Although the phase residual introduced by a telescope coordinate errors removed to first order by phase referencing, it contributes at second order, at the level $\omega_{\text{Earth}}\Delta X(\delta\Theta)$, where $\delta\Theta$ is the distance from reference to source in radians.

Global geodetic observations have measured the locations of many telescopes to centimetre accuracy. Among the telescopes used in the Huygens observation, only the stations Hobart and Parkes had such high-precision coordinates. The stations Ceduna, ATCA, and Mopra were much less well known, at accuracies of about 10m. Better coordinates for these telescopes would benefit not only the Huygens VLBI tracking experiment but also future coordinated observations with other VLBI networks.

12.2. Experimental Setup

As first step, the program committee for the Australian Telescope National Facility (ATNF) and Long Baseline Array (LBA) approved a two-hour slot for a test observation on 16 May, 2006, named VT08A. The stations allocated were: Hobart, Ceduna, Mopra, Parkes, and the ATCA. VLBI experiments aimed at measuring station coordinates or Earth orientation parameters are termed "geodetic," as opposed to "astronomical." Geodetic observing is a more structured affair than astronomical observing. Large numbers of telescopes with standard hardware and data recording systems observe in several sessions each year, and the data are processed at centers in Bonn or Washington DC. Apart from Parkes and Hobart, the Australian telescopes lacked the standard geodetic S/X receivers and MkV recorders. The goal of this two hour test was to detect fringes on all baselines; if successful, further observations could be requested. A positional fit could also be attempted with the short data set.

Standard geodetic observations are at simultaneous S (2 GHz) and X (8 GHz) bands. This is to detect and remove the variable ionospheric phase. Because not all the participating telescopes had S/X receivers, and the ionospheric delay contribution decreases as the square of the frequency, the experiment was conducted at K (22GHz) band. Leonid Petrov (NASA GSFC) had been involved in K band surveys (arXiv:astro-ph/0609557) with the VERA telescope in Japan, a VLBI instrument dedicated to astrometric studies of Galactic structure at K and Q (43 GHz) bands (<http://veraserver.mtk.nao.ac.jp/index-J.html>). He compiled a list of bright K band calibrator radio sources visible from Australia for the experiment.

The channel configuration had to be decided as well. The MarkIII geodetic frontends have 14 baseband converters with width 2 MHz each. Typically eight observe at RCP X band, spaced over 500 MHz, and 6 at RCP S band over 100 MHz. The wide span, and the placement of the channels within the span minimizes the uncertainty in the measured group delay. However, the mode available to the LBA for this experiment allowed four channels of 16MHz each. On the one hand, wide spacing gives delay ambiguities, on the other close spacing lowers precision. Unlike MarkIII frontends, the LBA uses digital BBCs which offer better phase stability. After much discussion

among Leonid Petrov, Chris Phillips (ATNF) and John Gipson (GSFC), it was decided to arrange the channels in pairs 96 MHz apart, as shown in Fig. 12.1.

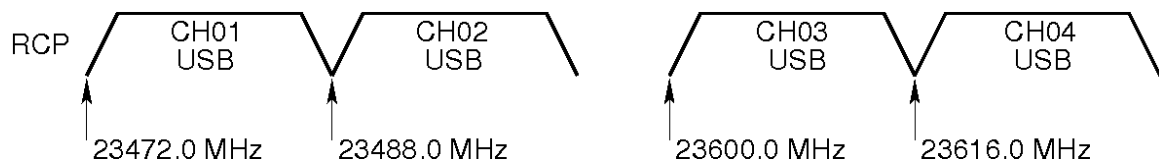


Fig. 12.1. Observing bands for the Australian geodetic fringe test observation VT08A. K-band was chosen to minimise ionospheric effects.

John Gipson wrote a schedule for the observation, which was translated by Chris Phillips for the control computers on the LBA telescopes. The experiment began on 16 May 2006 at 13:00 UTC lasted for two hours. Ten sources were observed in repeated groups of short scans of about two minutes. Two minutes is about the expected coherent integration limit, and the repeated scans are insurance against intermittent instrumental problems.

The observation went well. During or shortly after it was realized that Ceduna observed some channels at lower sideband, but the data were thought to be recoverable.

12.3. Data Processing

The data were recorded at each telescope with the ATNF PCEVN disk-based recorders. These are linux computers with PCI hardware software developed at Metsähovi Radio Observatory (MRO) to interface with the VLBI system backends. A data volume of about 225 MB was transferred over the net from ATNF HQ to another linux computer at JIVE, on which they were converted to Mk5 format with software developed at MRO. This was similar to the procedure with Huygens VLBI data. After conversion, data were uploaded to Mk5 disc-packs for playback into the hardware correlator.

An initial inspection with the EVN MarkIV correlator at JIVE was performed. Fringes were found to all telescopes except Ceduna, as shown in Fig. 12.2. System temperature at Hobart seemed surprisingly high, and the staff are investigating the cause. It happened that Ceduna recorded in two different modes during the observation, and neither were able to be decoded after considerable effort. Digital backends and recording systems generally offer improved flexibility and ecoverability, but sometimes the parameter space is larger than can be searched.

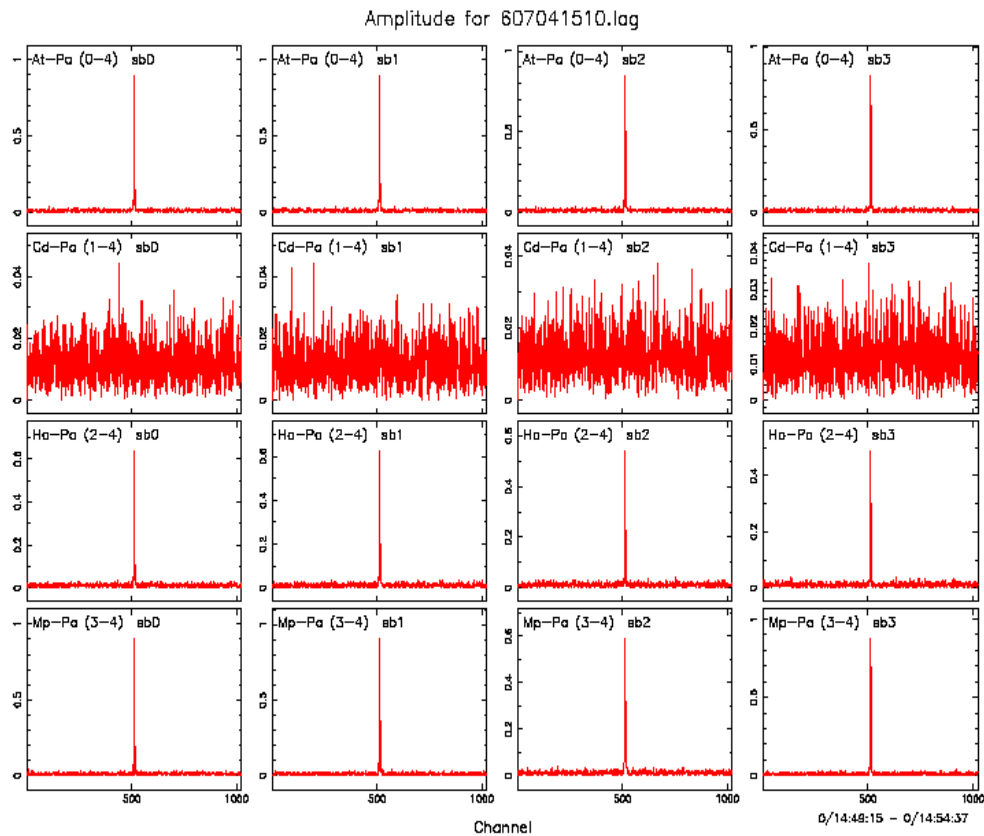


Fig. 12.2. VT08A Fringes on baselines to Parkes. Due to a recording problem at Ceduna no detection was possible.

Table 12.1 System Equivalent Flux Densities for LBA telescopes in VT08A. The high SEFD for Hobart could be due to eg feed misalignment or pointing error.

Station	SEFD (Jy)
ATCA	2110
Hobart	49030
Mopra	2850
Parkes	2170

Table 12.1 lists the calculated station sensitivities, with Hobart the clear outlier. An instrumental problem at Mopra was discovered during this checkout. Fig. 12.3 illustrates fringe amplitude oscillations on baselines to Mopra. Communication with the LBA team indicated it was known problem with the DAS at Mopra during the time of the observation.

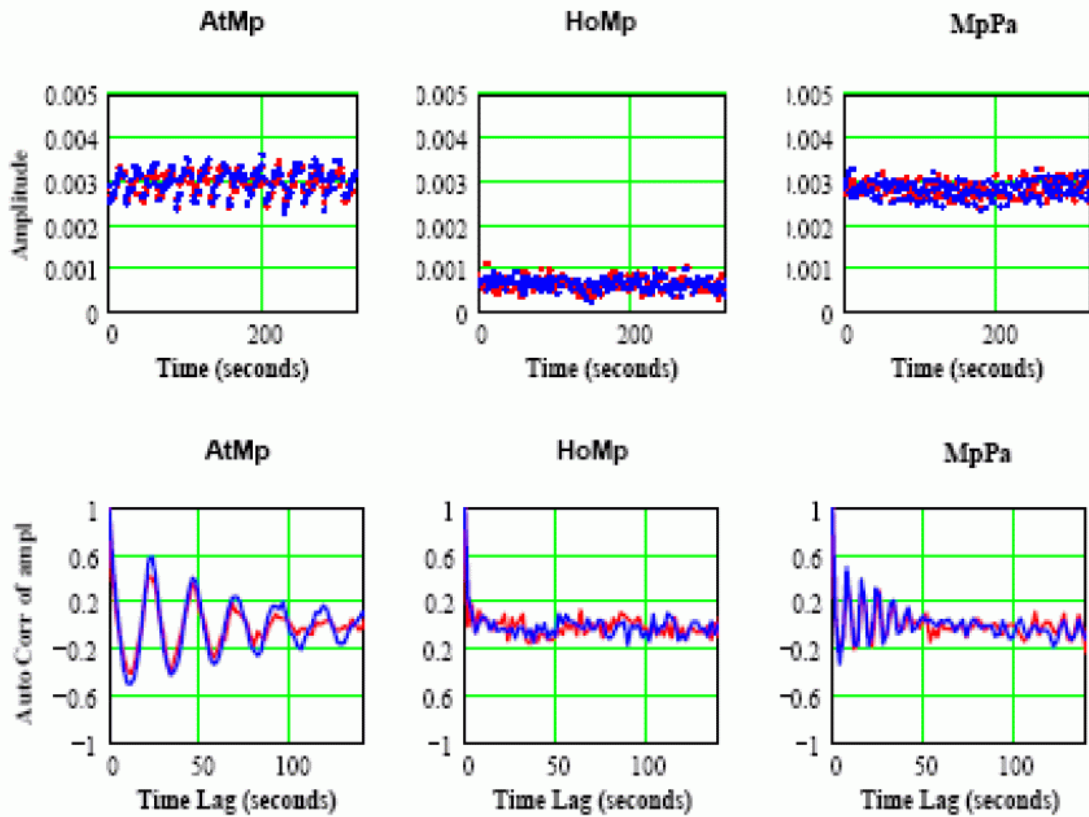


Fig.12.3. Amplitude oscillations on baselines to Mopra telescope in VT08A. Adam Deller (LBA) has reported it was a known problem with the Mopra data acquisition system at the time of observation.

The upconverted Mk5 diskpacks were sent to the MkIV correlator at Bonn and processed there during the week of 24 July 2006. The correlation dataset was analyzed by Leonid Petrov at GSFC and produced an improved estimate of station locations, presented in Table 12.2.

Table 12.2. New positions for Australian telescopes derived from experiment VT08A. The last column gives the position shift with respect to coordinates used in initial Huygens VLBI experiment data reduction. Confidence level is about 1 meter; changes to Parkes and Hobart are therefore not significant.

Station	X(m)	Y(m)	Z(m)	ΔR (m)
ATCA_014	-4751639.932	2791700.007	-3200490.456	91.267
HOBART26	-3950236.737	2522347.560	-4311562.539	0.451
MOPRA	-4682770.102	2802618.709	-3291758.912	1.807
PARKES	-4554232.006	2816758.963	-3454035.849	0.471

13. WP 6000 and WPCCN-5000: Technology demonstrations for future ESA missions

13.1. Smart-1 tracking, May - September 2006

SMART-1 is the first ESA mission to the Moon. It was launched in 2003 and orbited the Moon with a five-hour period until impact on 3 September 2006. The SMART-1 spacecraft offered a very attractive opportunity as a target for VLBI-style radio astronomy observations and verification of some approaches to data processing developed originally for the Huygens VLBI experiment. It also enabled verification of new features never exercised by European telescopes in array mode, such as different pointings for different telescopes in a single VLBI experiment (due to a close proximity of the source), interface with the ESOC Orbit Determination and Navigation, short-notice dynamic scheduling of observations. The radio astronomy campaign with SMART-1 organised by JIVE covered the last four months of the mission, from May through September 2006.

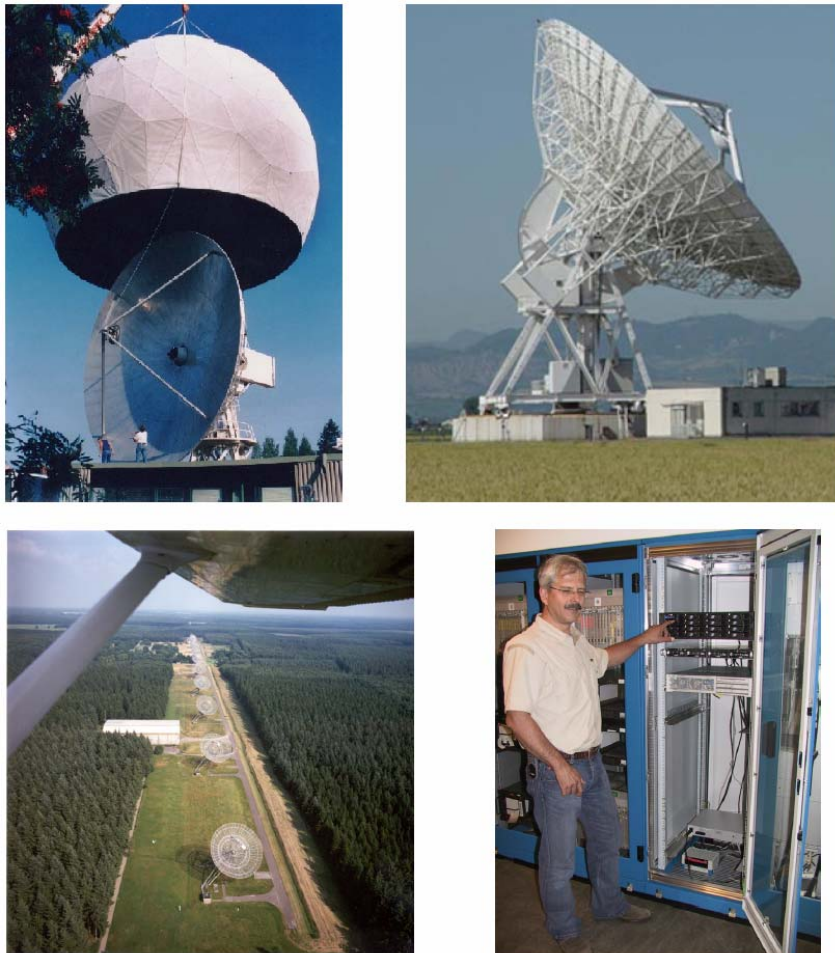


Fig. 13.1. Facilities involved in the May-June 2006 SMART-1 observing campaign, from top-right, counter-clockwise: Medicina (32 m, Italy), Metsähovi (14 m, Finland), Westerbork (only one 25 m single dish from 14 was used, The Netherlands), and data processing hardware at JIVE (The Netherlands).

In the first series of observations in May-June 2006, the SMART-1 S-band telemetry (TX) signal was observed with the three European radio telescopes shown in Fig. 13.1, Medicina (MC, 32 m, Italy), Metsähovi (MH, 14 m, Finland) and Westerbork (WB, 25 m single dish, The Netherlands). The data were recorded using Mk5A VLBI data acquisition system and moved to a Linux computer (4-core Opteron with 5 TB raid), which is also shown in Fig. 13.1. Observed Mk5A data from Medicina and Metsähovi were transported to JIVE via optical fibre network, while Westerbork data were delivered by car.

A calibrator source, J0242+1101, was observed in VLBI mode in order to synchronise the telescopes with sufficiently high accuracy. Atomic clocks at VLBI stations are usually synchronized to UTC by GPS, but are otherwise free running. Clock offsets and rates are measured at the correlator from a subset of the data, and then applied as corrections for full correlation. Fig. 13.2 shows VLBI fringes on the baseline MC–MH. Their detection enabled improved synchronization of the MC and MH local clocks from an a-priori value of several microseconds to several nanoseconds a-posteriori.

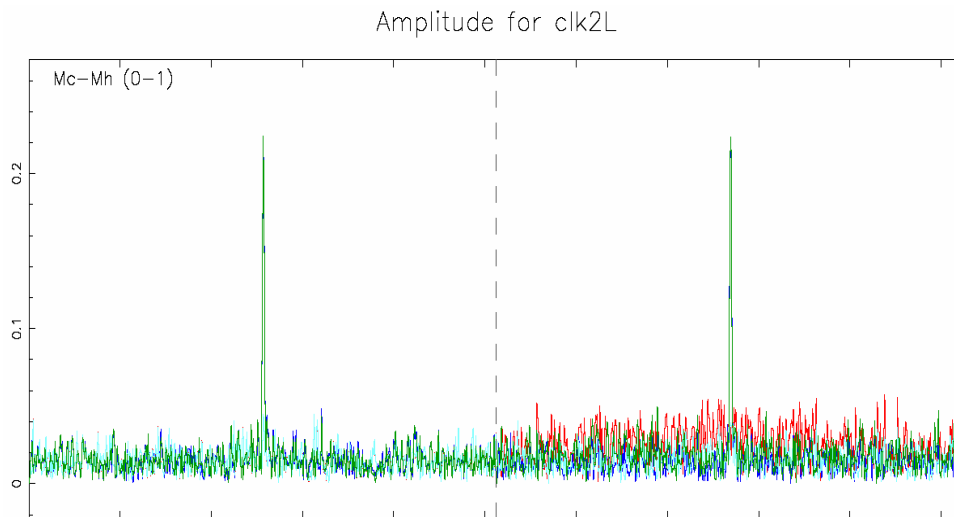


Fig. 13.2. VLBI fringes on the source J0242+1101 on the baseline MC–MH in LCP (left) and RCP (right). The horizontal axis corresponds to delay in the range $\pm 32 \mu\text{s}$, the vertical axis is correlation function (relative units). Cross-pol correlation is shown in red.

On 25 May 2006 the SMART-1 was detected at Medicina and Metsähovi with excellent signal-to-noise ratio (Fig. 13.3), close to the expected values, while Westerbork showed no detection due to technical problems (which were fixed later). Fig. 13.4 shows the dynamic spectrum of the SMART-1 TX carrier line detected at Medicina.

The quality of the signal detected with the Mk5 VLBI system enabled phase tracking of the SMART-1 TX carrier line with a frequency residual $< 1 \text{ mHz}$ corresponding to a radial velocity residual $< 0.1 \text{ mm/s}$ on time intervals of 100 s (Fig. 13.5). The factors limiting the residual tracking accuracy are propagation effects in the ionosphere and troposphere, and limited stability of the on-board local oscillator.

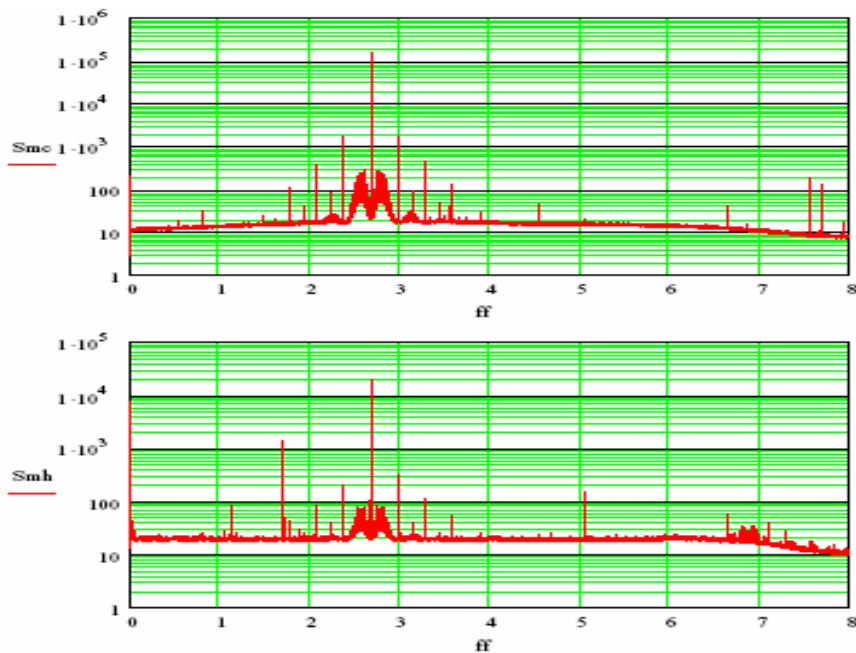


Fig. 13.3. Single dish spectra (64001 spectral channels, 125 Hz resolution, 10 s averaging) of SMART-1 S-band TX signal over an 8 MHz video band, detected by Medicina (top) and Metsähovi (bottom). The signal amplitude (vertical axis) is shown in arbitrary units. Note the presence of RFI in the band.

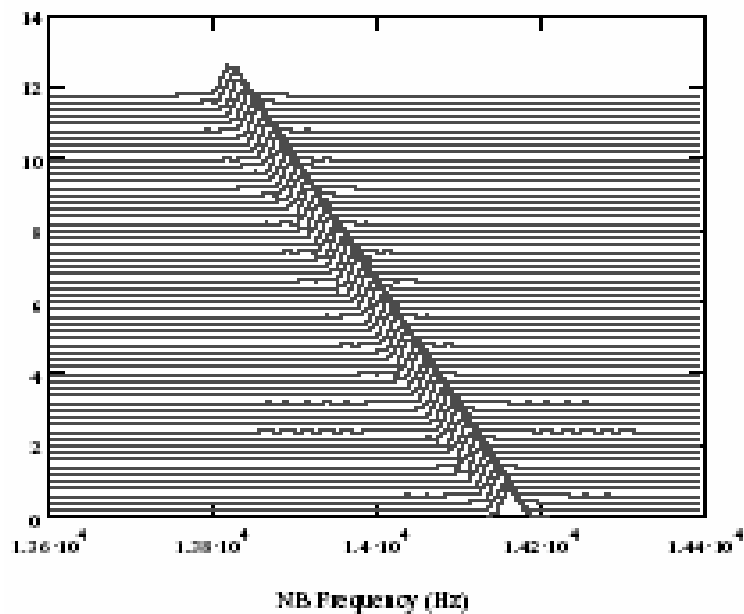


Fig. 13.4. Dynamic spectrum of the SMART-1 TX carrier line detected at Medicina telescope around the expected frequency of 2.235 GHz. Frequency resolution 24 Hz, vertical axis marked in seconds.

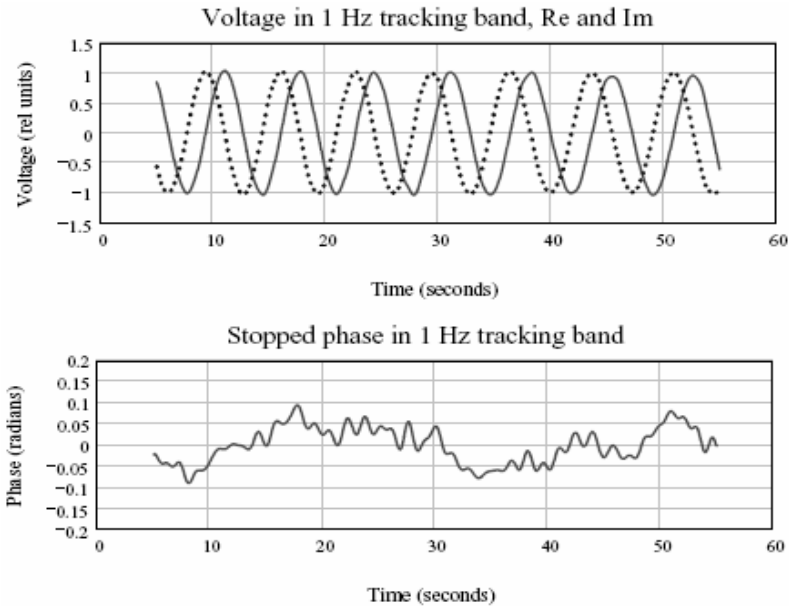


Fig. 13.5. Illustration of phase-tracking of SMART-1 S-band carrier line with frequency residuals < 1 mHz.

One of the MC–MH observations covered a period of lunar occultation of SMART-1. During this event it was possible to observe the phenomenon of radio signal diffraction on the lunar limb. Figures 13.6 and 13.7 present detection of diffracted radio waves with distinctly different Doppler slopes compared to the direct, non-diffracted signal. The diffracted signal is visible on both figures, beginning some ~5 s before the spacecraft’s “geometrical” egress from behind the Moon. The frequency scales at MC and MH were cross-calibrated to sub-mHz accuracy using clock-search data obtained on the calibrating background source.

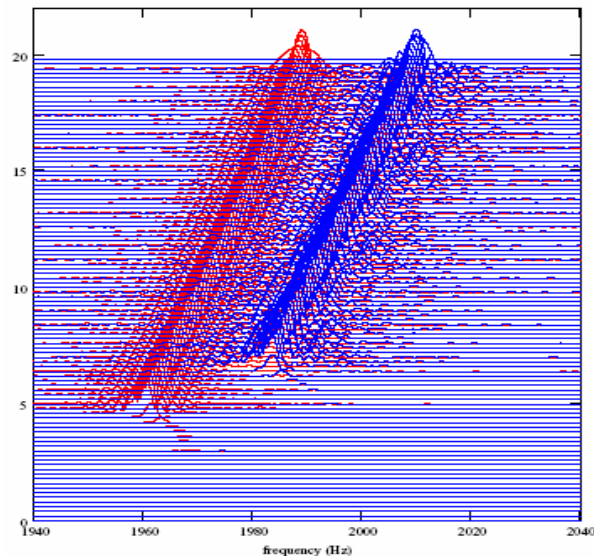


Fig. 13.6. Dynamic topocentric spectra of the SMART-1 S-band carrier line detected at Medicina (red) and Metsähovi (blue). The vertical axis is marked in seconds. The amplitude of the signal is presented in logarithmic scale. The MC and MH detections are shifted in time and frequency due to the difference in geographical location of the stations. The diffracted signal is visible as a “mouse tail” with opposite Doppler trend during a few seconds at the beginning of detection.

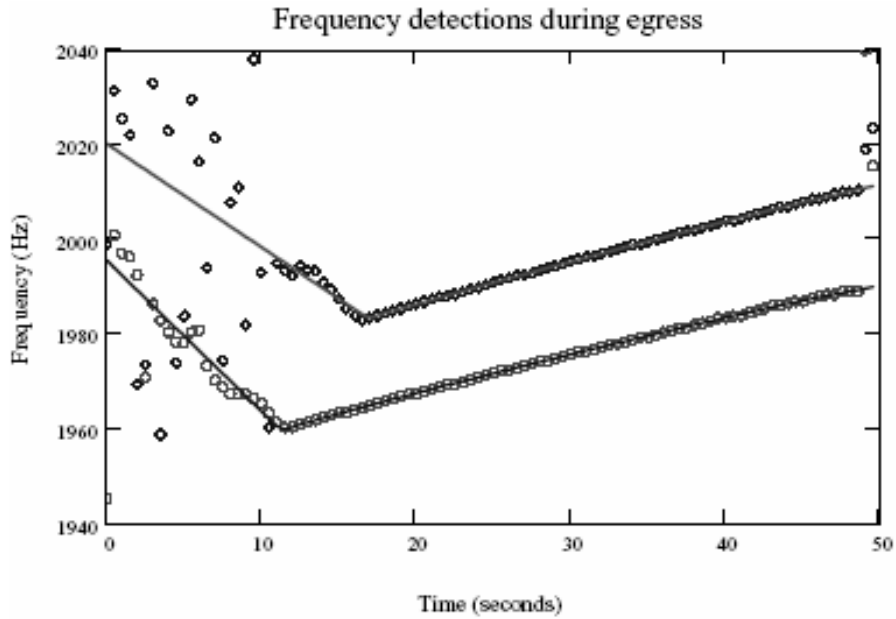


Fig. 13.7. Topocentric frequency detections of the SMART-1 S-band carrier line around the time of egress at Medicina (circles, lower curve) and Metsähovi (diamonds, upper curve) in a 100 Hz tracking band. The “elbows” points correspond to the spacecraft egress from the lunar limb. Pre-egress detections correspond to the diffracted radio signal.

The strength of the SMART-1 signal made it possible to achieve detections with integration time of 40 ms per point, sufficiently short for clear registration of a classical diffraction pattern (Figs. 13.8 and 13.9). The model patterns were computed for an ingress event, so the time direction is opposite to that detected during egress.

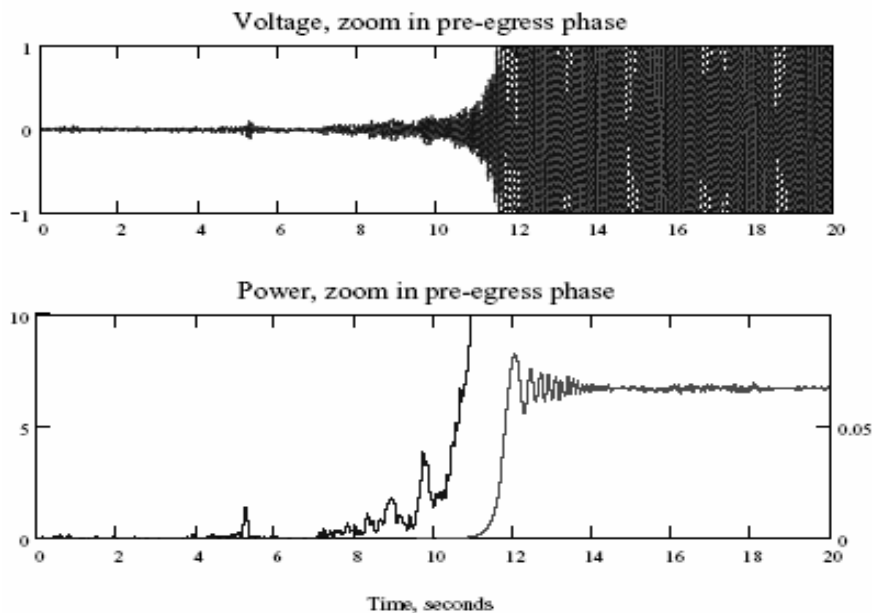


Fig. 13.8. Pre-egress diffraction pattern of SMART-1 carrier line, voltage (top) and power (bottom). The moment of the geometrical egress can be timed with an accuracy of several ms.

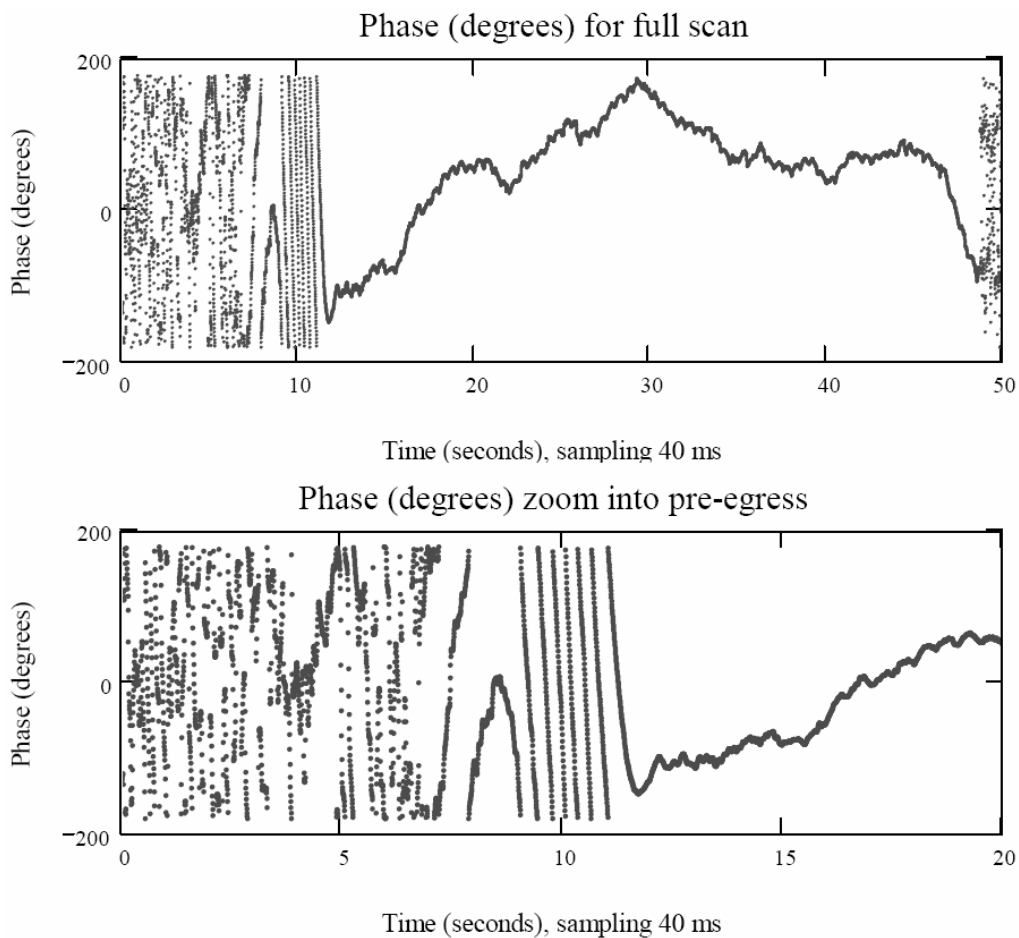


Fig. 13.9. Pre-egress diffracted pattern of the SMART-1 S-band line carrier (top) and zoom into the first 20 s (bottom).

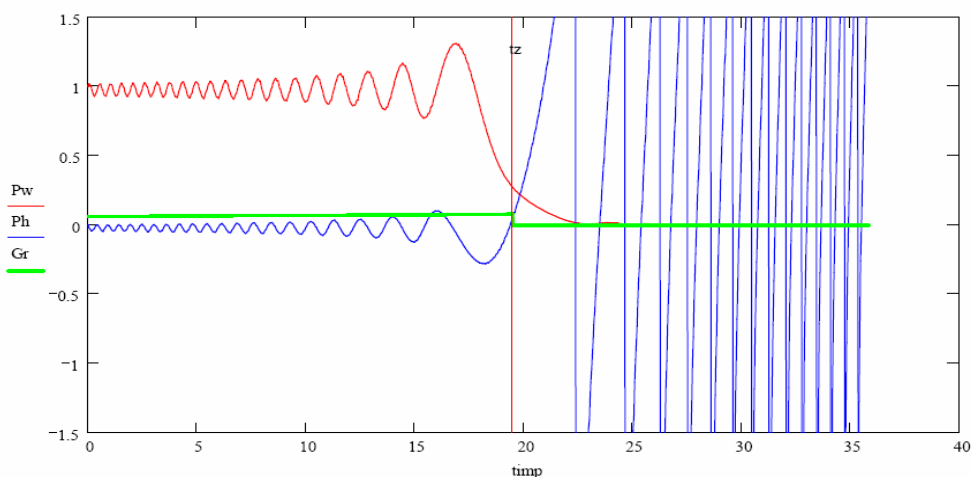


Fig. 13.10. A theoretical model for power (red) and phases (blue) of a diffracted signal on a flat circular screen for the case of ingress. A green line and a red vertical marker indicate the moment of geometrical ingress

The observed and theoretical diffraction patterns (Figs. 13.8, 13.9 and 13.10) are strikingly similar. The observed case is, of course, complicated by the actual 3D topography of the lunar surface near the limb and radio-refraction properties of the lunar surface. Fitting the theoretical diffraction pattern to that observed allows determination the moment of geometrical egress with an accuracy of several ms. At S/C velocity of ~ 1 km/s and a Fresnel zone size of ~ 500 m at S-band translates to several meters of positioning uncertainty of the S/C relative to the Moon 3D topography. Measurements similar to those shown in Figs. 13.8 and 13.9 could become a powerful diagnostic tool for studies of surface morphology. The results on spacecraft signal diffraction on the Moon presented here should be considered a demonstration for future “diffraction sounding” experiments with planetary missions.

Smart-1 observations on 2006.07.31 yielded a robust detection of the S/C at all 3 participating telescopes, MC, MH and WB. Spectra (resolution 31.5 Hz, integration 10 s) detected with Westerbork for two different modes of the S/C transmission are shown in Fig. 13.11. Supposedly, Scan No0001 corresponds to a ground-locked, high data rate mode, while Scan No0006 – to a free running on-board oscillator and low data rate.

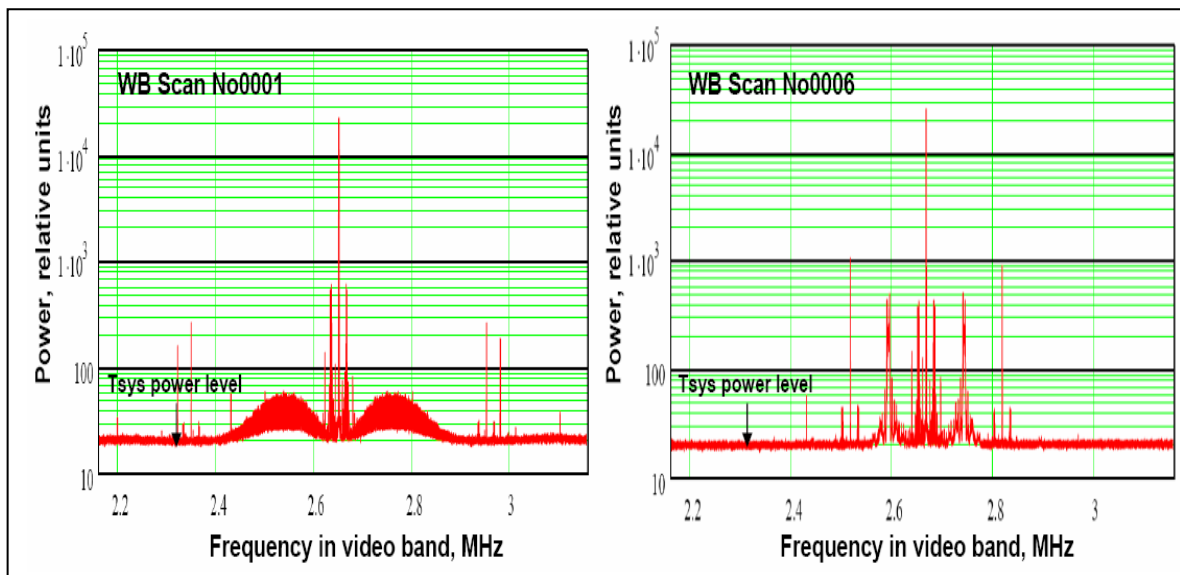


Fig. 13.11. Smart-1 signal spectra detected with Westerbork for two different modes of the S/C transmission. Arrows indicate the system noise power level in the video band.

Multi-station detection allowed us to characterize the detected phases and to distinguish between the phase jitter caused by propagation effects and intrinsic properties of the S/C signal. Averaging the detected phases for several stations effectively averages down the propagation effects, outlining the proper phase behaviour of the S/C oscillator and RF-chain, while the difference between station data and common mode outlines the propagation effects phase fluctuations as seen by individual stations. Fig.13.12 illustrates this characterization process. LO phase excursions of 1-2 radians on time scale ~ 1 minute can be tracked with 0.15-0.2 radian accuracy. Of course, this approach will work better for more than 3 stations observational setup.

Computing the auto correlation functions of phase residuals allows estimating the Allan variance of the S/C LO when cleaned from propagation effects for different modes of operation, while the same computation done for station residuals shows the combined station LO and propagation effects variance. Normalized auto correlation functions, computed for the common mode and station residuals for two scans are shown in Fig. 13.13. They allow estimation of the characteristic time of the process variation (as a width of the normalized autocorrelation function at a 0.5 level), while the process standard deviation characterizes the amplitude of the variance.

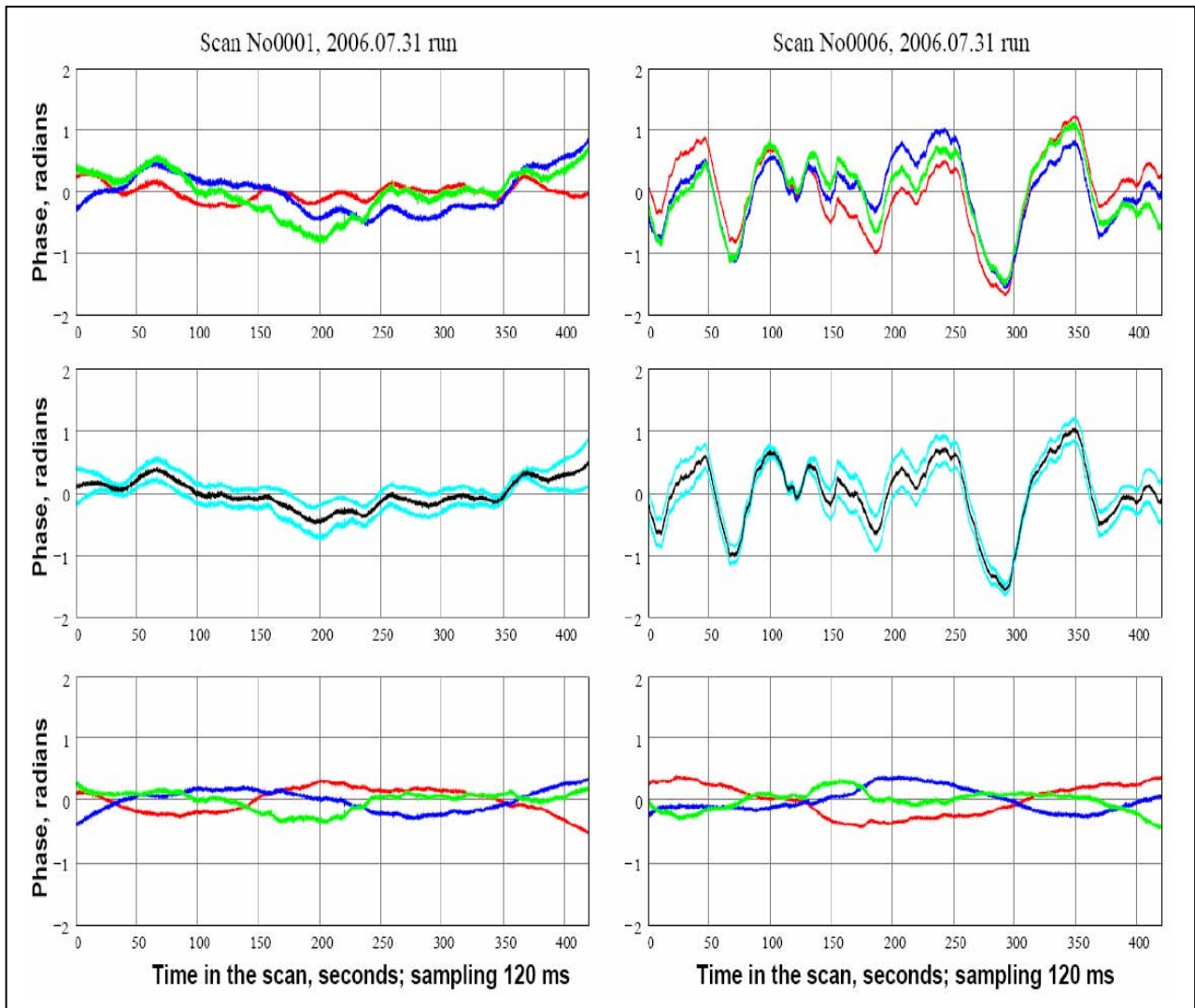


Fig. 13.12. Characterization of the S/C carrier line phase for two different transmission modes (left and right) using multi-station data. Detected phases of the carrier line (MC – red, MH – blue, WB – green) - upper panels. Common mode (average of three stations – black, and +/- 1 sigma band – light blue) – middle panels, and difference between station data and common mode – lower panels, colour coding the same as for upper panels.

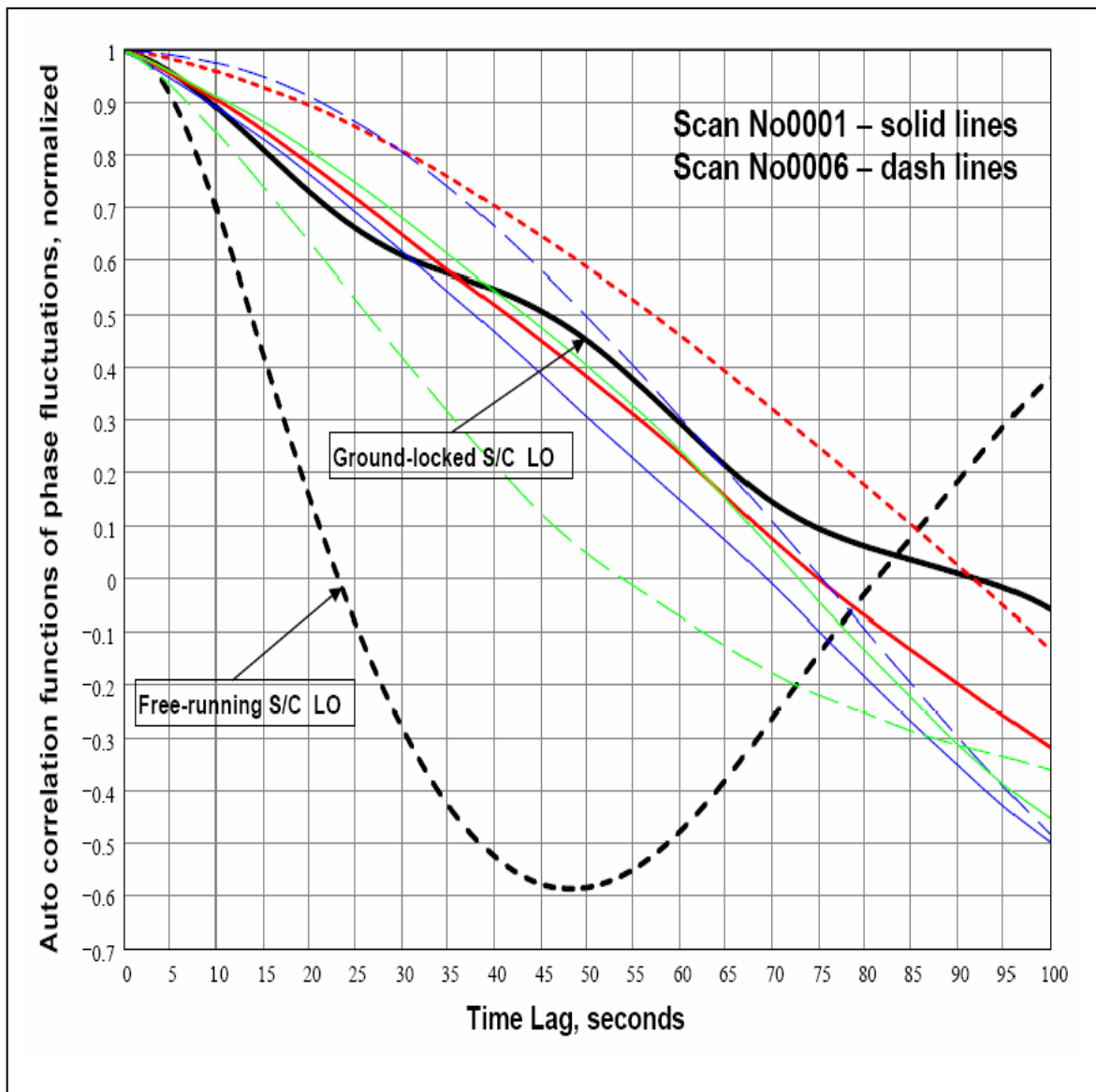


Fig. 13.13. Normalized auto correlation functions for the common mode (S/C LO) and station based phase variation processes. The common mode is shown in black, while station data is colour coded the same way as on previous figures.

Given the standard deviation $\sigma(\phi)$ and characteristic time t_c of the phase fluctuation process are estimated, the Allan variance for the carrier frequency F_o can be evaluated as:

$$Av = \delta f/f = \sigma(\phi) * t_c^{-1} * (2\pi F_o)^{-1}$$

Note, that this is a first order evaluation of the Allan variance. Actual measurement would require much longer time series covering more than just 5 -10 characteristic times. Estimated characteristic times and standard deviations for the residual phases, as well as corresponding evaluation of the Allan variances are summarized in Table 13.1.

Table 13.1. Characterization of the station based and S/C related phase variance at S-band. Propagation effects are included into station based variance, while S/C down-link path is “cleaned” from them.

	Characteristic Time, seconds	Standard deviation, radians	Allan Variance @ time scale
Station MC	41 :- 57	0.20 :- 0.25	0.33 e-12 @ 49s
Station MH	38 :- 50	0.17 :- 0.19	0.30 e-12 @ 44s
Station WB	32 :- 50	0.15 :- 0.16	0.28 e-12 @ 41s
S/C Ground-locked	46	0.22	0.35 e-12 @ 46s
S/C free run	14	0.58	2.94 e-12 @ 14s

We know that maser clocks at VLBI stations used for down-link reception and at ESA tracking stations used for up-link transmission have Allan variance $\sim 1.0e-14$ or better at the time scales ~ 1 minute, so the measured S/C LO variance in the ground-locked mode is mostly determined by the propagation effects over the up-link path, unsurprisingly equal to that of the down-link path as measured by the VLBI stations.

An Earth-based network of radio telescopes participated in SMART-1 tracking during its last orbit and impact on the Lunar surface on 3 September 2006. Due to Moon visibility constraints, the impact could be observed only from the Pacific area. The participating telescopes (Fig. 13.14) were Fortaleza (14 m, Brazil), TIGO (6 m, Concepcion, Chile), Australia Telescope Compact Array (ATCA, Narrabri, Australia) and Hobart (26 m, Tasmania, Australia). The data were recorded on Mk5A VLBI disk systems at Fortaleza, TIGO and Hobart. The ATCA data were first recorded on the Australian LBA disk data acquisition system and then translated into the Mk5 format using the procedure developed originally for the Huygens VLBI experiment (Chapter 6).

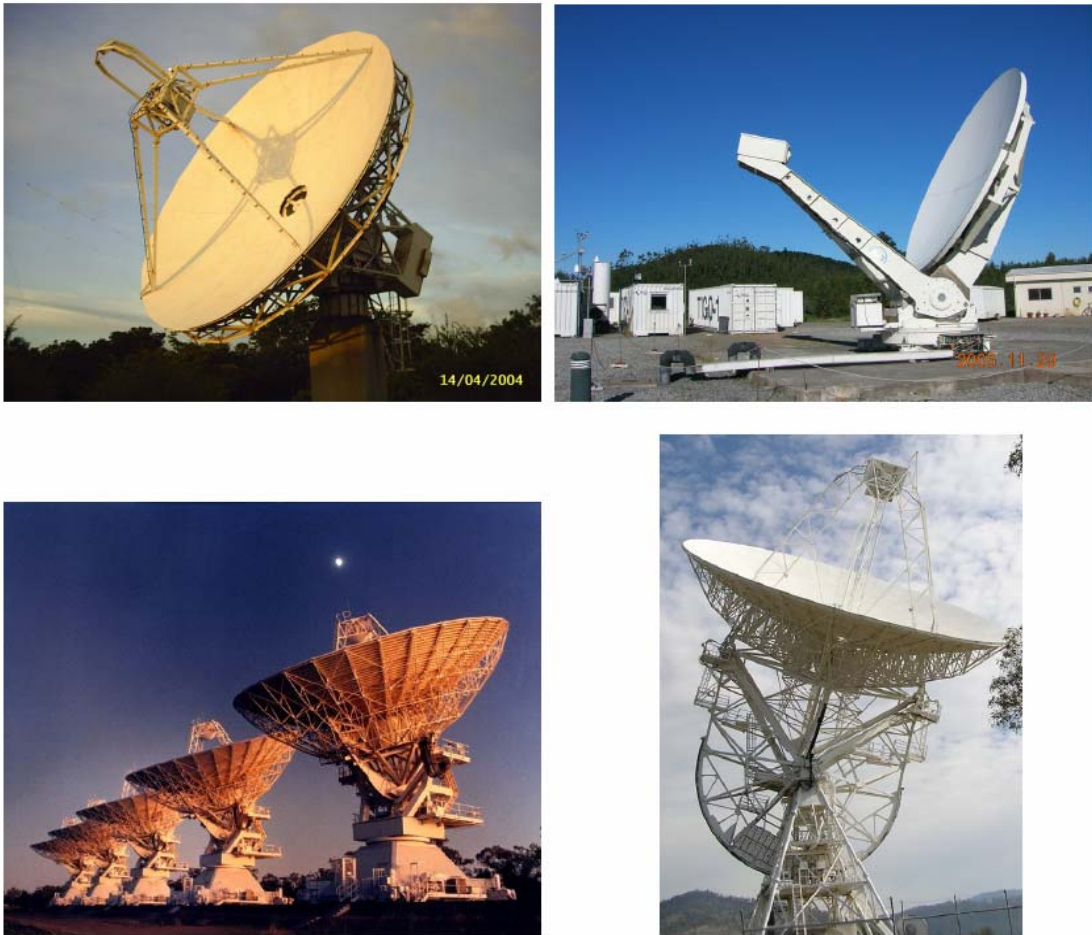


Fig. 13.14. Radio telescopes involved in the radio astronomy tracking of the last SMART-1 Lunar orbit, from top left, clockwise: Fortaleza (14 m, Brazil), TIGO (6 m, Concepcion, Chile), Hobart (26 m, Tasmania, Australia) and Australia Telescope Compact Array (ATCA, Narrabri, Australia).

Processing of the last orbit tracking data was conducted at JIVE using the same algorithms as in the prior radio astronomy experiments with SMART-1 in May-June 2006. The experiment was based on VLBI-style data acquisition and processing, but with an unusual for VLBI aim – to try to determine the time of impact with greatest possible accuracy. SMART-1 was transmitting at both S- and X-bands until its destruction at the impact.

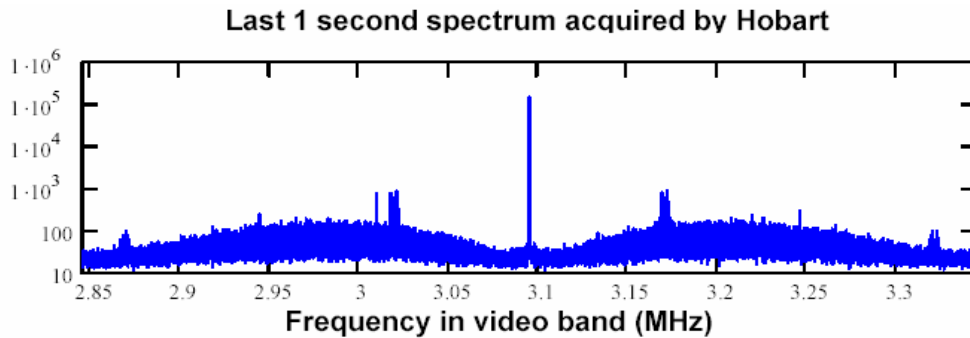


Fig. 13.15. Spectrum of the SMART-1 S-band signal during the last second prior to the impact detected at Hobart. The amplitude (vertical axis) is shown in arbitrary logarithmic scale. The main carrier line at ~3.1 MHz is detected with huge SNR.

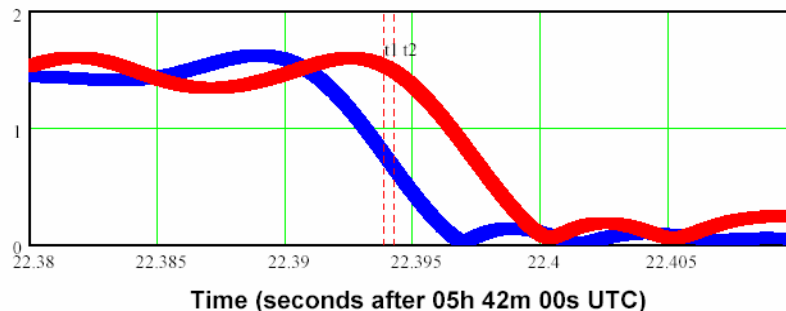


Fig. 13.16. The carrier line power (in arbitrary units) in a narrow tracking band as detected by TIGO (red) and Hobart (blue) during the last 30 ms of the SMART-1 mission. The vertical dashed lines mark a search window for the impact event with a higher time resolution as shown in Fig. 13.14.

Figs. 13.15 and 13.16 represent the SMART-1 S-band carrier signal during the last one second and last 30 ms of the mission, respectively. The delay of ~4 ms in the impact event time as it was seen by TIGO (red) relative to Hobart (blue) is due to a difference of light travel time from SMART-1 to the TIGO and Hobart sites.

Fig. 13.17 presents three one-second “snapshots” of the wide-band spectra from Hobart containing the SMART-1 S-band signal around the time of the impact. The central time frame contains the “last photons” received by Earth-based radio telescopes: Their localisation in time is illustrated in Fig. 13.18. It shows the signal power in a 300 kHz band around the S-band carrier line as a function of time during the last 300 μ s of the mission. The greater the bandwidth, the greater the contribution due to noise, compared to Fig. 13.16. The data shown in Fig. 13.18 were further “zoomed” and searched with a 10 μ s window for events with 3σ excess over the noise power. This search resulted in the following estimate of the arrival of “last photons” to Hobart as 05:42:22.394076 \pm 0.000010 s. A similar analysis for TIGO gives the “last photons” arrival time of 05:42:22.398 \pm 0.001 s. The much lower statistical accuracy of the TIGO estimate is due to the lower sensitivity of the 6-m antenna comparing to the 26-m Hobart. Note that the time marker of the last fully received SMART-1 telemetry word is 05:42:21.759, some 600 ms earlier than the “last photons” arrival detected by Hobart. This difference should be attributed to the difference in geographical location of Hobart and the telemetry tracking station, as

well as the fact that the duration of one telemetry word transmission was about 2 s. The impact has actually interrupted transmission of the next telemetry word.

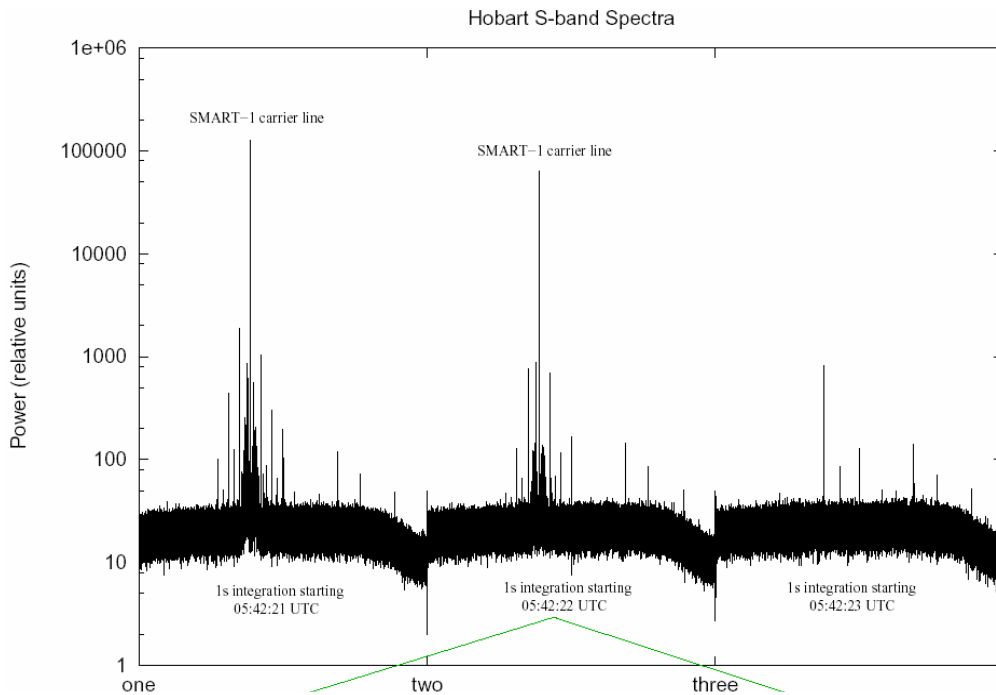


Fig. 13.17. Three one-second “snapshots” in the SMART-1 S-band spectrum around the carrier line as detected by Hobart. Green lines indicate the position of further search for “last received photons” in a 300 kHz data band.

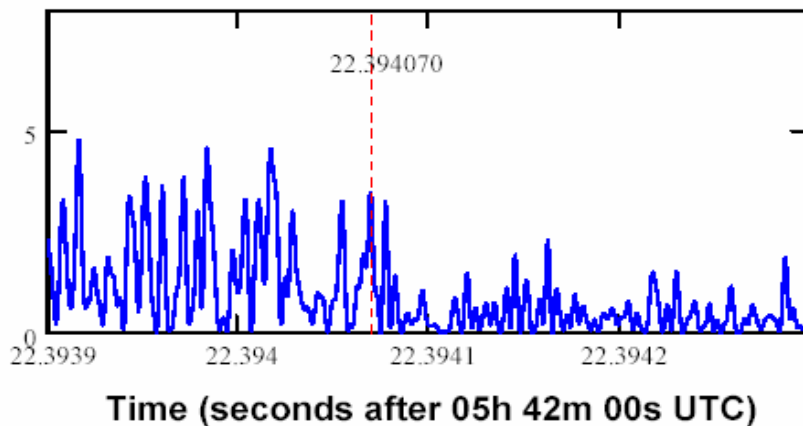


Fig. 13.18. SMART-1 S-band signal power (arbitrary units) in the 300 kHz band around the carrier frequency as a function of arrival time at Hobart. Moment of the end of the transmission can be defined as a change of power level and determined with +/- 10 us accuracy.

13.1.1. Occultation data analysis

A deeper analysis of the occultation diffraction patterns is now in progress as a cooperative efforts of scientists from JIVE and Shanghai Astronomical Observatory of Chinese Academy of Sciences. Preliminary results are encouraging and were presented at ASTRON/JIVE Daily Image website (<http://www.astron.nl/dailyimage>) as a poster presentation, which is also shown in Fig.13.19. Research will continue.

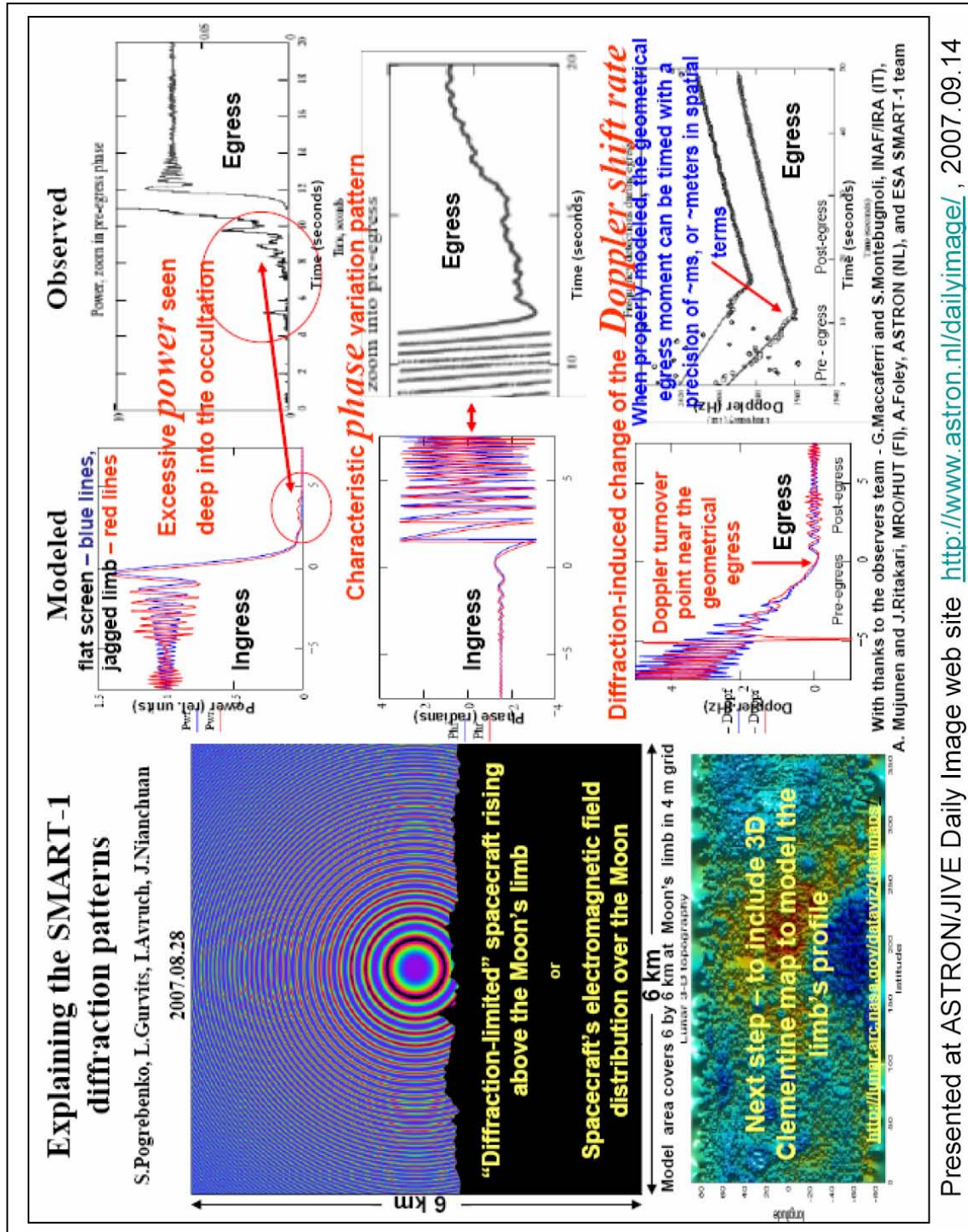


Fig. 13.19. Poster presentation at ASTRON/JIVE Daily Image website.

13.1.3. Conclusions

The SMART-1 radio astronomy observing campaign resulted in obtaining experience in VLBI-style observations of spacecraft at observatories never before involved in observations of the non natural radio sources (TIGO, Fortaleza). This experience and complementary to other stations sky coverage might become an asset in similar observations in the future.

The campaign also made it possible to work out operational interaction with the Navigation group at ESOC. In several instances, this interaction resulted in dynamic rescheduling of VLBI observations of SMART-1, never before exercised at European radio telescopes.

It was shown that the multi-station detection of the S/C signal allows discriminating between propagation media effects (in Earth ionosphere and troposphere) and proper S/C LO phase fluctuations for better characterization of the latter.

The high time resolution timing of SMART-1 events, including the lunar impact, demonstrated a high potential of radio astronomy tracking during critical events of space science missions.

The detection of diffraction pattern of SMART-1 S-band radio signal opens an opportunity to investigate further the novel technique of “radio occultation sounding” of planetary bodies.

13.2. Outlook for future missions

The Huygens VLBI tracking experiment demonstrated the potential of radio astronomy and VLBI support to planetary and other space science missions. The progress of VLBI technology over the last decade – introduction of disc-based high data rate VLBI media, high performance data processing facilities, improved geodetic and astrometric support of phase-referencing VLBI experiments – dramatically improved the major characteristics of the technique. Coupled with the fact that VLBI tracking imposes minimal requirements on the on-board instrumentation and can be often conducted as “piggy-back” on standard radio link from spacecraft, the technique can enhance significantly scientific applications which require high accuracy estimates of the spacecraft state vector. These applications cover a broad range of scientific disciplines, including physics of planetary atmospheres (as in the Huygens VLBI tracking experiment), planetary dynamics, gravimetry and fundamental physics.

The Huygens VLBI tracking experiment triggered introduction of the concept of Planetary Radio Interferometry and Doppler Experiment (PRIDE) – a generic experimental setup of on-board and Earth based radio devices and facilities.

The concept of PRIDE has been considered as a component of the ESA CV Laplace [15] and TandEM [16] missions for investigations of Kronian and Jovian systems, respectively, as well as the prospective Venus mission EVE [17].

Fig. 13.20 illustrates all the general scheme of PRIDE. Most of the on-board instrumentation shown in the scheme is not PRIDE-specific and is present in service and science payload. The Earth-based segment of PRIDE includes standard operational VLBI networks and data processing facilities.

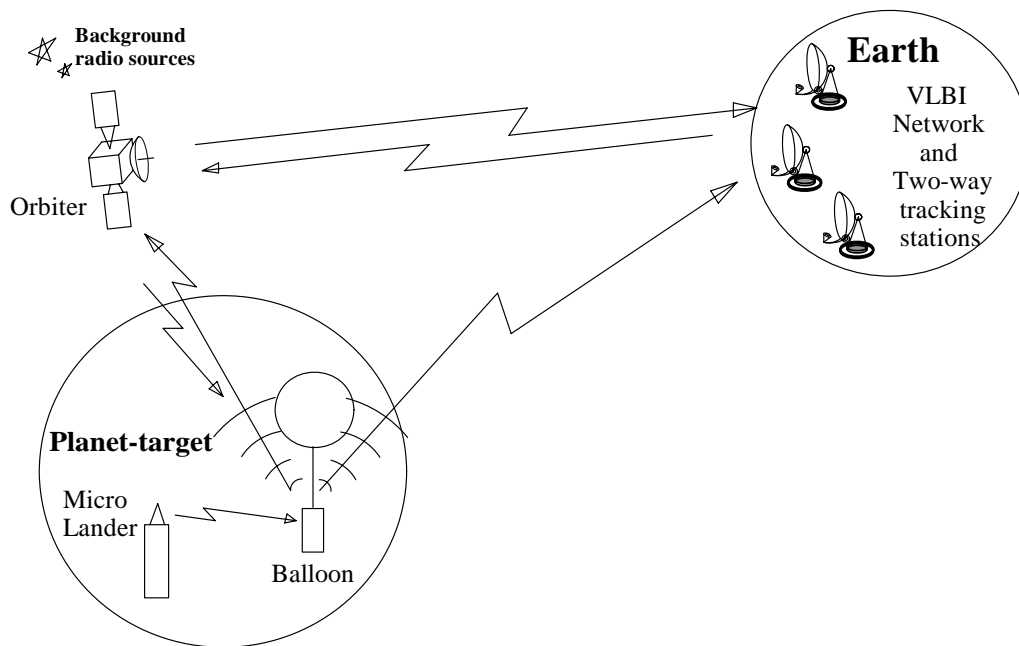


Fig. 13.20. Generic configuration of the Planetary Radio Interferometry and Doppler Experiment (PRIDE).

An example of target characteristics of the PRIDE experiment for Titan and Enceladus Mission (TANDEM), PRIDE-T, are shown in Table 13.2. The table represent rather conservative estimates of PRIDE-T characteristics based on available today technologies. However, they offer a 50-fold improvement of the achievable position accuracy reaching tens of metres at the distance to Saturn. .

Table 13.2. Comparison of Huygens VLBI tracking and PRIDE-T parameters.

	Huygens	PRIDE-T	Resolution gain
Radio link frequency	2 GHz	2/8/32 GHz	1/4/16
Distance	8 AU	~8 AU	1
VLBI "fringe" SNR	10 - 30	30 - 100	~3
Position accuracy (1 σ)	1 km	<u>360/80/20 m</u>	~3/12/50

Further improvement of PRIDE characteristics should be expected with the advent of the next generation radio telescope, the Square Kilometre Array (SKA, [18]) which will enable further at least ten-fold increase in the achievable SNR for VLBI fringes and proportional improvement of the positional accuracy. In addition, SKA with basically the same setup as required by PRIDE will make possible Direct-to-Earth communication from planetary probes equipped with low power (~1 W) and low-gain transmitters with the data rate of several tens of bits per second [19].

13.3. Huygens VLBI tracking: dissemination of results and outreach

In the period 2004 – 2008, various aspects of the Huygens VLBI tracking experiment were presented by the members of the team more than 40 times at national and international scientific meetings, including COSPAR scientific assemblies of 2006 (Beijing, China) and 2008 (Montreal, Canada), URSI assemblies of 2005 (New Delhi, India) and 2008 (Chicago, IL, USA), IAU General Assembly (2006, Prague, Czech Republic), European Planetary Science congresses of 2006 (Berlin, Germany) and 2007 (Potsdam, Germany), International Planetary Probe workshops of 2004 (Lisbon, Portugal), 2005 (Thessaloniki, Greece), 2006 (Pasadena, CA, USA), 2007 (Bordeaux, France), colloquia at ASTRON/JIVE, ESTEC, JAXA etc.

The major results of the experiment, the reconstructed descent trajectory of the Huygens Probe and evidence of the meridional wind (chapter 8 of this report) are being prepared for a refereed publication [4]. Pre-mission and early preliminary descriptive presentations of the Huygens VLBI tracking experiment are given in [20-23].

The Huygens VLBI tracking experiment featured in a number of TV programmes and movies (e.g. “Titan – a place like home?”, BBC Horizon Production, UK, 2005; “The Universe as seen by radio astronomers”, ESA TV Production for EuroNews, 2006), national and international TV, radio and printed media. The experiment was presented to a large audience (more than 300 people) of high-school students at the “International Year of Physics” event in Amsterdam (June 2005) and to the group of journalists at the EC FP6 press-conference (Westerbork, July 2005).

14. Conclusions

This report describes activities conducted under the ESA-ESTEC Contract No. 18386/NL/NR. The main topic of the contract, the Huygens VLBI tracking experiment, has been conducted successfully on 14 January 2005. Main results of the experiment and related work are as follows:

- 1). VLBI observations of the Huygens Probe during its descent in the atmosphere of Titan enabled reconstruction of the descent trajectory with the lateral accuracy of about 1 km (chapter 8).
- 2). The Huygens VLBI experiment assisted in achieving the goal of one of the Huygens experiments, the Doppler Wind Experiment, and provided evidence for the meridional component of the wind in the Titan atmosphere (chapter 8).
- 3). Radio astronomy observations conducted by the telescopes involved in the Huygens VLBI tracking experiment helped to compensate the loss of communication between Huygens and Cassini via the channel A at the carrier frequency of 2040 MHz and achieve the goal of the Doppler Wind Experiment.
- 4). “Eavesdropping” on the Huygens transmission at the frequency of 2040 MHz by the Earth-based radio telescopes involved in the Huygens VLBI tracking experiment (the NRAO Green Bank Telescope and ATNF Parkes Radio Telescope) and express processing of data from the single VLBI baseline Parkes – Mopra (Australia) with the data delivered from Australia to JIVE (The Netherlands) via global network of fibre cables have made possible quick diagnostics of crucial components of the Huygens on-board instrumentation (chapter 5).
- 5). The Huygens VLBI tracking experiment paved the way for future radio astronomy and VLBI segments of planetary science missions. Conservative estimates based on the present day technology indicates that future Huygens-style VLBI experiments can achieve significant (more than order of magnitude) improvement of position and velocity measurements of planetary probes and other spacecraft in deep space (chapter 13).

15. Acknowledgements

The members of the project teams express their gratitude to the directors and staff of the Australia Telescope National Facility (Australia), Westerbork Radio Observatory (The Netherlands), Radio Astronomy Department of the University of Tasmania (Australia), Shanghai and Urumqi VLBI Stations of the National Astronomy Observatories of China, Green Bank Telescope and Very Large Array of the National Radio Astronomy Observatory (USA), Medicina Radio Astronomy Station (Italy), Metsähovi Radio Observatory (Finland), Kashima Radio Astronomy Station of the National Institute for Information and Communication Technologies (Japan), Northeastern Space Radio Observatory (Brazil), Transportable Integrated Geodetic Observatory (Germany and Chile) for their support to the observations described in this report.

The Joint Institute for VLBI in Europe is funded by the national research councils, national facilities and institutes of The Netherlands (NWO and ASTRON), the United Kingdom (STFC), Italy (INAF), Sweden (Onsala Space Observatory, National Facility), Spain (IGN), France (CNRS), PR China (NAOC) and Germany (MPIfR). The European VLBI Network is a joint facility of European, Chinese, South African and other radio astronomy institutes funded by their national research councils. National Radio Astronomy Observatory is operated by Associated Universities, Inc., under a cooperative agreement with the National Science Foundation. The Australia Telescope is funded by the Commonwealth of Australia for operation as a National Facility managed by CSIRO.

16. References

- [1] VLBI tracking of the Huygens Probe at Titan, ESTEC Contract No. 17002/02/NL/LvH/bj CCN 03, JIVE Research Note #0005, July 2004
- [2] VLBI Observations of the Huygens Probe, ESA Contract No. 18386/NL/NR Progress report No. 1, JIVE Research Note #0007, November 2004
- [3] VLBI tracking of weak signal of Deep Space Probes
ESA-ESTEC Contract No. 18407/04/NL/LvH/bj, JIVE Research Note #0006
04.12.2004
- [4] Pogrebenko S.V. et al., 2008, "*VLBI Tracking of the Huygens probe during its Descent in the Upper Atmosphere of Titan: Evidence for Meridional Wind*", Planet. Space Sci., in preparation
- [5] VLBI Analysis Software CALC/SOLVE, NASA Goddard Space Flight Center, <http://gemini.gsfc.nasa.gov/solve/>
- [6] Mathcad 12: A Tool for Engineering Problem Solving, www.mathsoft.com
- [7] Giorgini J.D. et al. 1996, "*JPL's On-Line Solar System Data Service*", Bulletin of the American Astronomical Society, v. 28(3), p. 1158
- [8] Schilizzi R.T. et al. 2001, "*The EVN MarkIV VLBI Data Processor*", Experimental Astronomy, v. 12, p. 49
- [9] Whitney A.R. 2002, "*Mark 5 Disc-based Gbps VLBI Data System*", Proceedings of the 6th European VLBI Network Symposium, June 25-28, Eds. E. Ros et al., Bonn: MPI Radioastronomie, p. 41
- [10] Sovers O.J., Fanelow J.L. & Jacobs C.S. 1998, "*Astrometry and geodesy with radio interferometry: Experiments, models, results*", Reviews of Modern Physics, v. 70, No. 4, p. 1393
- [11] Huygens Descent Trajectory Working Group (DTWG) data base, http://www.mrc.uidaho.edu/~atkinson/Huygens/DTWG_Data/DTWG%233/OFFICIAL/
- [12] SPICE Toolkit, NASA JPL NAIF, <http://naif.jpl.nasa.gov/naif/toolkit.html>
- [13] Lorenz R.D., et al., 2007, "*Descent motions of the Huygens probe as measured by the Surface Science Package (SSP): Turbulent evidence for a cloud layer*", Planet. Space Sci., doi:10.1016/j.pss.2007.04.007
- [14] Foing B H. et al., 2006, "*SMART-1 mission to the moon: Status, first results and science goals*", Adv. Space Research 37, p. 6
- [15] Blanc M. et al., 2008, "*LAPLACE: A mission to Europa and the Jupiter System for ESA's Cosmic Vision Programme*", Exp Astronomy, in press
- [16] Coustenis A. et al., 2008, "*TandEM: Titan and Enceladus mission*", Exp. Astronomy, DOI 10.1007/s10686-008-9103-z

- [17] Chassefière E. et al., 2008, “*European Venus Explorer (EVE) - An in-situ mission to Venus*”, Exp. Astronomy, in press
- [18] Schilizzi R.T. et al., 2007, “*Preliminary Specifications for the Square Kilometre Array*”, SKA Memo No. 100, http://www.skatelescope.org/pages/page_astronom.htm
- [19] Fridman P.A., Gurvits L.I. & Pogrebenko S.V., 2008, “*The Square Kilometre Array as a "Direct-to-Earth" Facility for Deep Space Communications*”, SKA Memo No. 104, http://www.skatelescope.org/pages/page_astronom.htm
- [20] Lebreton J.-P. et al., 2005, “*An overview of the descent and landing of the Huygens probe on Titan*”, Nature, 438, 758
- [21] Bird M.K. et al., 2005, “*The vertical profile of winds on Titan*”, Nature, 438, 800
- [22] Witasse O. et al. 2006, “*Overview of the coordinated ground-based observations of Titan during the Huygens mission*”, Journal Geophys. Research 111, E07S01
- [23] Gurvits L.I., 2004, “*Christiaan Huygens, Huygens the Probe and radio astronomy*”, in Titan: from Discovery to Encounter, ESA SP-1278, p. 408